Università degli studi di Padova

Dipartimento di Fisica e Astronomia "Galileo Galilei"

Corso di laurea Magistrale in Fisica

Development of a multiple microdosimetric detector based on GEM (Gas Electron Multiplier), for hadron-therapy applications.

Relatore: Laura De Nardo   Laureando: Marchiori Elena

A. A. 2013/2014

Alla mia bicicletta rosa

Table of Contents:

0. Introduction

Radiation is a form of energy that has always been around in nature and human beings are irradiated throughout life. To assess the impact of radiation exposure properly, it is essential to understand the mechanism of the interactions of radiation with living organisms. Based on their primary interaction mechanisms, ionizing radiation can be classified into directly ionizing charged particles (e.g., electrons, protons, alpha, etc.) and indirectly ionizing radiation (e.g., photons and neutrons). Radiation of indirectly ionizing type deposits its energy through the production of charged particles (so-called secondary charged particles), which are directly ionizing type. In the case of directly ionizing interactions of charged particles with matter, the energy is lost in a large number of relatively small interactions via the Coulomb forces causing ionizations and excitations of the atoms and molecules. In a living cell, ionization and excitation of atoms and molecules initiate a complex chain of events from chemical changes in some important bio-molecules through mutations to bio-functional changes such as transformation and cell death. For this reason, ionizing radiation can be used to treat cancerous patients, concentrating the radiative beam into the affected area, to kill tumour cells without an invasive surgery, or chemotherapy.

Although different types of radiation may deposit the same average energy in an organ, living cells and tissues do not necessarily respond in the same way to these types of radiation. A rough division can be made trough "light" (electrons, photons) and "heavy" (protons and generally ions) particles. We usually talk about traditional radiation therapy, when referring to a therapy that uses beams of photons, and about hadron-therapy when beams of hadrons are used instead.

High ballistic accuracy, which offers the possibility to treat tumours located close to critical organs, and greater biological effectiveness for the same dose administered, make hadron-therapy preferable to conventional radiotherapy especially in critical cases, such as or particularly resistant tumours or patients who are particularly sensitive to radiation, such as children, because it is possible to minimize the radiation on healthy tissue. At the end of 2013, 48 treatment facilities were in operation worldwide and over 122 000 patients had been treated by means of protons and

heavier ions. Most of this therapy has been conducted using protons (about 105 000 patients) [1].

The low prevalence of hadron-therapy is due, besides to the high cost of acceleration systems, to the defective knowledge of physical properties and biological effects of therapeutic beams of hadrons, in particular, it is not always possible to ensure treatments with "biological effective dose" known with accuracy less than 5%, as required for an optimal treatment plan [2].

It is generally accepted that the microscopic distribution of energy deposition in volumes of cellular and sub-cellular dimensions is of critical significance for the level of biological damage caused. Therefore, measurement of radiation quantities in sites of size comparable to the cell or even the DNA cross-sections are required. Microdosimetry concerns the investigation of the energy depositions that occur in micro-volumes of the order of cellular and sub-cellular structures.

Through microdosimetric measurements, we are able to characterize in an appropriate manner the process of deposition of the local energy and explore the relationship between physical and biological world. For this reason experimental microdosimetry is used to achieve an adequate knowledge of the radiation fields generated by hadron beams.

To perform these microdosimetric measurements, proportional counters are extensively used. The equivalence to the human tissue is reached by employing Tissue-Equivalent (TE) materials. That is the reason for constructing the walls of the proportional counter out of a tissue-equivalent plastic and the use of a filling gas that has almost the same composition as human tissue. Therefore, these devices are called Tissue-Equivalent Proportional Counter (TEPC).

Furthermore, the simulation of a microvolume is carried out by the reduction of the gas pressure. Conventional TEPCs are proportional counters with a cavity employing a central anode wire. TEPCs are operated in pulse mode and the pulse-height spectrum is collected and converted to the parameter extensively used in microdosimetry, i.e. lineal energy.

Lineal energy is the energy imparted to the matter inside a unit volume by a single energy-deposition event divided by the mean chord length of the site, and it is commonly presented in units of keV/µm. The shape of a microdosimetric spectrum contains quantitative information that can be used to predict the relative biological effectiveness of radiation.

Commercial TEPCs have several shortcomings such as a relatively large physical size which limits spatial resolution and increases sensitivity to pileup effects. Furthermore, the cavity size does not allow to simulate site sizes than the typical micrometer (dimension of the cell nucleus, considered the most critical part of the cell). The possibility to investigate smaller site size, would permit to

analyse the effect of radiation in sites equivalent to the chromatin fibre (about 25 nm) and the DNA spiral (about 2 nm of diameter).

To study radiation effects both at the microdosimetric and nanometric scales, and to reduce pileup effects, miniTEPCs have been developed since 1990's [3]. Although these detectors allows to increase the resolution and the accuracy of the collected data, there are many difficulties in construction of a single and multi-element counter. Furthermore, the supply of counters for clinical usage is hampered by technical problems in the production of reliable detectors with predictable characteristics at comparatively little effort and low cost.

These drawbacks justify the efforts to develop a new type of TEPC based on a GEM instead of detectors employing a central anode wire. This thesis is about the development of an innovative multi-detector GEM (Gas Electron Multiplier)-TEPC that could allow a microdosimetric two-dimensional mapping (and three-dimensional in perspective) of therapeutic beams of ions, with a relatively small size and simple in construction and usage. The final aim is to create an easy TEPC to be used for dose conformation and dose delivery control in a clinical situation. This is part of MITRA INFN project (MIcrodosimetry and TRAck structure) started in 2012, that involves Universities of Padova, Milano, Roma and INFN-LNL. The goal of the project is to develop innovative methods and tools to characterize accurately the radiation fields generated by hadron-therapeutic beams:

- putting together microdosimetry, which measures fluctuations of the deposited energy at local level (µm) with excellent accuracy, and nanodosimetry, which measures track structures at nanometric level.

- developing innovative detectors for research, capable of measuring some physical characteristics that are descriptive of the "quality" of radiation and easily measurable.

- identifying useful solutions in clinical practice: developing new detectors that are robust, affordable and easy to use.

Six different activities make part of MITRA experiment, two for nanodosimetry, and four for microdosimetry. The development of a GEM based detector is one of these, targeted to the construction of a detector easy to use in clinic.

The experimental activity of characterization and optimization of the detector was carried out at the National Laboratories of Legnaro INFN.

The **Outline** of this thesis is briefly described as follows:

Chapter 1 gives an introduction about hadron-therapy and its applications, explaining advantages and disadvantages of this therapy. Different kinds of radiation damage are introduced, as well as the RBE, Relative Biological Effectiveness, that allows a physical description of biological effects of radiation.

Chapter 2 deals with microdosimetry and microdosimetric quantities, and its usage in hadron-therapy fields. The weighting function used to interpret microdosimetric spectra is defined.

Chapter 3 is about detectors used for experimental microdosimetry: conventional TEPCs, miniTEPCs, and presents the idea of a detector based on a GEM together with other works of this genre, developed in the last years.

Inside *Chapter 4* a general description of GEM operation is given. Moreover we introduce the concepts used to develop a single GEM detector in a general way.

Chapter 5 describes the motivations leading the design of the detector and describes the components of the prototype.

Chapter 6 explain the experimental set-up used for the measurements: the vacuum chamber, and the electronic chain.

Chapter 7 presents the experimental results obtained with this prototype, using an alpha and a gamma source. GEM effective gain has been evaluated in different conditions using the signal of an alpha source ^{244}Cm. A typical microdosimetric spectrum was acquired with a ^{137}Cs source, to prove that this GEM based prototype operates as a usual TEPC.

Chapter 8 deals with the conclusions and the futures improvements of the detector, and inside this chapter, new experiments for the characterization of this detector are proposed. Finally, it describes the advantages and disadvantages of this prototype for clinical usages.

1. Hadron-therapy

## 1.1 About ion beam therapy

The use of proton and ion beams has been proposed more than 60 years ago in 1946 by Robert Wilson [4]. In 1955 the first patients were treated with proton beams in Berkeley. Since then radiotherapy with proton and ion beams has constantly been developed at research centres. Within the last decade, however, a considerable number of hospital based facilities came into operation [5].

Ionizing radiation, interacting with biological matter, released some energy that can lead to a serious damage of the living structures (see **sec. 1.2**). Ideally, one would like to irradiate the tumour with a high dose of radiation, leaving the surrounding tissue, healthy, intact. This is obviously not possible, for this reason several ways to reach a satisfactory compromise are investigated.

Traditional radiation therapy uses high-energy photons, irradiating the affected area with different beams from several directions. In this way a low dose is released in the surrounding tissue, and the intersection of the beam that carries an higher dose, is concentrated in the tumour area. Although this is a clever way to carry the radiation, a wide fraction of the body is subjected to radiation, as can be seen in the left part of pic. **1.1.1**.

Using a beam of hadrons allows to concentrate better the radiation, and it also increases the dose released in the region concerned (see right part of pic. **1.1.1**).

Just looking at the graph of the depth-dose distribution of the different particles (pic. **1.1.2**), make evident the advantage of heavy ions in hadron therapy.
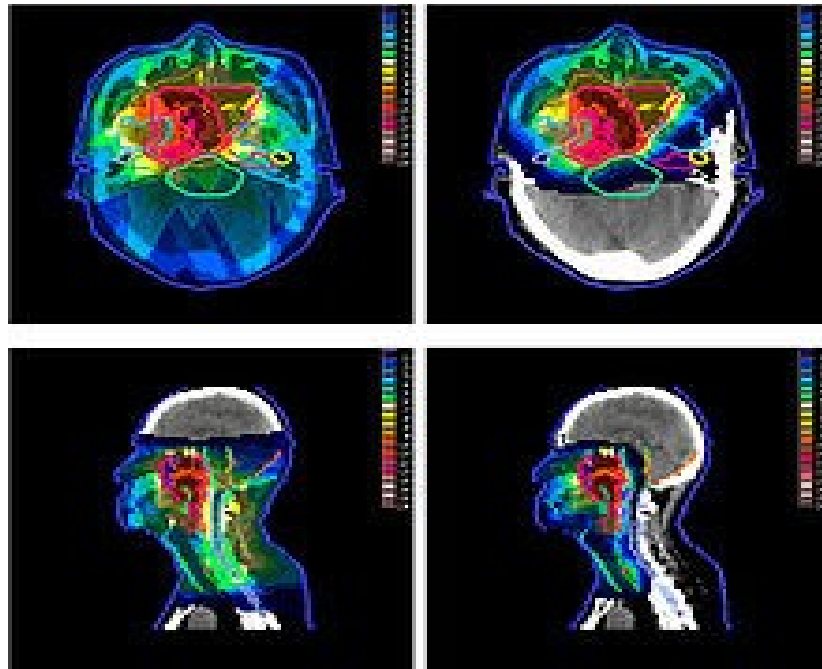
Pic. 1.1.1*: Irradiation of naso-pharyngeal carcinoma by photon (X-ray) therapy (left) and proton therapy (right)*
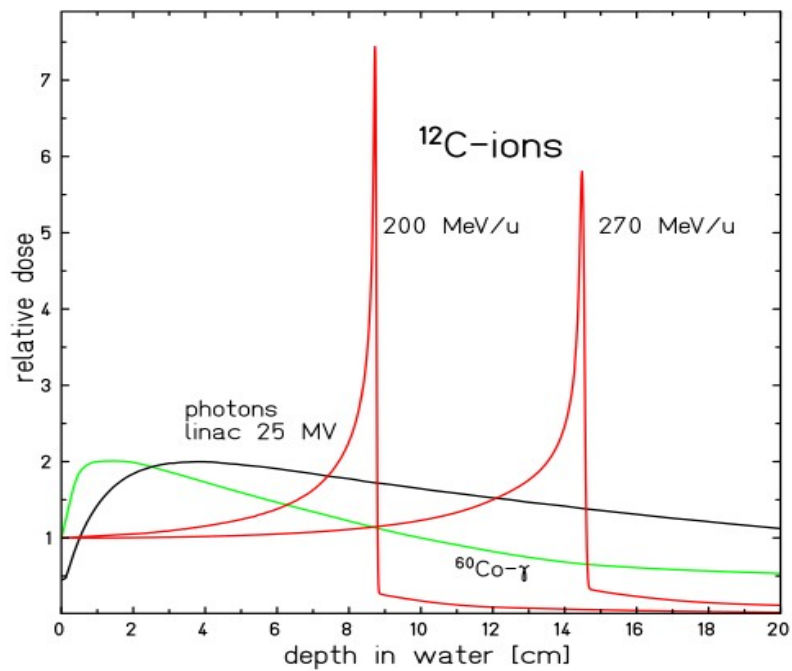
Pic. 1.1.2*: Profiles of the delivered dose with respect to depth for different types of radiation. Graph is taken from [5].*

The graph shows the delivered dose for different type of radiations. The dose depends on the interaction of particles with matter. When photons interact with matter the number of photons is exponentially decreasing and the depth-dose distribution is characterized first by an increase and then by a slow decrease. On the other side, charged particles slow down and gradually loose energy in atomic interactions until they come to rest. When slowed down, the number of interactions increases, reaching a maximum at the end of their range, and causing the maximum dose deposition called the Bragg peak. This behaviour allow to release a higher dose in the area of the target, releasing very little energy in the way [5].

In some cases clinical hadron-therapy would be preferable to conventional radiotherapy: particularly when the part to be irradiated is in depth or close to organ at risk. The dose that can be given to the tumour is in fact limited by the tolerance to the radiation of the surrounding healthy tissue. Tumours located near organs called "critical" or "at risk", often can not be irradiated at doses sufficiently high to be effective to treat the disease, due to the too high doses that would be necessary to administer to these healthy organs, with grave risk of damaging them.

In picture **1.1.3** it is showed the probability of tumour control and normal tissue complications as a function of the dose [5], and the ideal situation (blue): tumour control without normal-tissue complications. Normally, the dose window that can be exploited is very narrow, but it has been observed that a decrease in the irradiated volume, such as is possible to attain with hadrons, makes some organs more tolerant to radiation, thereby enabling a greater irradiation of the area. This effect is called dose volume [5]. In such cases, the use of hadrons allows a better ballistic precision and less irradiation of healthy tissue. Hadron-therapy is also preferable to conventional radiotherapy in the case of radio-resistant tumours that are those tumours which are less likely treatable by conventional radiotherapy for their biological behaviour.

The increased biological effectiveness of ion beam in the stopping region, offers a potential improvement to the dose delivered to the tumour without increasing the likelihood of complications to surrounding healthy tissue.
The reason for this enhanced biological effectiveness is an increase in the energy loss of the particles, when they are slowing down. Since the energy loss (and consequently also the Linear Energy Transfer) of e.g. a Carbon-12 ion is generally much larger as compared to a proton with the

same range, the term *high LET[1] radiation* is commonly used for heavier ions.
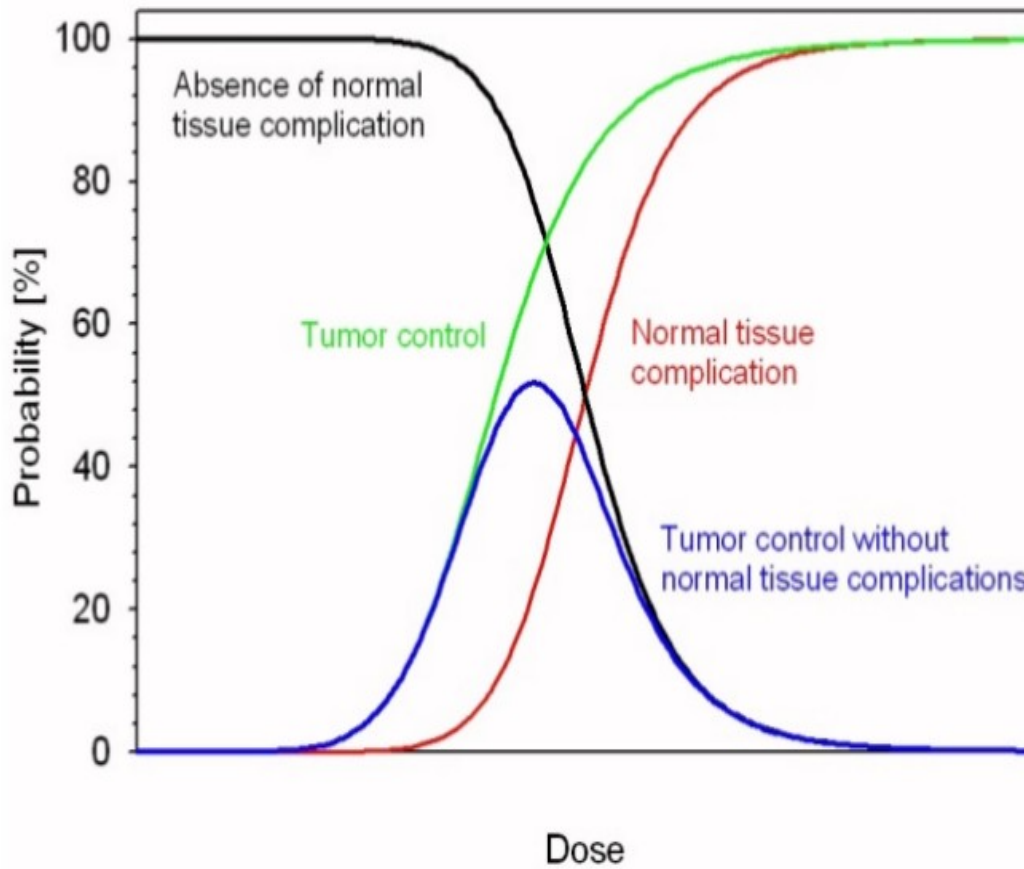
Pic. 1.1.3: Schematic representation of the probability of tumour control (green) and complications of normal-tissue (red) as a function of dose [5].

There is a large number of patients that may benefit from the use of improved radiation therapy techniques in general: according to recent cancer statistics, the relative number of patients that could be cured by improved radiotherapy techniques is in the order of 20% [5]. These patients cannot be cured with existing techniques, although their disease is still localized at the time of diagnosis and considered to be potentially curable. It is assumed that using new techniques to treat the localized disease, many of these patients could be cured.

---

1   **Linear energy transfer** (LET) or restricted linear collision stopping power (L_Δ) of charged particles in a medium is the quotient of *dE* by *dl*, where *dl* is the distance traversed by the particle and *dE* is the mean energy-loss due to collisions with energy transfers less than some specified value Δ [6]. LET is a positive quantity. LET depends on the nature of the radiation as well as on the material traversed.

1.2 Interaction of protons and heavy charged particles with matter

The fundamental difference between the interaction of photons and charged particles is that photons are being attenuated, i.e. the number of photons is exponentially decreasing due to absorption at the electrons in the atomic shell. Charged particles passing through tissue, however, slow down and gradually loose energy in atomic interactions until they come to rest. This reduces the energy of the particles, which in turn causes increased energy loss, reaching a maximum at the end of range and causing the maximum dose deposition within the target area. Radiative energy loss (Bremsstrahlung) can be completely neglected for proton or ion beams at therapeutic energies: several hundreds of MeV per atomic mass. (For proton, energy range is about 60-250 MeV that allows to reach 3-30 centimetres of depth, for carbon ions, energy range is about 200-500 MeV/amu).

The primary rationale for radiotherapy with heavy charged particles is this sharp increase of dose in a well defined depth (Bragg peak, see pic. **1.1.2**) and the rapid dose fall-off beyond that maximum.

Protons and ions in the clinical energy range have a substantial probability to undergo non-elastic nuclear interactions. These reactions basically remove particles from the primary beam and can be treated as attenuation mechanism. In addition, secondary particles are produced, which contribute to the dose especially outside the primary target region. The primary difference between proton and ion beams is that in the case of protons only target fragmentation occurs, while for ions projectile fragmentation is most important.
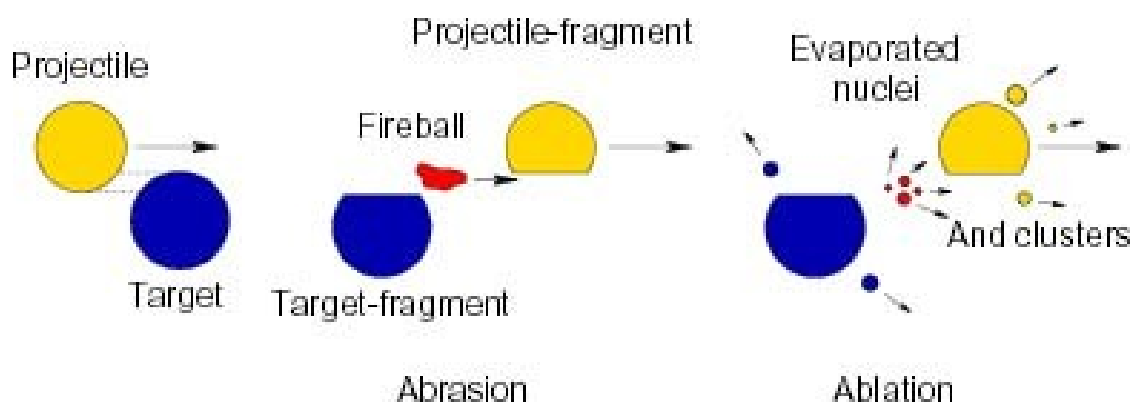
Pic. 1.2.1: *Schematic of the nuclear fragmentations [9].*

At energies of several hundred MeV per atomic mass unit which are required for radiotherapy applications, the radiation field is significantly affected by nuclear fragmentation processes with increasing penetration depths. The most frequently occurring nuclear reactions are peripheral collisions where the beam particles may lose one or several nucleons. This process can be described by the abrasion–ablation mode [10] as illustrated in figure **1.2.1**. Nucleons in the overlapping zone of the interacting projectile and target nuclei are abraded and form the hot reaction zone (fireball), whereas the outer nucleons (spectators) are only slightly affected by the collision. In the second step (ablation), the remaining projectile and target fragments as well as the fireball de-excite by evaporating nucleons and light clusters. Those emitted from the projectile fragments appear forward peaked in the laboratory frame due to the high velocity of the projectile. The projectile-like fragments continue travelling with nearly the same velocity and direction, and contribute to the dose deposition until they are completely slowed down or undergo further nuclear reactions. Neutrons and clusters from target-like fragments are emitted isotropically and with much lower velocities. The particles ablated from the fireball cover the range between the projectile and target emission. Nuclear fragmentation reactions lead to an attenuation of the primary beam flux and a build-up of lower-Z fragments with increasing penetration depth. The lower-Z fragments have longer ranges than the primary ions as the range of particles (at the same velocity) scales with A/Z^2. The impact of nuclear fragmentation on depth-dose profile of heavy-ion is shown in pic. **1.2.2**. With increasing penetration depth the peak-to-entrance dose ratio becomes gradually smaller, mainly caused by the exponentially diminishing of primary ions. The build-up of lower-Z fragments is clearly visible in the dose tail behind the Bragg peak at larger depths. Additionally the Bragg peaks are increasingly broadened by straggling.
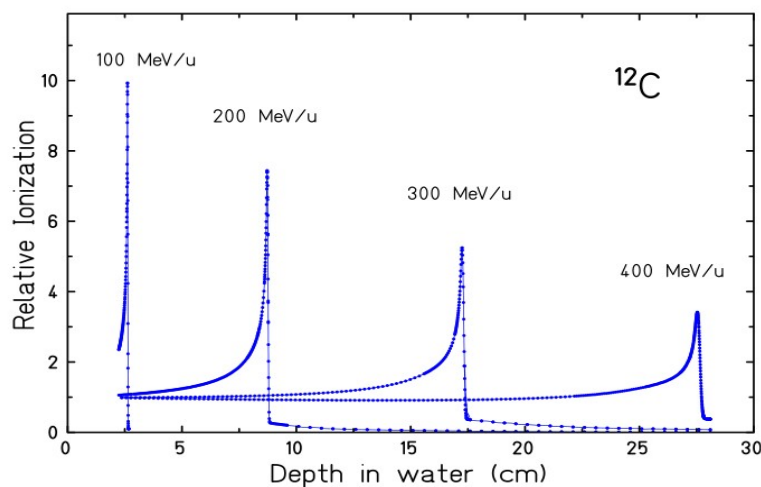
Pic. 1.2.2: *Measured Bragg curves of ¹²C ions stopping in water [7].*

1.3 Interaction of radiations with biological matter

When ionizing radiation interacts with cells, critical parts of the cell may be hit. Usually the chromosomes in the cell nucleus are considered to be the most critical part of the cell since they contain the genetic information and instructions required for the cell to perform its function and for reproduction purposes. The most important effect of radiation is thus on the DNA molecule, which is the main constituent of the chromosomes. On the other hand, there are very effective repair mechanisms at work within the cells of a human body, which constantly repair cellular damage, including chromosomal damage. There are different possible effects of radiation on cells. Some ionizing events produce substances not normally found in the cell. These can lead to a breakdown of the cell structure and its components. Cells can repair the damage if it is limited. Even damage to the chromosomes is usually repaired. If a damaged cell, however, needs to perform a function before it has had time to repair itself, it will either be unable to perform the repair function or it will perform the function incorrectly or incompletely. The result may be cells that cannot perform their normal functions or that now are damaging other cells. These altered cells may be unable to reproduce themselves or may reproduce at an uncontrolled rate. Such cells can be the underlying causes of cancers.

If a cell is extensively damaged by radiation, or damaged in such a way that reproduction is affected, the cell may die. Radiation damage to cells depends on how sensitive the cells are to radiation.

If radiation interacts with the atoms of the DNA molecule, or some other cellular component critical to the survival of the cell, it is referred to as a **direct effect**. Such an interaction may affect the ability of the cell to reproduce and, thus, to survive.

If a cell is exposed to radiation, the probability of the radiation interacting with the DNA molecule is very small since these critical components make up such a small part of the cell. However, each cell, just as is the case for the human body, is mostly water. Therefore, there is a much higher probability of radiation interacting with the water that makes up most of the cell's volume. When radiation interacts with water, it may break the bonds that hold the water molecule together, producing fragments such as hydrogen (H) and hydroxyls (OH).These fragments may recombine or may interact with other fragments or ions to form compounds, such as water, which would not

harm the cell. However, they could combine to form toxic substances, such as hydrogen peroxide (H_2O_2), which can contribute to the destruction of the cell. This mechanism is called **indirect radiation effect** .

High-LET radiation (i.e. alpha-particles, neutrons, protons) are densely ionizing radiation since they lose the energy throughout a small distance, causing dense ionization along their track with high localized multiple DNA damage. Low-LET radiation, such as X and γ-rays, are sparsely ionizing radiation since they produce ionizations sparsely along their track and, hence, almost homogeneously within a cell.

A basic difference between high and low LET radiations is that the amount of direct radiation damage is strongly increased in the case of high LET radiation as compared to low LET. Besides, biological effects of high LET radiations are in general much higher then those of low LET radiations with the same energy, because the higher concentration of deposited energy can cause more severe damage to any microscopic structures near the particle track.

During the formation of radicals, the presence of oxygen plays an important role for the radiation damage. In the presence of oxygen, the radiolysis of water is different and different radicals are formed like the hydroperoxy free radical or organic hydroperoxy free radicals, which are more stable and have longer lifetimes. This stabilization of radicals in the presence of oxygen leads to a higher probability of clustering of radiation damages, which are less likely to be repaired by the cell. Consequently, dissolved oxygen in tissue increases the amount of radiation damage, at least for low LET radiation.
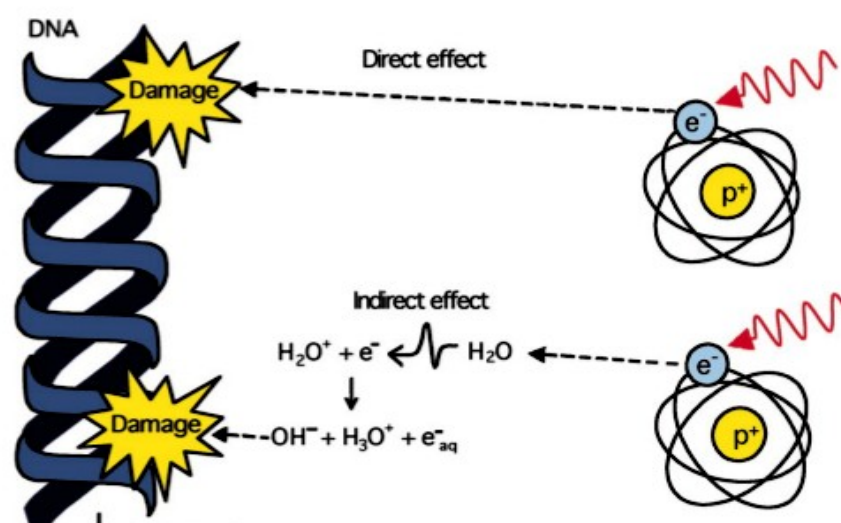
*Pic. 1.3.1: Direct and indirect effect of radiation on cell DNA.*

Human solid tumours are invariably less well-oxygenated than the normal tissues from which they arose, because the blood perfusion in the central part of the tumour is reduced. This so-called tumour hypoxia leads to resistance to radiotherapy and anticancer chemotherapy as well as predisposing for increased tumour metastases [11]. A major part of the resistance, though perhaps not all, is the result of the physicochemical free radical mechanism of the oxygen effect in sensitizing cells to ionizing radiation. Since generally indirect radiation damage is less important for high LET radiation, also the oxygen concentration in tissue is less important for high LET radiation, as can be observed in pic. **1.3.2**, where the survival curves of human kidney T-1 cells are shown, for X-rays and carbon ions with different LET, both with oxygenated and hypoxic cells. For each radiation, at the same dose the survival of hypoxic cells is higher than that of oxygenated cells. However the difference in the survival rates of oxygenated and hypoxic cells in the case of X-rays and carbon ions of low LET (33 keV/µm) is similar, while it is lower in the case of high LET carbon ions (118 keV/µm).

To quantify the influence of oxygen concentration on the survival of cells, the oxygen enhancing ratio (OER) quantity is used, which is the ratio of doses needed to achieve the same biological effect in hypoxic and well oxygenated cells.

$$OER = \frac{D_{hypoxic}}{D_{oxygenated}}$$

In pic. **1.3.3** some measured data on the oxygen enhancing ratio in V79 cells as a function of the LET are shown. It is seen that at very high LET values an OER=1 is reached, which means that the doses needed to achieve the effect is independent on the oxygenation of the cells.

In other words, high-LET radiation offers a potential benefit for the treatment of hypoxic tumours which are resistant to the traditional radiotherapy with low-LET radiation.
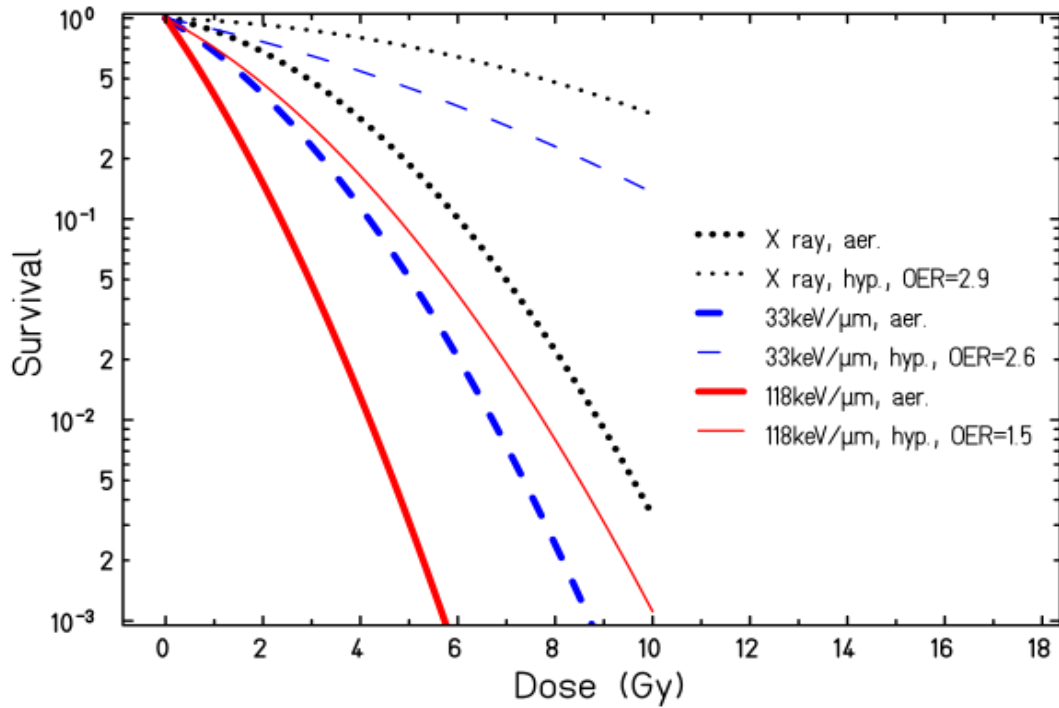
Pic. 1.3.2: *Survival curves of human kidney T-1 cells for X-rays and carbon ions with different LET, both with oxygenated and hypoxic cells [7].*
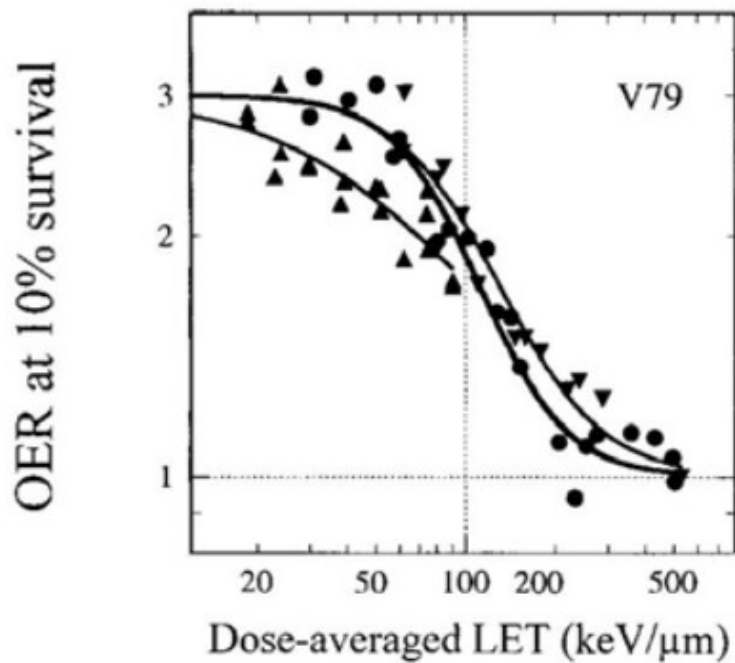
Pic. 1.3.3: *OER as a function of LET measured at 10% survival using Helium (triangles up), Carbon (circles) and Neon ions (triangles down), (reproduced from [12]).*
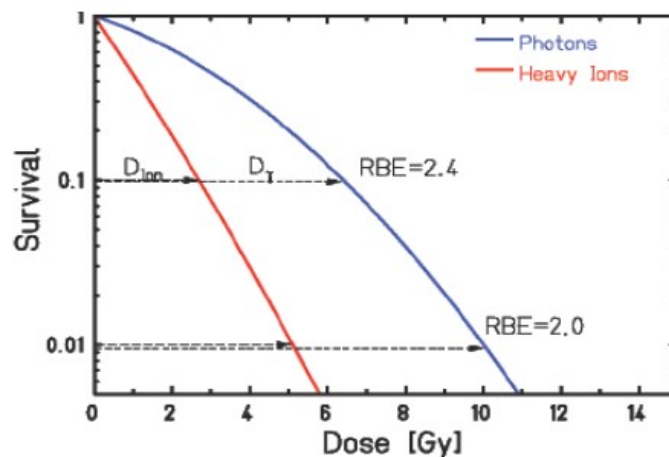
1.4 Relative biological effectiveness (RBE)

It is a general finding that the necessary doses to produce a certain biological effect using radiation with a higher linear energy transfer (LET) are lower as compared to photon radiation. To quantify this effect, cell survival measurements are performed [4]: when a Petri dish with N_0 cells is irradiated, only a fraction N cell cultures will survive at a given dose level. This fraction $S=N/N_0$ is called the surviving fraction and can be determined by counting the cells under a microscope.

The cell survival plotted as a function of the applied dose is called cell survival curve and exhibits a typical shouldered form (see Fig. **1.4.1**). While generally, the photon survival curves show a distinct curvature (the so-called *shoulder*), high LET radiation shows a nearly straight line (plotted in logarithmic scale).

The linear-quadratic model (LQ model) is the most common way to parametrize the cell survival curve S:

$$S(D)=\exp\left(-\alpha D-\beta D^2\right)$$

where D is the absorbed dose and α and β are experimentally determined parameters. The ratio α/β determines the shoulder of the survival curve.

Pic. 1.4.1: *Survival curves for photons and heavy ions and RBE values at various effect levels [5].*

The largest experience on the biological effectiveness of radiation is coming from photon radiation. This is the case for in vitro data but even more for clinical data.

Consequently, in order to transfer this experience from photon to high LET radiation, the relative biological efficiency (RBE) was introduced:

$$RBE = \frac{D_{photon}}{D_{ion}}$$

Here, D_{photon} and D_{ion} are the absorbed doses ($D = \frac{\Delta E}{\Delta m}$) for photons (reference radiation) and high LET radiation, which lead to the same biological effect, respectively. The RBE depends on the radiation quality and tissue-specific response as well as the biological end point and the dose level of the radiation, i.e. the level of survival.

The RBE is an important quantity, as the iso-effective dose of a proton or ion irradiation can be determined as the product of the absorbed dose multiplied by the RBE. This iso-effective dose is equally effective as the same dose delivered with the reference radiation, i.e. photons.

1.5 Treatment planning and dose conformation

The process of minimizing the dose delivered to normal tissue, trying to maximize it in the tumour area, is a process called "dose conformation".

The first step of treatment planning for any radiation therapy modality is to define and delineate the target volume on the basis of modern imaging techniques.

The target volume as well as critical structures are delineated manually in different slices. From these contours a 3D model of the treatment geometry is constructed, which is used to find suitable beam entrance ports under the condition that the traversal of critical structures should be avoided. For protons and heavier ions only few entrance ports (typically 2 nearly opposing fields) are necessary in most cases because of their superior depth-dose characteristics. Thereby radio-sensitive organs can be spared to a maximum extent.

After target definition the dose distribution has to be adapted to the planned target volume, which ideally should be covered completely by 100% of the prescribed dose, while the dose in organs at risk should be minimized. For protons the optimization commonly is restricted to absorbed dose only, applying a constant RBE value of 1.0–1.1 [6]. For ion-beam therapy the biological effective dose has to be optimized, which is a difficult task in view of the manifold dependencies of RBE and the complex radiation field.
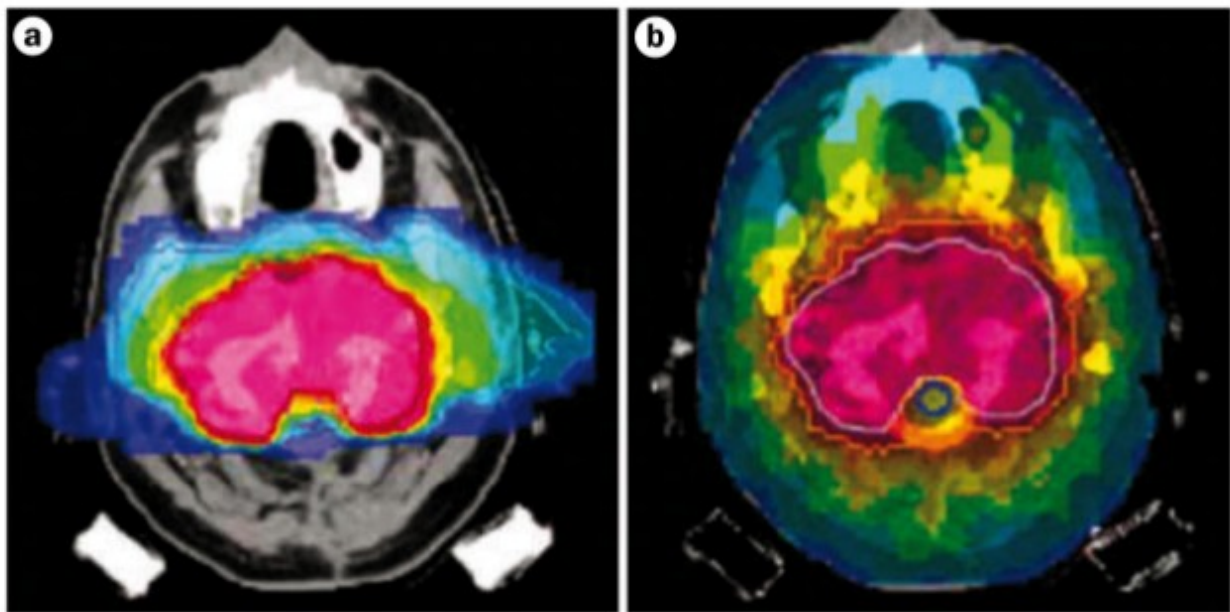
Pic. 1.5.1: *Comparison between the results of a treatment plan for a large volume at base of the skull. a) plan for a carbon ions. b) plan for photons.*

To evaluate the absorbed dose, the concept of RBE proves extremely helpful. By properly predicting the RBE for each position in the treatment field, the required physical dose can be determined and the appropriate primary particle fluence can be applied. However, RBE has complex dependencies covering a wide range of parameters, therefore RBE determination require biophysical modelling, since it is not feasible to experimentally determine the RBE for all possible parameter combinations even for *in vitro* measurements. The lack of knowledge about basic mechanisms, and the absence of rigid quantitative data necessary as input for the models, prohibit the achievement of required model accuracy. Therefore, simplified models needed to be developed to include RBE either based on some experimental heavy-ion data or by transferring the experience with conventional radiation to the case of ions. The complexity of RBE issue also impacts the definition of the biologically or clinically relevant dose. The RBE values used in therapy depend on

the applied biophysical model, so there is not a common definition. The relevant dose has been named and determined differently at every heavy-ion treatment centre.

The approach used at Lawrence Berkeley Laboratory (LBL) was based on a large data set of measured RBE values which was exploited as input to design the beam shaping device[13, 14, 15, 16]. At HIMAC and HIBMC in Japan, a similar method is applied to shape the ridge filter system in order to achieve a homogeneous biological response [17, 18]. The most recent approach developed at GSI and currently applied at Heidelberg facility (HIT) and at CNAO relies on the local effect model (LEM), which predicts RBE values using the photon dose-response curve of the system, the physical dose distribution around single ion tracks, and the cell nucleus as the sensitive target [19, 20].

The implementation of active energy variation and raster scanning for carbon ions opened the pathway for individually optimized tumour conformity for each patient without the need of additional customized passive beam shaping devices. This breakthrough in beam delivery poses a new challenge for biological treatment planning in order to fully exploit the new potential. For this purpose, the local effect model was developed at GSI. It calculates RBE values for each position in the treatment field and facilitates the application of complex 3D volumes with a homogeneous photon-equivalent dose. The local effect model relates the response of biological systems following ion irradiation to the corresponding response after X-ray irradiation. It assumes that the biological effect of irradiation is entirely determined by the spatial local dose distribution inside the cell nucleus. The accumulated local dose in the cell nucleus from different tracks is calculated for small sub-volumes individually using a track structure model. The local effect model uses an amorphous track structure description which assumes that the track consists of an inner part with a constant initial dose attached to an outer part following a $1/r^2$ dependence. It can be expressed by:

$$D(r) = \begin{cases} \dfrac{\lambda\, LET}{r_{min}^2}, & r < r_{min} \\[2ex] \dfrac{\lambda\, LET}{r^2}, & r_{min} \leq r \leq r_{max} \\[2ex] 0, & r > r_{max} \end{cases}$$

where LET denotes the linear energy transfer and λ is a normalization constant to assure that the

radial integral reproduces the LET for a medium with density ρ.

With knowledge of the deposited dose, the resulting biological damage is extrapolated from data of X-ray experiments for each sub-volume and integrated over the entire cell nucleus.
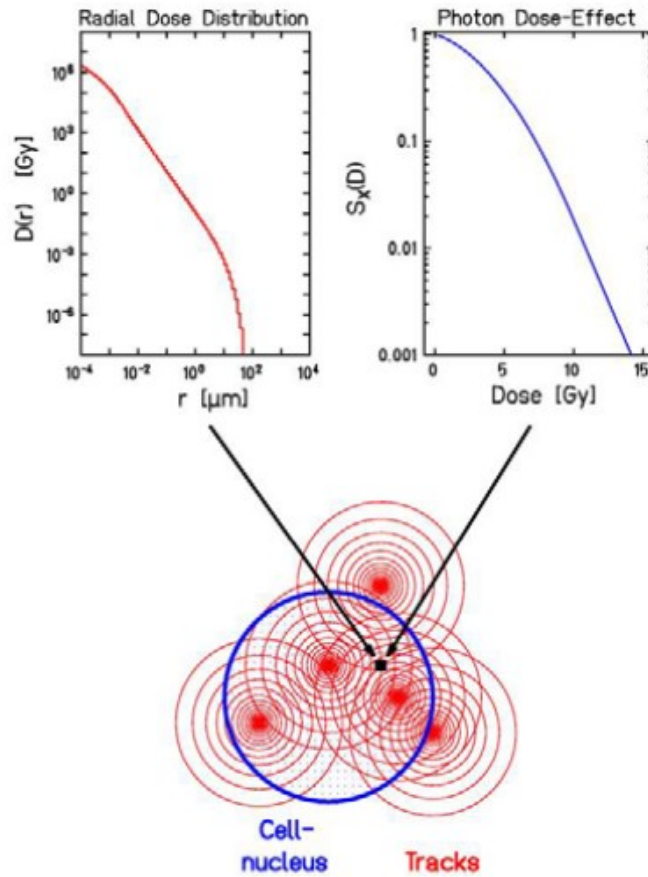
Pic. 1.5.2: Basic idea of the local effect model (LEM): the radial dose distributions of single ion tracks are superimposed to the cell nucleus. Using the photon dose response on a microscopic level, the survival for ion beams is calculated (reproduced from [21]).

2. Fundamentals of Microdosimetry

2.1 Microdosimetry and conventional dosimetry

Microdosimetry is formally defined by Rossi and Zaider as "the systematic study and quantification of the spatial and temporal distribution of absorbed energy in irradiated matter"[23]. In this way it's possible to evaluate the inhomogeneous and stochastic nature of interactions. Not only the average energy deposited per unit mass (i.e. the absorbed dose), but the number of energy deposits, their magnitude and their spatial distribution influence the effect of radiation on biological structures [22].

Conventional dosimetry refers to the dose absorbed as energy released on a macroscopic volume, but in many situations it is inadequate in describing the effect of radiation on biological materials.

The main difference between microdosimetry and classical dosimetry is the usage of stochastic quantities.

Radiations which differ in the number, size and distribution of energy deposit cause different effects for the same absorbed dose. This is observed in the case of biological effects and is usually quantified in the term relative biological effectiveness (RBE) for a given radiation.

Our understanding of these differences between radiations begins with an appropriate description of the manner in which the energy is initially deposited. This description requires detailed information on the structure of the tracks generated in an irradiated medium.

If we wish to improve our understanding of radiation effects, concepts must be developed which relate some of the principal features of the absorption of ionizing radiation in matter to the size and perhaps the nature of the structures being affected. This is the objective of microdosimetry.

2.2 Microdosimetric Quantities

Microdosimetric quantities are defined in the International Commission Radiation Units and Measurements report 36 [22].

The fundamental dosimetric quantity is the *energy imparted* ε to the matter in a volume.

$$\epsilon = \sum_i \epsilon i$$

ε is a stochastic quantity and the energy deposits over which the summation is performed may be due to one or more energy deposition events. The *energy deposit*, ϵ_i in a single interaction is defined as:

$$\epsilon_i = E_0 - E_1 + Q$$

where E_0 kinetic energy of the incident ionizing particle, E_1 the sum of the kinetic energies of all ionising particles leaving the interaction volume and Q includes the changes in the rest mass energy of the atom and all particles involved in the interaction.

The *specific energy* imparted, *z*, is the quotient of ε by *m*, where ε is the energy imparted by ionizing radiation to matter of mass *m*.

$$z = \frac{\epsilon}{m}$$

The unity of z is the gray: 1 Gy=1 J Kg^{-1}

z is a stochastic quantity. It is useful to consider the probability distribution of *z*. The value of the distribution function, *F(z)*, is the probability that the specific energy is equal to or less than *z*. The probability density, *f(z)*, is the derivative of *F(z)* with respect to *z*:

$$f(z) = \frac{dF(z)}{dz}$$

The expectation value, $\bar{z} = \int_0^\infty z f(z) d(z)$ is called *mean specific energy* and it is a non-stochastic quantity. Specific energy may be due to one or more energy deposition events. The number *n* of energy deposition events which have contributed to a particular specific energy *z*, is in general distributed at random and may be described by a Poisson distribution.

The *lineal energy*, y, is the quotient of ε by *l,* where ε is the energy imparted to the matter in a volume by a single energy-deposition event, and *l* is the mean chord length in that volume:

$$y = \frac{\varepsilon}{l}$$

The unity of the lineal energy is keV μm⁻¹.

The mean chord length in a volume is the mean length of randomly oriented chords in that volume. Various type of randomness exist and the definition of *l* typically refers to randomness in which the body is exposed to a uniform, isotropic field of straight infinite lines. Other types of randomness exist and are associated with other mean chord lengths [24]. The lineal energy depends on the mean chord length of the collecting volume. The mean chord length may be calculated using the formula provided by Cauchy, which states that for any convex body in a uniform isotropic field of straight infinite lines, the mean chord length is equal to 4V/S, where V is the volume and S the surface area. For geometries commonly used in microdosimetric experiments, right cylinder and sphere, the mean chord length has the same value, while the distribution of chord length is quite different.

$$l_{sphere} = \frac{4V}{S} = \frac{2}{3}d \qquad\qquad l_{cylinder} = \frac{4V}{S} = \frac{2}{3}d$$

The lineal energy is a stochastic quantity. It is useful to consider the distribution function of y. The value of the distribution , *F(y)*, is the probability that the lineal energy is equal or less than y. The probability density *f(y)* is the derivative of *F(y)* with respect to y:

$$f(y) = \frac{dF(y)}{dy}$$

It is also called *lineal energy distribution.* It is important to keep in mind that y is defined for a single energy-deposition events only. The lineal energy distribution *f(y)* is independent of the absorbed dose.

The expectation value, $\bar{y}_F = \int_0^\infty y f(y) dy$ is called *frequency-mean lineal energy* and it is a non-stochastic quantity that corresponds to the concept of LET (linear energy tranfer). Another useful quantity is the dose distribution of y. Let *D(y)* be the fraction of absorbed dose delivered with lineal energy less than or equal to y. The dose probability density *d(y)* is the

derivative of *D(y)* with respect to y: $d(y) = \frac{D(y)}{dy}$

The distribution $d(y)$ is independent of the absorbed dose. The expectation value $\bar{y}_D = \int_0^\infty y\, d(y)\, dy$ is called *dose-mean lineal energy*, and it is a non-stochastic quantity. The relationship between $d(y)$ and $f(y)$, and between $\bar{y}_F$ and $\bar{y}_D$ is: $d(y) = \dfrac{y}{\bar{y}_F} f(y)$ and $\bar{y}_D = \dfrac{1}{\bar{y}_F} \int_0^\infty y^2 f(y)\, dy$

Although it seems similar, *lineal energy* is a different concept from LET. LET only describes energy loss occurring along the trajectory of the primary charged particle. In this sense, energy deposition can only be described when the particle intercepts a point or volume of interest. It neglects the radial dimensions of a track caused by secondary electrons (delta-rays) that can have considerable range when the velocity of the heavy particle is large. In radiation biology, differences in the relative biological effectiveness (RBE) of different ions is attributed, in part, to differences in the LET of the radiation. The energy distribution of electrons ejected from the path of the primary ion depends on the velocity of the incident particle, but not on its charge. Because particles with different charge but similar LET must have different velocities, one might expect that RBE might not be dependent on LET alone, as is confirmed by radio-biological experiments. For radiation protection, a radiation weighting factor, w_r, has been defined to compensate for differences in RBE between different types of radiation [25]. Multiplying the absorbed dose by the proper radiation weighting factor yields an equivalent dose that relates a risk to the specific exposure. For mixed fields and for radiations without a defined w_r, the ICRP gives a formula for calculating a radiation quality factor, Q, which is a function of the LET of the incident particle, Q(LET). In this contest, energy deposition spectra measured by TEPCs can be used to calculate absorbed dose and to estimate the average quality factor of unknown radiation fields. In these analysis, it is assumed that lineal energy, y, is numerically equivalent to LET. Thus the measured distribution $f(y)$ is assumed to be a direct measurement of LET spectrum. However, comparison of measurements of $f(y)$ with a TEPC and $f(LET)$ using a particle spectrometer indicate that there are major differences between the two distributions [26]. This can cause large uncertainties in the corresponding estimates of quality factor.

Experiments has also been performed to use y_D and y_F as an esteem for the LET in radio-protection [27], founding that the frequency mean lineal energy, y_F, was about 8–15% lower than the corresponding value of LET for all ions, while y_D was within 10% of LET for Z = 6 to 26. However, y_D was about 50% greater than LET for ^{4}He. Previous results showed that y_D was more than a factor of two greater than LET for protons [28]. A way to avoid these problems should be to replace the current definition of quality factor based on LET with Microdosimetric Event-based

approach, as suggested by ICRU [29] and developed by A. M. Kellerer [30] introducing a specific quality function *q(y)* to weight microdosimetric spectra:

$$q(y) = \int q(y) d(y) dy$$

problems with this approach include the validation of the *q(y)* function for all types of radiations and energies and corrections for various wall effects which could distort the measured *y* spectra [52, 53]

2.3 Evaluation of quality of a radiation field and weighting function

Radiation quality can be described either by radiometric or by dosimetric quantities. Radiometric quantities, however, may not be directly related to the mechanisms that determine the radiation effects. The specification of radiation quality for purposes of biophysics is not in terms of the radiations as such, but of energy which they deposit locally in individual events. Microdosimetric specifications of radiation quality include formulations related to track structure of charged particles or to energy deposition in small volumes.

Ionizations created by a radiation within a biological tissue, trigger a chain of events that leads to the biological damage in a manner not fully understood, yet.

Microdosimetry offers a way to evaluate RBE (see sec. **1.3**) of a therapeutic beam thanks to a response function called biological weighting function **r(y)**. [32, 33].

This function assigns to the different parts of a microdosimetric spectrum, a different biological weight, making possible to determine the quality of the beam investigated:

$RBE_c \cong \int r(y) d(y) dy$ where the subscript *c* stands for calculated.

d(y)dy comes from microdosimetric measurements.

The advantages obtained with this procedure come from the fact that only with physical measurements it is possible to determine the beam quality; in fact the acquisition of

microdosimetric spectra is cheaper, faster and more easily reproducible than a series of radio-biological measurements.

From the **r(y)** function, using microdosimetric spectra, it is possible to establish the RBE of a radiation field even in situations of irradiation really complex, in which taking radio-biological measurements it is not possible. The complexity of the therapeutic radiation fields includes variations in ion energies and fragmentation of projectiles as well as target atoms.

Thirty years ago, in the context of an European program, several microdosimetric and radio-biological measurements were taken simultaneously in radiotherapy centres of all Europe, to investigate the relationship between physical and biological effects, and to obtain the **r(y)** function [33].

The weighting function **r(y)** has been calculated from radio-biological measurements of RBE and from microdosimetric measurements of the considered beam. It attributes a different "weight" to every part of the microdosimetric spectrum, with a constant trend of unitary value from 0 keV/μm to 10 keV/μm, corresponding to the maximum of the energy released by a photon radiation. Since 10 keV/μm to 70-80 keV/μm, **r(y)** increases in a rapid way from 1 to about 4.5, than decreases again because as the ionization events become larger, they deposit more energy than what is needed to produce a biological effect (as cells death). Part of the deposit energy is therefore "wasted", because a greater dose than needed is deposited for the same biological effect.

Initially, **r(y)** was calculated for fast neutrons beam [33], and then was verified that the same weighting function can be used also for protons beam [32, 34]. It was esteemed with in-vivo radio-biological measurements, and microdosimetric spectra simulating chromosomal dimensions: 1-2μm.

Dose prescriptions in proton therapy are obtained by dividing the dose used in conventional photon therapy by an appropriate RBE to obtain the physical proton dose to be delivered to a patient. The proton RBE in clinical use is 1.1, which is assumed to be independent of the incident proton energy and depth. Radio-biological measurements have however proved that the RBE in the SOBP[2] used in proton therapy is not constant, strongly increasing in the distal part of the SOBP.

In pic. **2.3.1** RBE microdosimetric values at different depths are plotted together with the relative

---

2   SOBP stands for Spread Out Bragg Peak. Mono-energetic Bragg peaks are usually not wide enough to cover most treatment volumes. By superimposing a set of beams with decreasing energies and weights, a *Spread out Break Peak* (SOBP) is generated, which delivers the desired dose to the whole treatment volume.

dose and two sets of radio-biological data collected by using the therapeutic proton beam of Nice [34].

For these reasons, evaluation of RBE through the **r(y)** function are extremely important and may provide a way to calculate more accurately the RBE of protons at different energies and depth.
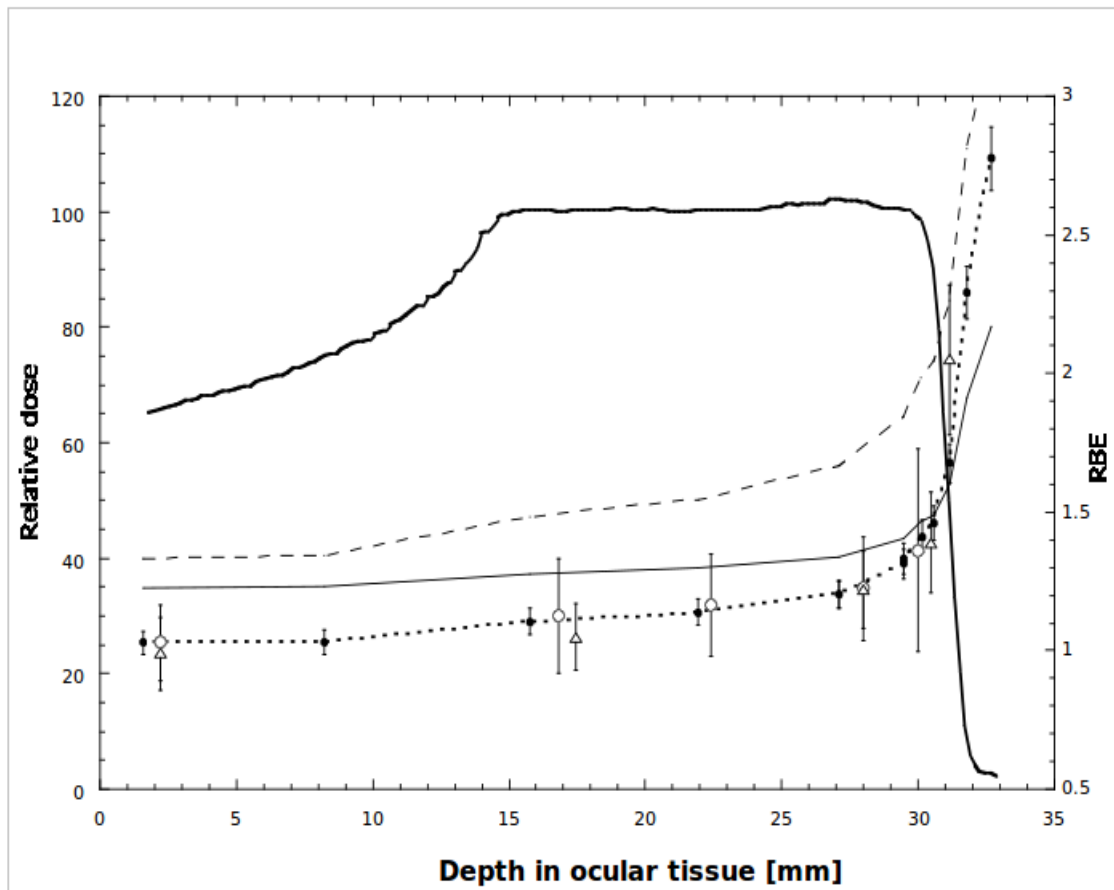
Pic. 2.3.1: *Comparison of radio-biological RBE and microdosimetric RBE$_\mu$. Open triangles: RBE for human tongue cell carcinoma at 2 Gy. Open circles: RBE for human melanoma cells at 8 Gy. Full dots with dotted line: RBE$_\mu$ for early damage in mouse crypt cells at 8 Gy with Loncol's weighting function. Continuous thin line: RBE$_\mu$ for early damage in mouse crypt cells at 10 Gy with Tilikidis's weighting function. Dashed line: RBE$_\mu$ for early damage in mouse crypt cells at 2 Gy with Tilikidis's weighting function[34].*

In picture **2.3.2**, the **r(y)** functions published in literature are shown. All of them are extracted from 2 μm microdosimetric spectra. Tilikidis and colleagues have published two **r(y)** functions (for 10 Gy and 2 Gy) for early effects in mouse intestinal crypt cells [31]. Pihet, Loncol and colleagues have published a **r(y)** function for the same biological end point and for 8 Gy [32, 33]

27

Attempts to apply the weighting function **r(y)** derived from the neutron experience to therapeutic carbon beams have leaded to RBE estimates not always in agreement with those derived from the application of the LEM model [36].
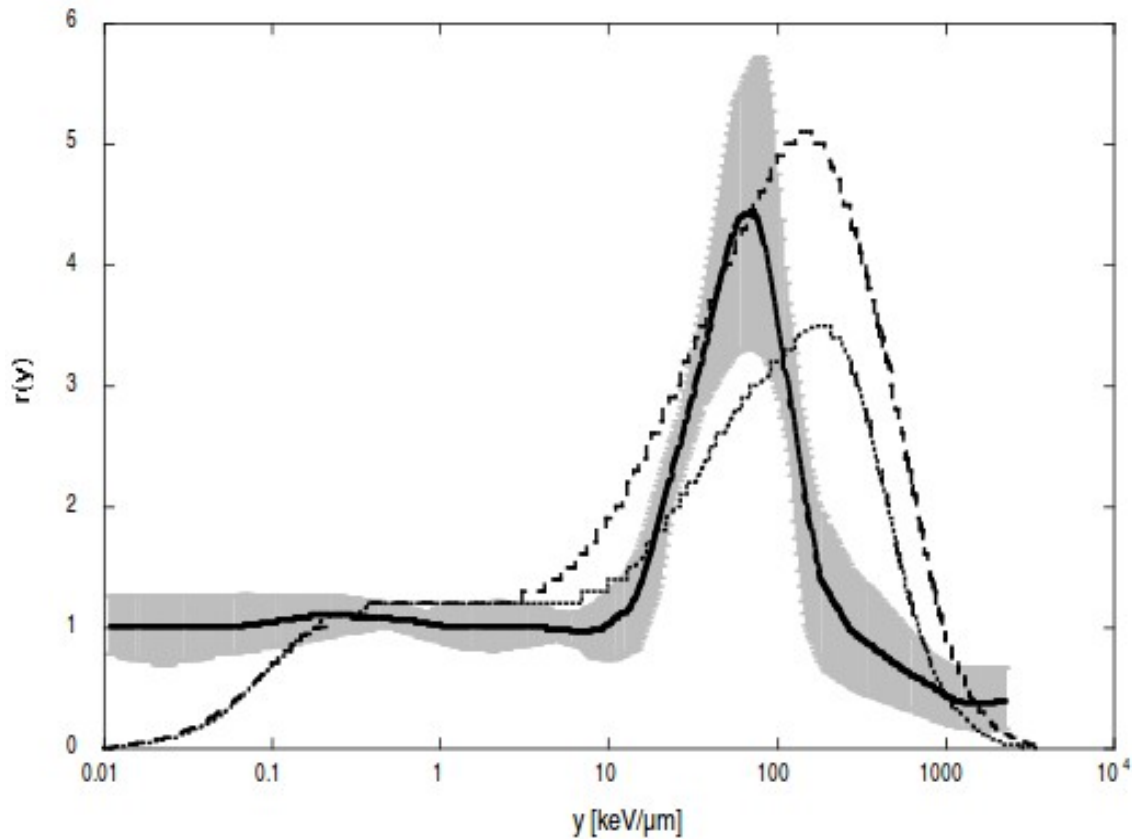
Pic. 2.3.2: *Weighting function for early damage in mouse crypt cells. Thick line: 8 Gy Loncol's [32]. The grey stripe around the line is the overall uncertainty ± 1 standard deviation (SD). Dashed line: 2 Gy Tilikidis's [31]. Dotted line: 10 Gy Tilikidis's [31]. The picture is taken from [34].*

This can be due to the fact that particles of equal LET but different velocity exhibit equal values of lineal energy density, but may have substantially different RBE. At equal LET, the fast carbon ions tend to be faster than recoil protons released by neutrons, i. e. their tracks are less narrow and the saturation effect will therefore become important at higher values of LET, i. e. the weighting function for carbon ions should be shifted toward larger values of linear energy. Another crucial aspect is the fragmentation of the primary beam projectile and target atoms. One needs to study the potential distortion of the microdosimetric distributions due to simultaneous traversal of the detector by pairs of fragments. Further studies are required to evaluated a weighting function for carbon ions.

2.4 Microdosimetric kinetic model

To be integrated into a treatment planning system, experimental data have to be accurately reproduced by a model, which can predict survival values at any dose. In the field of radiotherapy with ions (hadron-therapy), cell survival depends not only on dose, but also on ion species and ion energy. Consequently, a complex model is needed in order to take into account for the biological dependence of the radiation. However the complexity of the radiochemical and radio-biological mechanisms involved in the formation of biological damages complicates the elaboration of such models. Most of the recent models are based on micrometric and nanometric scale calculation. Among others, two models have been the subject of study and development in the context of applications to hadron-therapy treatment planning. These models are the Local Effect Model (LEM) [see sec. **1.5**] and the Microdosimetric Kinetic Model (MKM).

The MK model was originally developed by Hawkins [37], based on the concept of the theory of dual radiation action [38]. The basic assumptions employed in the models are that (i) a cell nucleus can be divided into many sub-cellular structures with the size of 0.5 –1.0 µm, so-called *domain*, (ii) primary DNA lesions diffuse throughout the domain by random flight and (iii) a cell dies when radiation directly induces an unalterable lethal lesion, or some primary lesions combine in pairs to form a lethal lesion. Based on these assumptions, it was theoretically derived that the average number of lethal lesions in a domain can be given by a linear- quadratic (LQ) correlation with a specific energy z in the domain.

The model was recently improved by Kase et al. [41, 42] in terms of the saturation correction for expressing the decrease of RBE owing to the overkill effect. In the improved model, the cell-survival fraction for any type of radiation can be expressed as a function of only one parameter: the saturation-corrected dose-mean lineal energy in domains, referred to as y^* in ICRU 36 [22] which can be derived from microdosimetric spectra. According to the LQ model, the survival fraction of cells irradiated with the absorbed dose D can be expressed by the equation:

$S = e^{-\alpha D - \beta D^2}$ where S is the survival fraction, and α and β are parameters depending on the cell lines and dose rates as well as the profiles of radiation such as energy, charge, speed and LET in a complicated manner. In the MK model, the parameter β can be regarded as a constant, and its numerical value can be obtained from the survival curve of the cells irradiated by a reference radiation. The parameter α can be estimated from the obtained β by the equation : $\alpha = \alpha_0 + \beta z^*_{1D}$

where α_0 is a constant that represents the initial slope of the survival fraction curve in the limit of LET=0, i.e. in the condition that deposition energies are so sparse that no primary lesions interact with one another. The parameter z^*_{1D} denotes the saturation-corrected dose-mean-specific energy in the domains, and can be calculated as: $z^*_{1D} = \dfrac{l}{m} y^*$ where l is the mean cord length, and m is the mass of the domain.

The MKM model is at present seriously considered by the National Institute of Radio-biological Science (NIRS) in order to adapt it to their treatment planning system [39, 40, 41, 42]

3. Experimental microdosimetry

3.1 TEPC: Tissue Equivalent-Gas Proportional Counter

The experimental apparatus to reproduce a site of micrometric size, is not of micrometric dimensions (making an exception for solid state microdosimetric detector, see par. **3.2** for examples), for obvious difficulties in construction. What is usually done, is to use a gas detector, filled with tissue-equivalent gas, at low pressure. In this way, with sensitive volumes of the order of the $10^{-2}/10^{-3}$ meters, it is possible to effectively simulate a micrometric site.

In the early 1950s the low-pressure proportional counter has been developed, the basic assumption of experimental microdosimetry is that the charge produced in small gas-filled cavities is generally considered to be a good measure for the absorbed dose in the surrounding material. [23]

For this reason, the simulation of microscopic regions is made using a geometrically similar gas volumes of equal effective dimensions. The gas composition, as well as the material of the cathode is Tissue-Equivalent to minimize distortion in calculations of deposited energy, accordingly with ICRU standard. Mass percentage composition of plastic-TE and common gas mixture TE used in microdosimetry are shown in Table **1** [22].

The most common material for the cathode is a plastic called A 150. The cathode has to be mechanically stable and electrically conductive, and these requirements are achieved using more carbon and decreasing the content of oxygen compared with a real biological tissue. Using carbon as a conductive replacement for oxygen is accepted because the differences in term of energy response for photons are negligible since the atomic numbers of oxygen and carbon are similar, furthermore they possess very similar neutron cross section for energies up to 10 MeV. The two gas mixtures based on methane and propane are composed by hydrogen, carbon, nitrogen and oxygen to be as similar as possible to the composition of the biological tissue. The propane mixture permits higher gas gains and is more homogeneous with plastic A-150, while the methane based mixture more closely models the ICRU muscle tissue composition.

Name	H	C	N	O	F	Na	Mg	Si	P	S	K	Ca
ICRU tissue, muscle	10,2	12,3	3,5	72,9	-	0,08	0,02	-	0,2	0,5	0,3	0.007
Plastic A 150	10,1	77,6	3,5	5,2	1,7	-	-	-	-	-	-	1,8
Methane-TE	10,2	45,6	3,5	40,7	-	-	-	-	-	-	-	-
Propane-TE	10,3	56,9	3,5	29,3	-	-	-	-	-	-	-	-

Table 1: Elemental composition of tissue-equivalent materials.

For this reason detectors are called Tissue-Equivalent Gas-Proportional Counters (TEPC). A proportional gas filled counter is a kind of ionisation chamber, filled with gas, to measure the charge of ions of one sign created by the radiation. Typical for these detectors is the phenomenon of gas multiplication which relies on the fact that the electric field within the counter is high enough to enable secondary ionisation, proportional to the amount of primary ionisation.

In general a TEPC consists of two electrodes: the wall of the counter is the cathode and the central wire the anode. Applying a helix around the anode provides a more uniform electric field along the anode, for a spherical counter. This type of counter is also known as Rossi counter due to the innovative design of Harold Rossi and his co-workers in mid-nineteen-fifties. A typical spherical TEPC (Rossi counter) with helix is shown in Pic. **3.1.1.**

Another way to attain a uniform electric field along the anode wire, for a spherical counter, without the use of a helix, is that to subdivide the cathode wall into several spherical sectors, biased at different voltages. This solution was recently adopted in the development of a special TEPC, called EuTEPC [51], for ESA (European Space Agency) to provide active personal dosimetry at the International Space Station. The EuTEPC cavity has a diameter of 5 cm and it is filled with low propane-gas density and sealed to operate for two years at the ISS without gas refilling.

TEPC is almost universally designed with a central anode surrounded by a cathode. In this configuration, the electric field becomes stronger in the vicinity of the anode. A positive potential applied to the anode causes electrons from ionising events to drift toward the anode. At a distance from the anode determined by the detector characteristics and applied voltage, these electrons will obtain a kinetic energy capable of ionisation of gas molecules between successive collisions. Moreover, the new electrons produced will also be capable of producing ionisation in the gas.
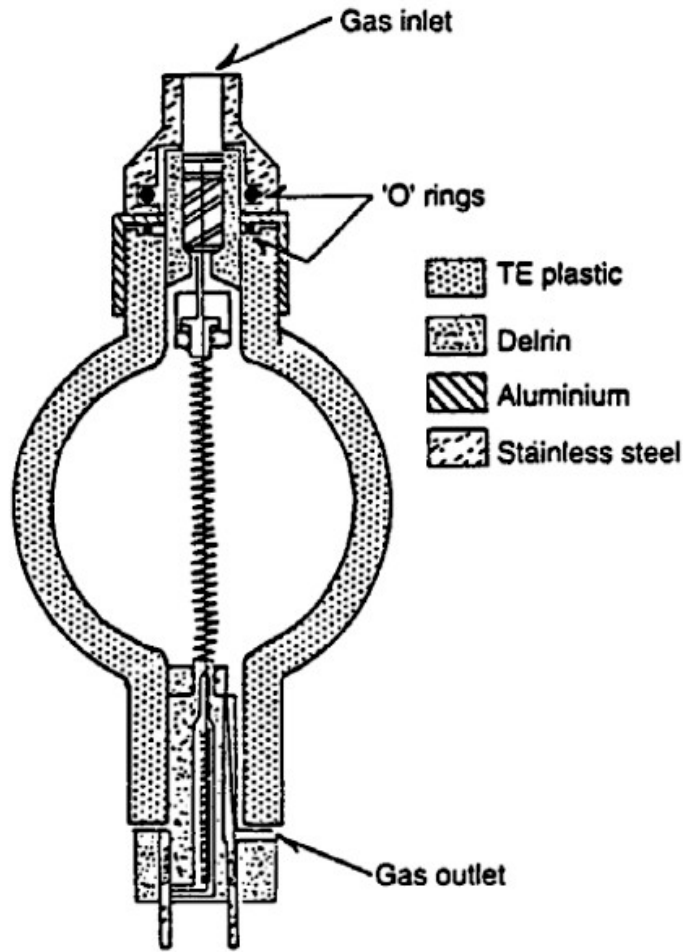
Pic. 3.1.1: A typical spherical Tissue-Equivalent Proportional Counter (TEPC) with helix. This counter is often called "Rossi counter"[23].

The gas multiplication process, which is generally based on the cascade of electrons, is expressed by the Townsend equation:

$$\frac{dn}{n} = \alpha\, dx$$

where n is the number of electrons and x is the distance, and α is the first Townsend coefficient and is defined as the mean number of secondary electrons produced by a free electron per centimetre of its path length. It depends on the counting gas, the gas pressure and the field strength.

The reduced ionization coefficient α/p depends only on the value of the reduced electric field strength E/p at a given location in space only in the case of equilibrium conditions. In such cases,

α/p can be wrote as: $\frac{\alpha}{p} = A \cdot e^{-B\left(\frac{p}{E}\right)}$ where A and B are the parameters gas-dependent, p is the pressure and E the electric field. Such conditions are fulfilled only in the case of uniform electric fields (not too strong) or for gases at high pressure in relatively weak non-uniform electric fields [46].

The electric field strength in low-pressure counters such as TEPC can be very strong and the field varies considerably over the electron mean free path. Electrons cannot reach the equilibrium energy distribution corresponding to the local electric field strength, as they would have in a uniform field of the same strength, and the corresponding α/p does not follow the changes in E/p (α/p becomes lower than that for equilibrium conditions). P. Segur et al [47] developed a so called "field gradient model" to take into account the effects of the variation of the field strength over the electron mean free path, resulting in an expression for α/p as that above, but with A and B coefficients which are pressure dependent.

To simulate a site of micrometer size, pressure of the gas inside the chamber must be properly chosen.

One of the principles of using a proportional counter in microdosimetry is the assumption that the spatial distribution of energy deposition in the gas-filled cavity is the same as in geometrically similar regions in the surrounding wall material when dimensions are inversely proportional to the density ratio.

The energy deposited by the particle in crossing the microscopic medium volume, E_m, is given by the product of the tissue mass stopping power, the tissue density and the path length across the medium volume, thus:

$$E_m = \left(\frac{1}{\rho}\frac{dE}{dx}\right)_m \rho_m \Delta X_m$$

The energy deposited by the particle in crossing the gas volume, E_g, is given in similar manner by:

$$E_g = \left(\frac{1}{\rho}\frac{dE}{dx}\right)_g \rho_g \Delta X_g$$
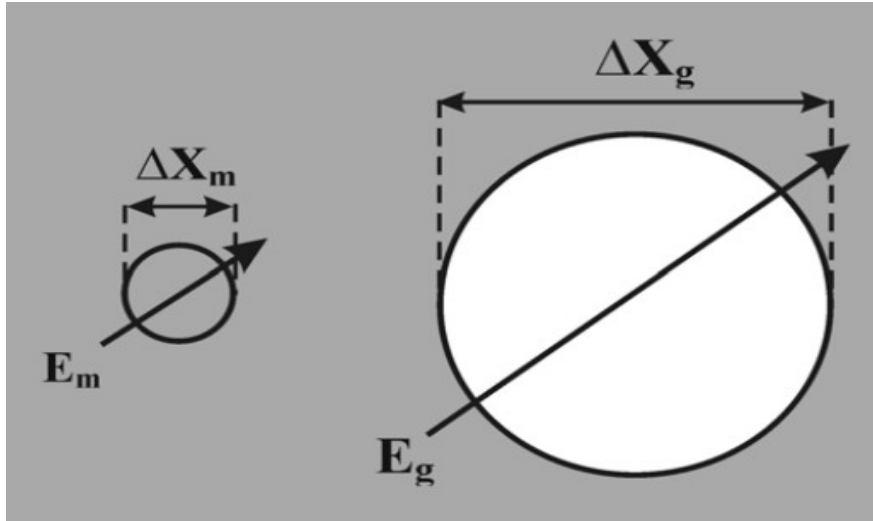
Pic. 3.1.2: Microscopic tissue site size simulation using a tissue equivalent gas cavity.

These two quantities must be equal if the energies deposited in medium and gas have to be the same:

$$\left(\frac{1}{\rho}\frac{dE}{dx}\right)_m \rho_m \Delta X_m = \left(\frac{1}{\rho}\frac{dE}{dx}\right)_g \rho_g \Delta X_g$$

When the mass stopping power of medium and used gas are the same, the condition required is thus:

$$\rho_m \Delta X_m = \rho_q \Delta X_q$$

If the product of the gas density and the gas cavity diameter is equal to the product of the tissue volume diameter and medium density, simulation of the microscopic medium volume is achieved.

However, the density difference between the cavity and the surrounding wall can lead to distortion of an experimental microdosimetric distribution even if the wall and the gas have the same atomic composition. These have been termed the wall effects [53]. Wall effects can be classified into four types (see pic. **3.1.3**):

a) *Delta-ray effect:* A primary particle enters the cavity with one of his delta rays, and the distance between the two particle is such that only one would enter the real tissue volume. This effect is most significant for high-energy heavy charged particles and for high energy electrons.

b) *Re-entry effect:* An electron may re-enter the cavity after it has crossed it, due to its curved path,

while it wouldn't re-enter the real tissue volume. Most significant for electrons, while it's generally negligible for heavy particle.

c) *V-effect:* Two heavy charged particle from a inelastic nuclear interaction form a V sharp pattern.

d) *Scattering effect*: An uncharged primary particle may undergo interaction producing charged particle close enough to both enter the cavity, while in the real microscopic region they are not close enough.
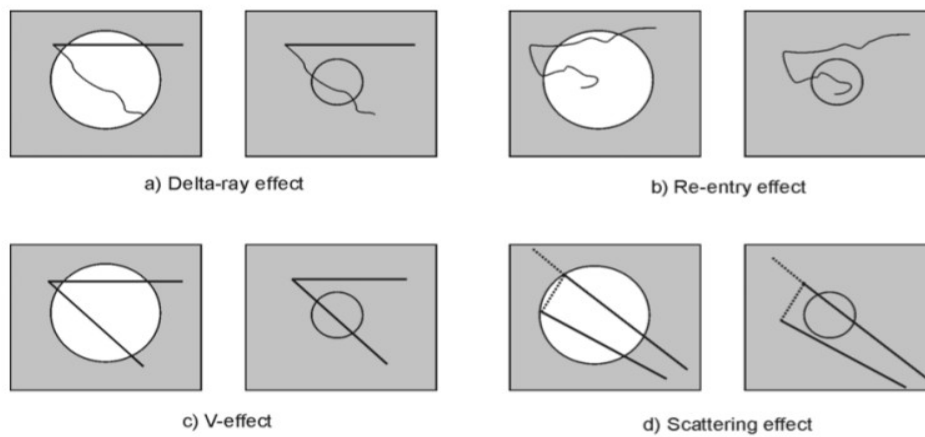
Pic. 3.1.3: *Schematic of four types of wall-effects. Straight lines represent heavy charged particle, dashed lines neutral primary particle while the twisting lines are for electrons. For every effect is shown what happen in the counter tissue-equivalent (left), and what in the real site (right). Picture is taken from [55]*

In pic. **3.1.4** is presented a comparison between experimental spectra taken with a wall TEPC (Takada 2001) and with a wall-less one (Tsuda 2010) [52] in a 290 Mev/u carbon ion beam. The shape of the peak is similar in the region of y around 10 keV μm^{-1} for both TEPC, which implies that the response functions of the wall TEPC are similar to that of the wall-less TEPC, in regard to the response to the primary beam. However, the counts with y of 0.2 to 3 keV μm^{-1} are much less in the wall TEPC than that with the wall-less TEPC. This demonstrates that the wall TEPC cannot measure the energy deposited by delta rays correctly because of the existence of the structural materials such as the thick cathode wall. More delta rays are produced in a solid cathode than in a gas, with the heavy ion beam irradiation of a general TEPC whose detection part is composed of a cathode wall made of a tissue-equivalent plastic. The wall used to define the sensitive volume of the TEPC influences energy deposition within the sensitive volume because it has a density significantly greater than that of the cavity gas. A systematic investigation of this effect has been made by Rademacher et al. [53] showing that it becomes important most of all for measurements in

high-velocity heavy ions beams. The response of a wall TEPC, for trajectories through the detector, is always larger than calculations for energy loss in a homogeneous medium. This enhancement is greatest for trajectories near the cavity/wall interface.
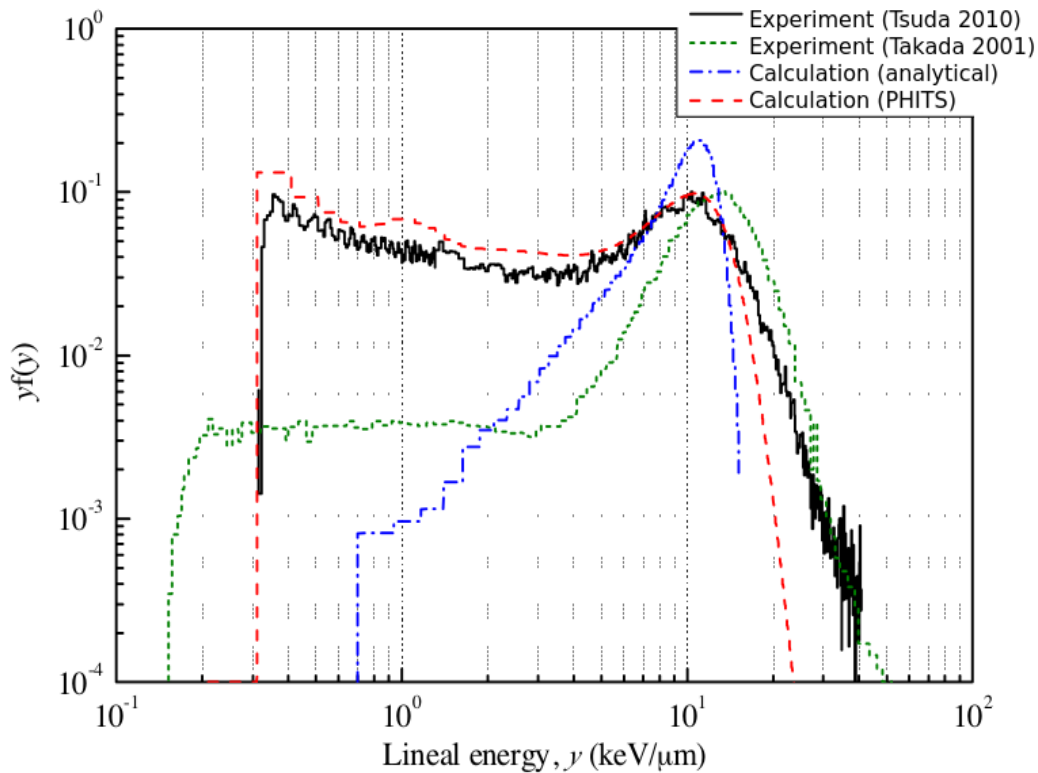

Pic. 3.1.4: *Graph taken from [52], analysing the behaviour of a wall-less TEPC. It shows frequency distributions of y of the wall-less TEPC, a commercial wall TEPC (Takada 2001) irradiated by the 290 MeV/u carbon ions and those of the calculations. The PHITS calculation is based on the microdosimetric model (Sato et al 2006). The contribution of delta rays is not included in the plot 'calculation (analytical)', because the calculation is based on the chord length distribution of the primary beam in a cylindrical detection volume of the wall-less TEPC.*

3.2 Mini-TEPC

For radiation protection applications, TEPCs with a cavity of a few centimetres are commonly employed, but for hadron-therapy applications, traditional TEPCs can not be used to collect microdosimetric data due to pile-up of the electronic signals in the high intensity of therapeutic beams. Another limitation of large size TEPC is the low spatial precision. It happens that with a diagnostic accuracy of the tumour of order of a millimetre, we are unable to monitor with equal precision, sometimes indispensable, the radiation field as the detectors have larger volumes than this limit. One way to avoid these drawbacks is to decrease the volume of the sensitive TEPC so that the number of particles intercepted remains low; by reducing the sensitive volume size, we also increase the spatial precision with which we measure the radiation field.

The first miniTEPC was manufactured at the Columbia University [3]. To simplify the construction, a cylindrical geometry, instead of spherical one, has been chosen: It has a cylindrical cavity of 0.5mm of diameter (see pic **3.2.1**). The main difference between a Rossi counter and the cylindrical miniTEPC is the geometry which imply a different chord length distribution: however the chord distribution for a right regular circular cylinder is not radically different from that of a sphere. The main advantage of using cylindrical cavity is that it simplify the construction, allowing the development of smaller TEPC.
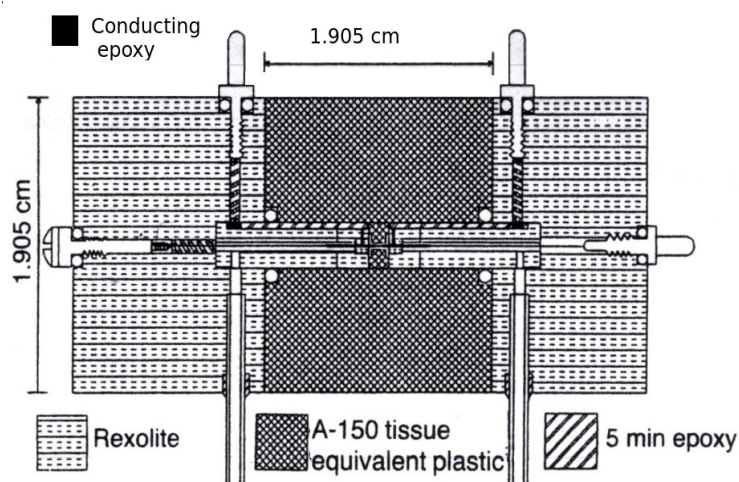
Pic. 3.2.1: Schematic of the miniTEPC of Columbia University [3].

The external dimension of this miniTEPC are still quite large, because it has guard tubes. Guard tubes (or field tubes) are electrodes that are maintained at a potential (respectively to the anode) equal to that which would have existed at the outer surface if they were not present and if the counter had been a infinite cylinder. These tubes allow to maintain the electric fields as constant as possible inside the sensitive volume, and then to delineate precisely the charge collecting volume. Guard tubes, however, have three major drawbacks:

1) they require a great mechanic precision in the phase of centring and insulating the tubes from the anode.

2) they have electrical connections and insulators that make the external dimensions of the TEPC encumbering.

3) they drive up the cost of the construction.

The need to miniaturize TEPC has led to study the possibility of building detectors without guard tubes that operate in a stable manner [54]. In pic. **3.2.2** is presented a design of a miniTEPC without guard tubes: the inner cylindrical cavity has a diameter of 0.9 mm and equal height, the external diameter of the cylinder is ~2.5 mm.
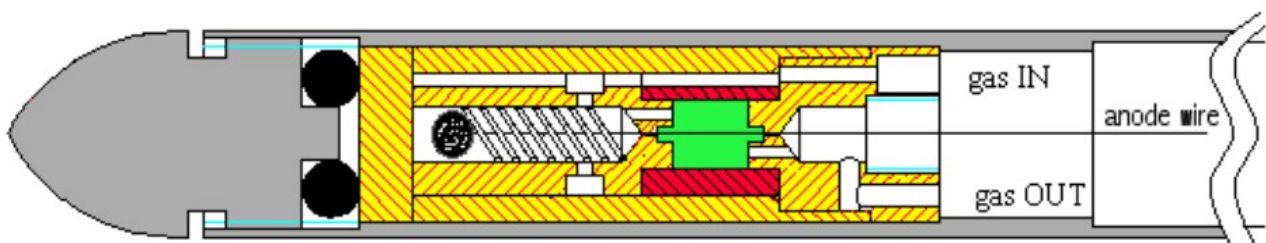
Pic. 3.2.2: Cylindrical miniTEPC without guard tubes. In green the sensitive volume, in red the TE-plastic A150 cathode.

The central anode wire of a mini TEPC has to be centred precisely to ensure an isotropic electric field. Assembling of a central wire in a small cavity is not an easy task. This become even more difficult for a mini multi-elemental counter. This situation motivated the development of alternative TEPCs that avoid these difficulties, such as the usage of micro-pattern and solid state detectors.

3.2.1 GEM-TEPC

To simplify the construction of a mini-TEPC, M. Farahmand first had the idea to develop a GEM based TEPC [55]. As can be seen in pic. **3.2.3** this TEPC consists of a cylindrical cavity, laterally defined by an insulator. One face of the cylinder consists of a cathode, made in equivalent plastic, the other face is defined by a GEM foil to amplify the electrons released in the cavity region, that are later collected on the anode.

GEM is a foil composed with an insulated layer covered both sides with copper, with an array of holes inside which the electric fields become strong enough to multiply electrons in avalanches when a suitable potential difference is applied to the copper layer (see chapter **4**).

The main difference with the traditional TEPC with central anode wire, is that the multiplication region is separated from the read-out electrodes, this allowed measurements with simulated site of nanometric order.
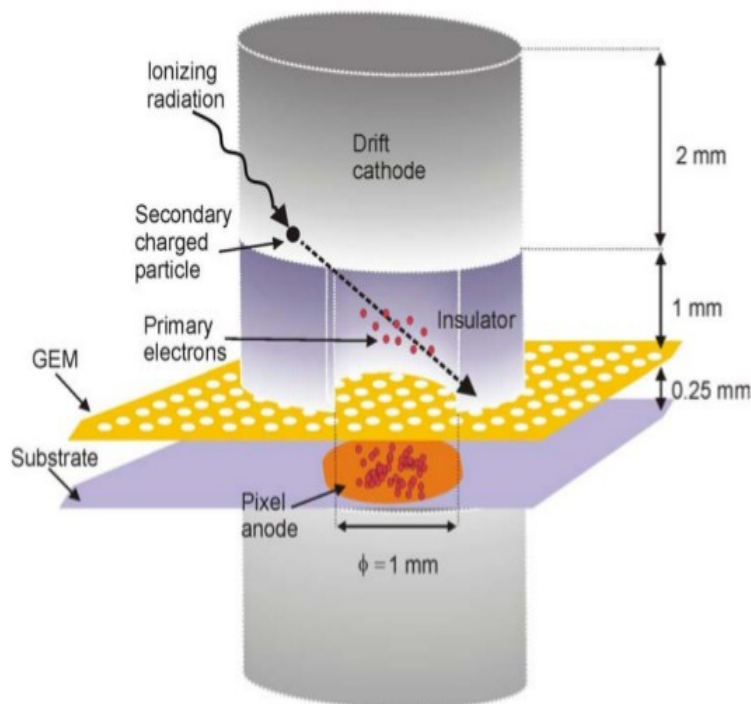
Pic.3.2.3: Schematic of a sensitive volume in the GEM based detector developed by M. Farahmand. Insulator walls, define the collective volume.

This detector has been used to obtain the microdosimetric spectrum with simulated tissue volumes

of 1 µm shown in pic. **3.2.4**. The spectrum was obtained using an encapsulated californium (^{252}Cf) source that produces a mixed ɣ/n field. The spectrum can be divided into three regions: first, the region up to a *y* value about 10 keV/µm due to the contribution of gamma rays to the spectrum; then, the region up to about 150 keV/µm produced by proton recoils in elastic scattering; finally, the region for *y* values larger than 150 keV/µm belonging to the contribution of α particles and heavy ion recoils.
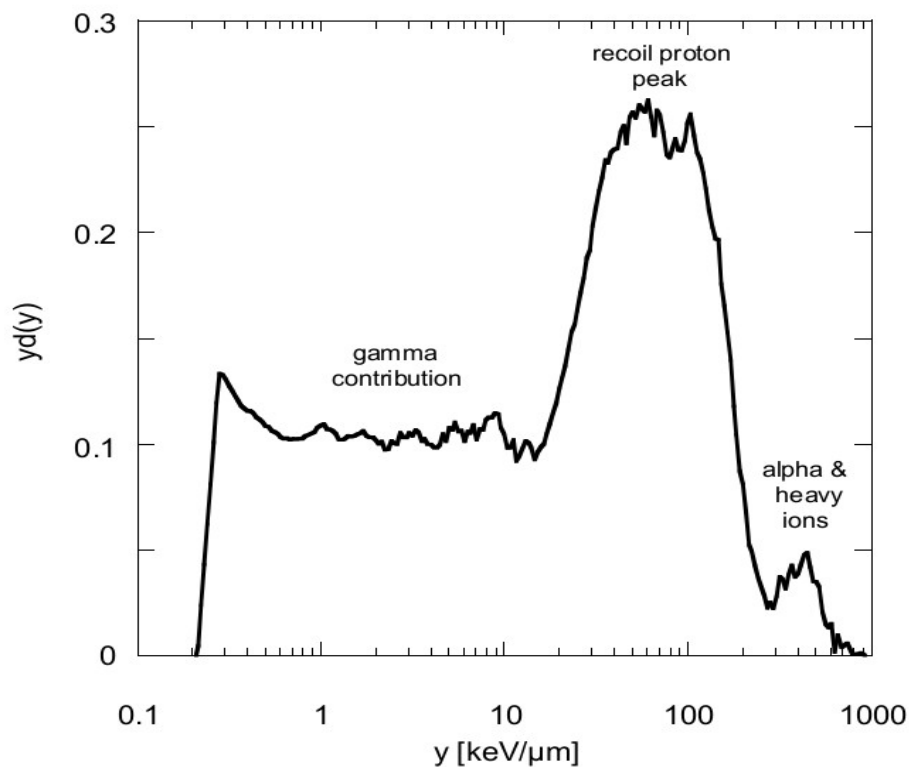
Pic. 3.2.4: Microdosimetric spectra for a 1 µm site size obtained by M. Farahmand [55] with encapsulated ^{252}Cf source measured with a cylindrical counter cavity of 1.8 mm in diameter and 1.8 mm in height. The gamma component, the proton peak, and the contribution of alpha and heavy ions to the total spectrum are indicated.

A similar work (Orchard 2011) applies the usage of a THGEM instead of a GEM, in a single detector for microdosimetry [56]. THGEM is a larger version of the GEM. It contains a thicker insulating layer and larger diameter holes. Compared with the GEM, the THGEM is easier to fabricate and cheaper, with similar performances. It was first introduced in 2002 by Periale et al. [57].
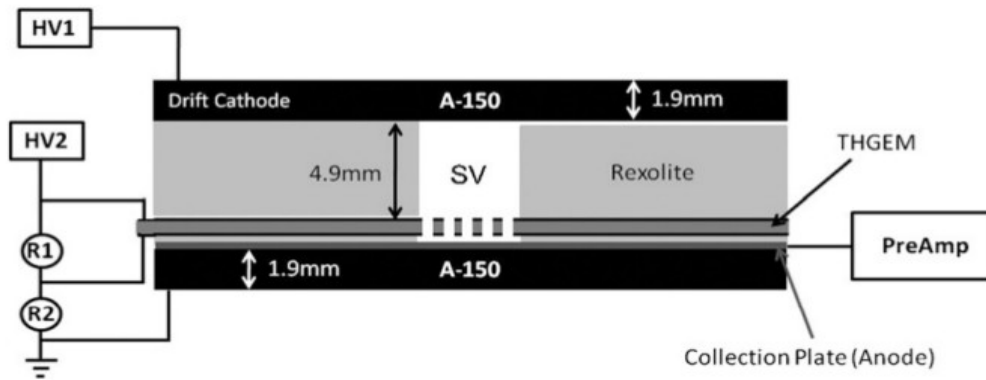
Pic. 3.2.5: Cross-section of the THGEM TEPC

Another TEPC detector based on GEM was developed by J. Debau [58], for radiation protection application. A multiTEPC has been developed to increase the sensitivity of a low-intensity radiation field. The detector consist of a single GEM, that define the multiplication region, and a stripped anode wire.
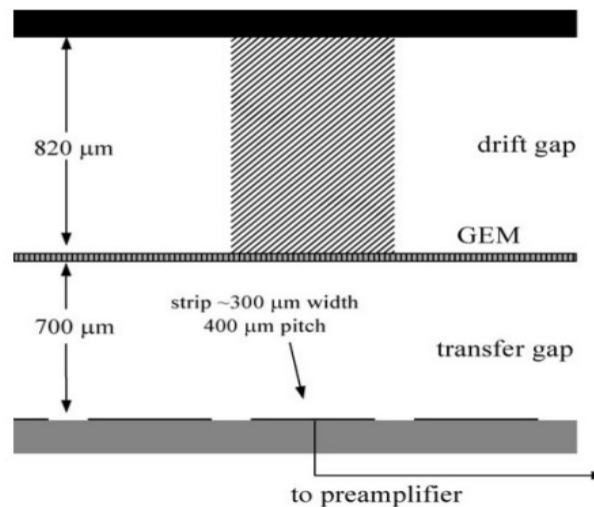

Pic. 3.2.6: Profile of the GEM configured for microdosimetry, developed by J. Debau.

It has wall-less collective volumes and a cathode in plastic TE that irradiates only from the upper layer in case of indirectly ionizing beams. The anode is divided into 128 collective stripes. Monte Carlo calculations showed that the probability for two distant strips to respond to a charged recoil particle emanating from the same primary neutron interaction in the TE–GEM was low provided the strips were separated by 1 mm or more. Thus, distances of this order in the detector appeared

42

to be relatively 'unconnected'. This condition allowed the design of the simplified readout coupling scheme of pic. **3.2.7**.

Although some events would inevitably lead to the generation of long-range secondary charged particles travelling parallel to the strip readout plane. The effect of such a particle track crossing two commonly coupled strips would be to yield falsely large imparted energy events, leading to an overestimate of the dose equivalent.
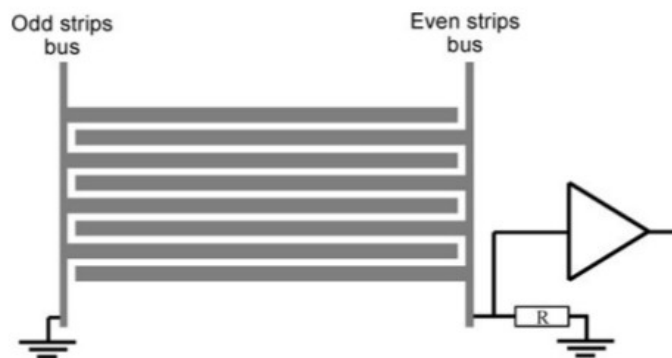
Pic. 3.2.7: *Schematic of the connection in the anode of the TEPC detector based on GEM developed by J. Debau [58].*

3.3 Solid state microdosimeters

The employment of solid state, allows the construction of detectors with micrometer dimensions. They are simple in construction, they don't require a flow gas system, and can operate with lower potentials than required for a miniTEPC. Besides they have the advantage of having condensed phase like the human tissues they are simulating.

An example of the **Silicon** detectors for microdosimetry developed at the University of

Milano is sketched in pic. **3.3.1** [59, 60, 61]. The monolithic telescopic structure consists of a thin diode (~2 µm) on the surface to measure ΔE and a thick substrate diode (~500 µm) to measure E. Micrometric cylindrical diodes (9 µm in diameter) are designed on the surface layer being the silicon microdosimeter. The ΔE/E structure of the detector makes it possible particle identification, e.g. protons against electrons, and particle energy assessment. This information allows event-by-event analysis for an optimized tissue equivalence correction.

Owing to the dimensions of its active volume, the segmented ΔE detector is in principle a microdosimeter, while the E detector can give information about the kind and the energy of the impinging particle. Pic. **3.3.2** shows a typical scatter plot ΔE/E obtained with this detector in the proton radiation field of CATANA facility.
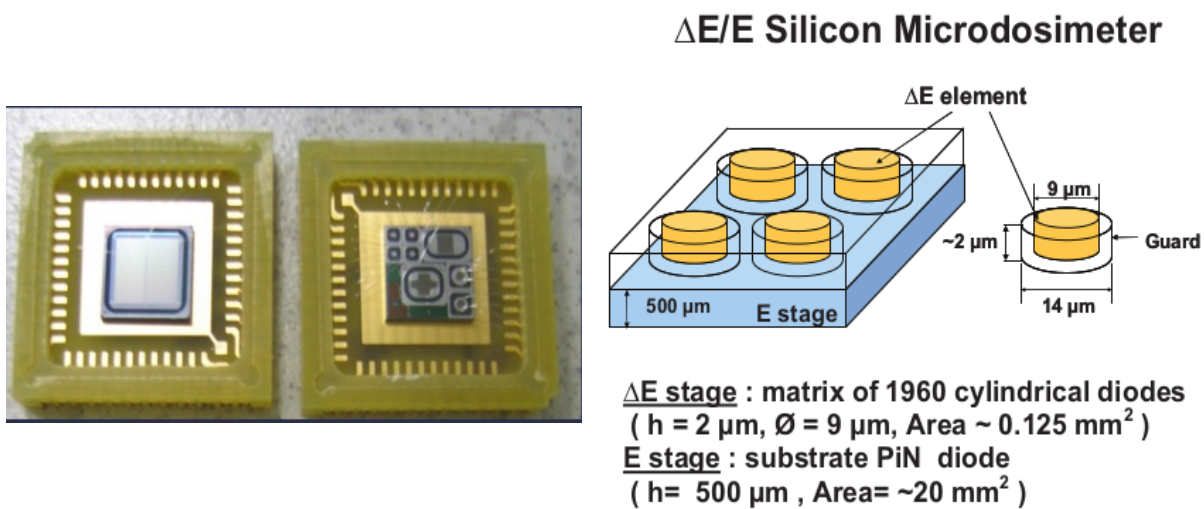
Pic. 3.3.1: Schematic and picture of silicon detector.
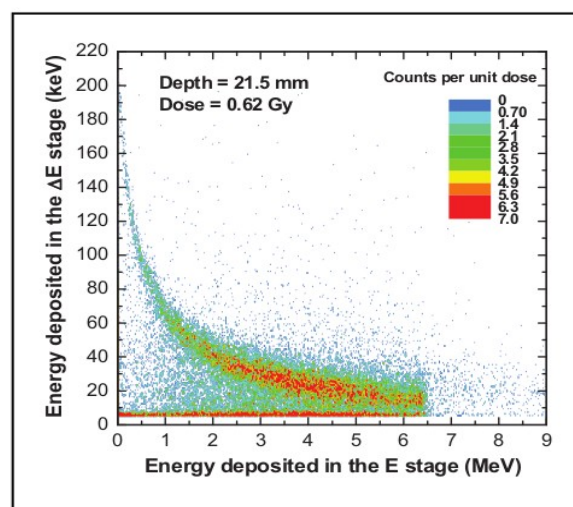
Pic. 3.3.2: Scatter plot of the energy deposited in the surface diode (ΔE stage) against the energy deposited in the substrate diode (E stage) for the same event [59].

44

In order to derive lineal energy spectra similar to those acquired by a reference cylindrical TEPC (the reference detector in experimental microdosimetry), the spectra of the energy imparted in the silicon ΔE detector are corrected for **tissue-equivalence**, obtaining distributions equivalent to those of a tissue ΔE detector by scaling the energy ε imparted per event in the silicon ΔE detector with the ratio R of stopping powers of the radiation measured in tissue and in silicon, and for **shape-equivalence**, in order to take into account the difference in shape between the sensitive volumes of a reference TEPC (1 μm simulated diameter) and of the silicon one.

In pic. **3.3.3** a microdosimetric spectrum obtained with the proton therapeutic beam of CATANA facility at 21.8 mm of depth is compared with one taken with a cylindrical TEPC in the same conditions. The agreement is satisfactory, but the electrical noise affects the lower threshold of the lineal energy (6 keV/μm), and this presently limits the application range of the silicon microdosimeter to the medium and high LET radiation fields. The reason of the relatively high electronic noise is the high specific capacitance of the thin surface diode, therefore only microdosimeters with very small area (and efficiency) and very low strays in the connections to the amplifying device could significantly improve the low-energy threshold.
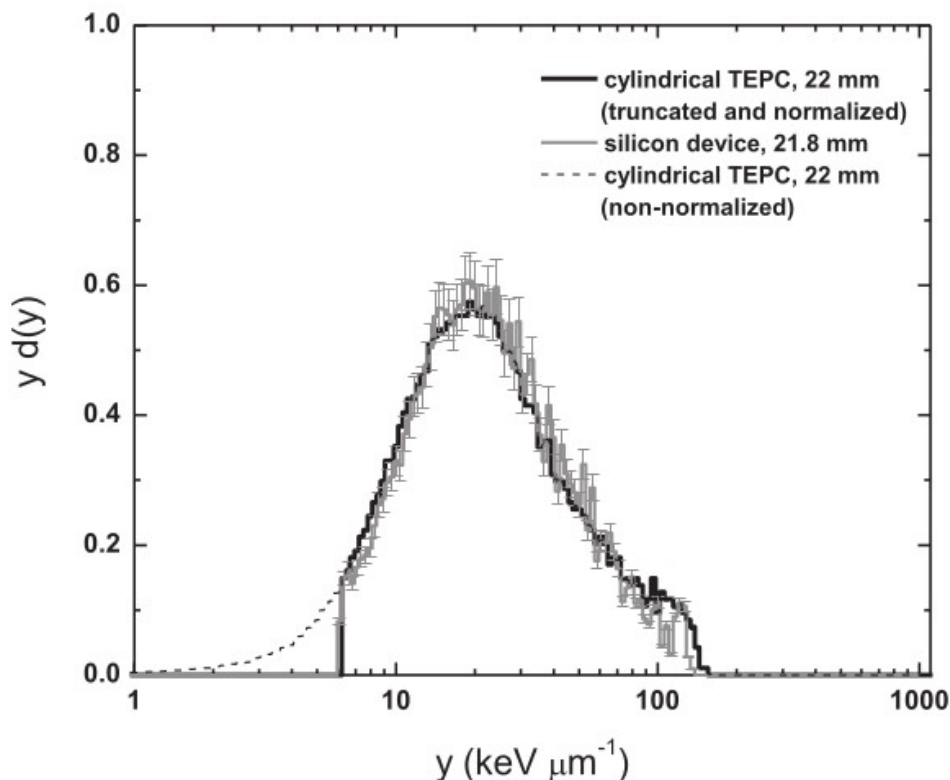
Pic. 3.3.3: Comparison between the lineal energy spectra obtained with the silicon device (grey curve) and those obtained with the reference TEPC (solid black curve) truncated at a value corresponding to the energy threshold of the silicon-based system (6keV/μm). The non-normalized complete microdosimetric spectra measured by the TEPC are also shown (dashed black line) [61].

Because of the strong radiation hardness, the large band gap and their closeness to tissue, diamond based dosimeters are widely investigated for medical and environmental applications.

Diamond detectors for microdosimetry are developed at the University of Roma: the aim is to develop a transportable microdosimetric detector that simulates easily size of 1-2-µm [62, 63]. A schematic of this kind of detector is drawn in pic. **3.3.4**.

The first diamond layer grown on top of a generic low cost monocrystalline High Pressure High Temperature (HPHT) diamond substrate, is about 15 µm thick and heavily doped by boron. This takes advantage of the conductive properties of boron which acts as backing buffer contact. A second layer of intrinsic high purity and high quality CVD diamond is then grown on top of the doped diamond. This is the detecting region, its thickness is variable from a few microns up to more than 400 µm depending upon the use of the detector.

The electrons and holes produced by the radiation in the upper region (i.e. sensitive volume) are collected by the electrode (Ag contact) since the boron doped layer do not allow the carriers to proceed toward the HTHP region.

This detector is characterized by high reproducibility of the layered detectors in term of performance and stability [63].
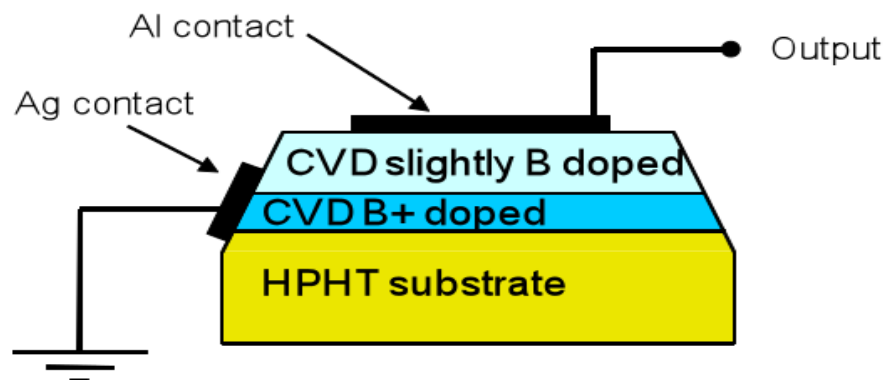
*Pic. 3.3.4: Schematic of the diamond detector [62].*

The diamond components have the ideal characteristics for a beam intensity monitor: they are composed of carbon, an element with a low atomic number, and therefore they do not interact highly with the beam, but still further studies are necessary to compare the results to a standard TEPC microdosimeter, to increase the signal to noise ratio, and to optimize the readout electronics.
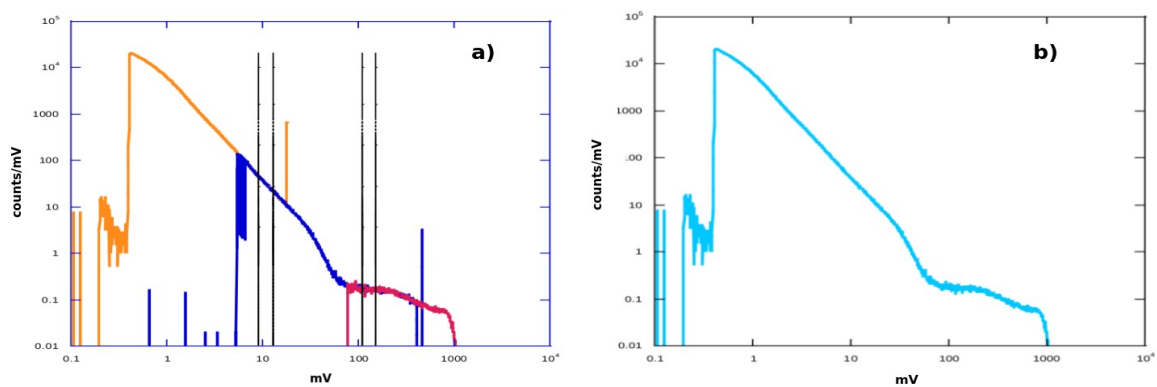
3.4 Generation of a microdosimetric spectrum

Because of a rather large range of values in most microdosimetric distributions (from 0.1 keV/µm to 1500 keV/µm), microdosimetric spectra are usually collected by using three different multi channel analyser. Pre-amplifier pulses are sent to three different linear amplifiers, which have different gains in order to reach the same resolution both for small-size y-events and large-size y-events, usually called low LET, medium LET and high LET. By means of a pulse generator, it is possible to test the linearity of acquisition system and to find the linear correlation between channel and mV; in this way the three original sub-spectra can be calibrated in Volt. In pic. **3.4.1-a** it is shown the three count-spectra, collected with three different amplifications. In pic. **3.4.1-b** the same spectra are collected in a single chart; they are calibrated in mV and represented on logarithmic axes, their overlapping regions can be easily seen. The first sub-spectrum (orange) is due to the output signals amplified with the highest gain factor (low LET), the second spectrum (blue) corresponds to counts arriving from the amplifier with middle gain factor (medium LET) and the red sub-spectrum belongs to amplifier with unitary amplification (high LET). In the overlapping regions sub-spectra show the same trend but different counts per channel. This is naturally due to different amplification and to different ADCs channel numbers.

In order to obtain a single total microdosimetric spectrum, the three different spectra are joined together in the overlapping parts by multiplying every spectrum for a determined factor (see pic. **3.4.2**). The peaks at the ends of the sub-spectra represent saturation effects in the counting system. In pic. **3.4.2-a** the joint regions are highlighted, pic. **3.4.2-b** shows the final result.

The pulse height spectra (pic. **3.4.2-b**) should be converted into the densities $f(y)$ (frequency distribution) and $d(y)$ (dose distribution) of the lineal energy y. The linear representation of $d(y)$ vs y or $f(y)$ vs y is rarely employed. Instead, the representation of fundamental microdosimetric spectra is traditionally displayed as a log-linear plot with the ordinate multiplied by y such that the area under the curve delimited by two values of y is proportional to the fraction of events (for $f(y)$) or to the fraction of dose (for $d(y)$) delivered by events in this range of lineal energy values.
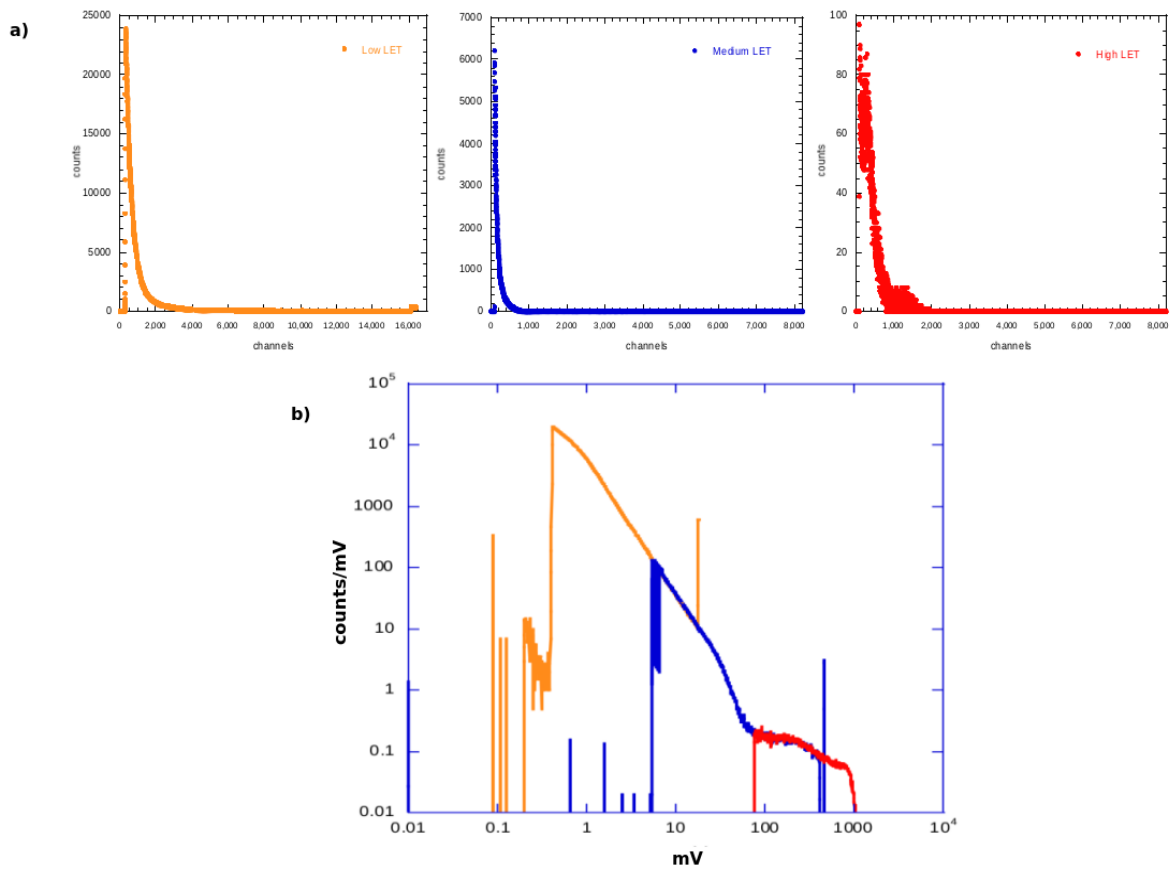
Pic. 3.4.1: *Counts obtained with three different amplifiers (a), plotted together on a logarithmic axis (b). [64]*

Pic. 3.4.2: *Evolution of a microdosimetric spectrum: on the left (**a**) the regions of overlap and junction are highlighted, on the right (**b**) is shown the total count-spectrum after the junction of the three spectra. [64]*

48

The graphical presentation of f(y) and d(y) requires a conversion of these distributions to a logarithmic scale of y, in order to have the same number of channels per y decade. Usually the number of channels is between 50 and 100; therefore, any channel in a microdosimetric spectrum has the same logarithmic size. Let the logarithmic scale of y be subdivided in B increments per decade, such that the *nth* value of y is: $y_n = y_0 \cdot 10^{n/B}$ where y_0 is the lowest value of y that has to be considered in graph [22]. One of the reasons showing spectra graphically is to be able to estimate from the plot the fraction of events that have lineal energy values in a given range of interest. In the log-linear representation, the ordinate must be multiplied by y because of the fact that:

$$\int_{y_1}^{y_2} d(y)\,dy = \int_{y_1}^{y_2} [y\,d(y)]\,d(\ln y) \qquad \int_{y_1}^{y_2} f(y)\,dy = \int_{y_1}^{y_2} [y f(y)]\,d(\ln y)$$

The principle of logarithmic re-binning of the linear spectrum is based on the following equation:

$$d(\ln y) = (\ln 10)(\log(y)) = \frac{1}{y}\,dy$$

consequently the normalization of frequency and density distributions are defined as:

$$\int f(y)\,dy = (\ln 10)\int y \cdot f(y)\,d(\log y) = 1 \qquad \int d(y)\,dy = (\ln 10)\int y \cdot d(y)\,d(\log y) = 1$$

The full spectrum obtained, showed in pic. **3.4.3**, has not yet been calibrated in lineal energy.

The calibration is generally performed using one of the following methods. One, usually carried out in commercial TEPCs, is calibration based on an internal alpha source, another is calibration based on features of the lineal energy spectrum.
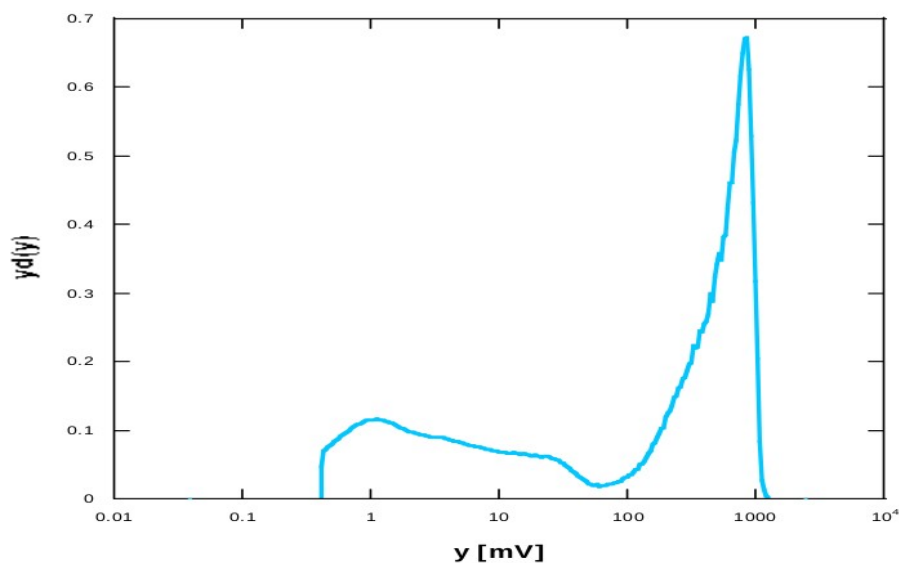
Pic. 3.4.3: *Typical representation of microdosimetric spectrum: yd(y) versus log(y). Microdosimetric spectrum of thermal neutron field at 1µm simulated site size, not calibrated [64].*

The first one associate the mean pulse height produced by particles crossing the detector along well defined trajectories with the mean lineal energy given by the formula:

$$y_\alpha = \frac{\Delta E_a}{l}$$

where ΔE_a is the absorbed energy in the TEPC sensible volume and l is the mean chord length. For a right cylinder or a sphere, in a uniform isotropic field of straight infinite lines, the mean chord length can be calculated with the Cauchy formula for convex body: 4V/S, and for both these

geometry it correspond to $\quad l = \frac{2}{3}d \quad$.

The second way to calibrate microdosimetric spectra is based on features of the lineal energy spectrum. This calibration is generally performed by analysing "edges" which correspond to maximum values of energy deposition in the counter by specific particles. These specific charged particles have a mean projected range that is equal to the maximum path length inside the simulated site. In mixed radiation fields, the calibration is most commonly performed using the proton edge: the maximum amount of energy that a proton can deposit in the simulated site size. The proton edge consists of a specific point in KeV/μm in the microdosimetric spectrum. As for alpha calibration, an empirical determination of this point serves to calibrate the entire lineal energy spectrum. However, this procedure assumes that the amount of energy required to produce an ion pair (W) is constant for all charged particles depositing the absorbed dose. This assumption is not strictly valid and therefore correction factors must be applied to account for differences in W-values between charged particles. The W-value correction factors have been adopted only for the secondary electrons produced by the gamma rays, for protons and for alpha particles. No corrections were evaluated for the heavy recoil ions. In literature there are some ways to find the proton edge: one of them, commonly chosen, is to find the mid-point of the final linear segment of the proton recoil portion of the lineal energy spectrum [65, 66].

Another possible "edge" usable, is the electron edge: using an external γ-ray source, an almost homogeneous and isotropic electron field is produced within the TEPC. Most electrons crossing its sensitive volume release only a small fraction of their kinetic energy. The maximum amount of energy is released by those electrons which cross the volume along its longest chord L_{max}, and stop exactly at the volume border, because of decreasing stopping power with increasing energy. In this case the electrons enter the volume with a range $R = L_{max}$, and lose their total kinetic energy inside.

Electrons of higher energy which cross and exit the volume have a lower stopping power (see pic. 3.4.4) and therefore release a smaller amount of energy. [67]
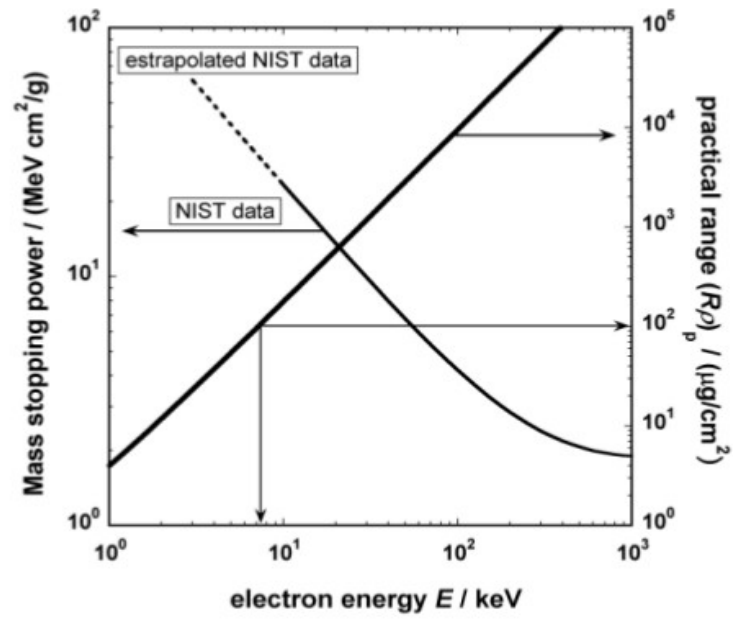
*Pic. 3.4.4: Mass stopping power and practical range.*

# 4. GEM detectors

4.1 Characteristic of a GEM foil

A GEM (Gas Electron Multiplier) is a micro-pattern detector consisting of a thick insulator foil, metallized both sides with copper in which an high density matrix of holes has been made (see pic. **4.1.1**).

With the application of suitable potentials, electrons released by ionisation in the upper gas layer (conversion and drift gap) drift into the open channels of the GEM (amplification region), where they multiply in an avalanche (see pic. **4.1.2**).
Due to its design, positive ions feed back into the drift region, and the underestimation of the charge due to local decrease of the electric field caused by positive ions is reduced as compared to that of a wire chamber.
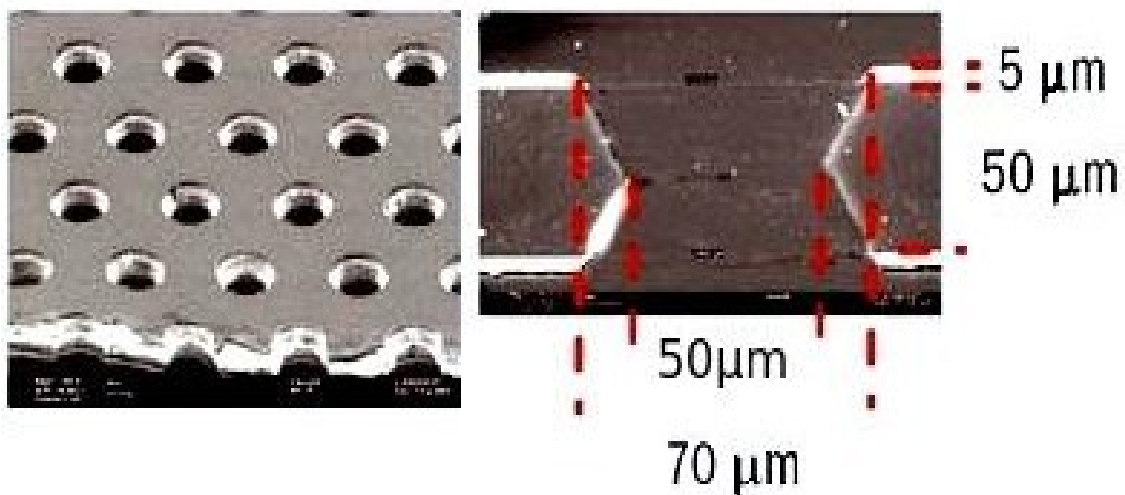
Pic. 4.1.1: Gas electron multiplier (GEM) detector: microscope photographs of a real device from above and the profile of the walls of the holes.
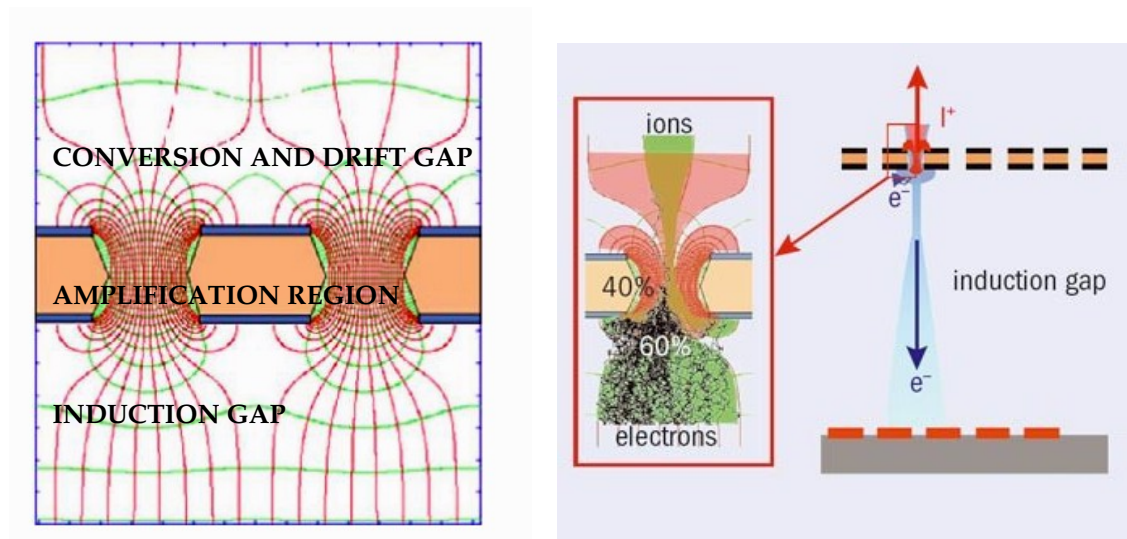
Pic. 4.1.2: Fields lines and amplification of a GEM [69].

The initial idea and the subsequent development and optimization of the geometrical parameters has been performed by Sauli in 1996 [68]. The choice of geometrical parameters of the GEM foil, such as the diameter, pitch, and the shape of the holes (conical, biconical, cylindrical) and the technology used are a compromise between construction needs and the proper functioning of the detector. Several types of GEM exist nowadays, with difference in dimensions, pitch and shape of the holes. Typically the insulator layer is made of Kapton, 50 μm thick, although GEM made with a different kind of insulator, such as polytetrafluoroethylene [70] are developed to improve the robustness of the GEM. Kapton has the advantage of being a commercial mass product and is widely used for the production of flexible circuit boards. However, it has the disadvantage that it easily carbonizes under the influence of the arc discharges during operations.

The apertures, of 50-100 μm in diameter, are typically spaced 100-200 μm, disposed in a triangular matrix and usually made using the photo-lithographic process, though it is possible to use a laser to drill the GEM [71].

The diameter of the hole affects the gain of the GEM. For the same external electric fields and polarization of the GEM, the reduction of the diameter of holes increases the electric field strength inside the hole, resulting in an increased gain of the detector. However, as shown in picture **4.1.3**, a saturation effect of the gain curve is observed for values of hole diameter below ~70μm [72]. This effect can be interpreted as an increasing in the number of electrons produced inside the holes that are captured from the lower electrode of the GEM, facing the induction region.

54
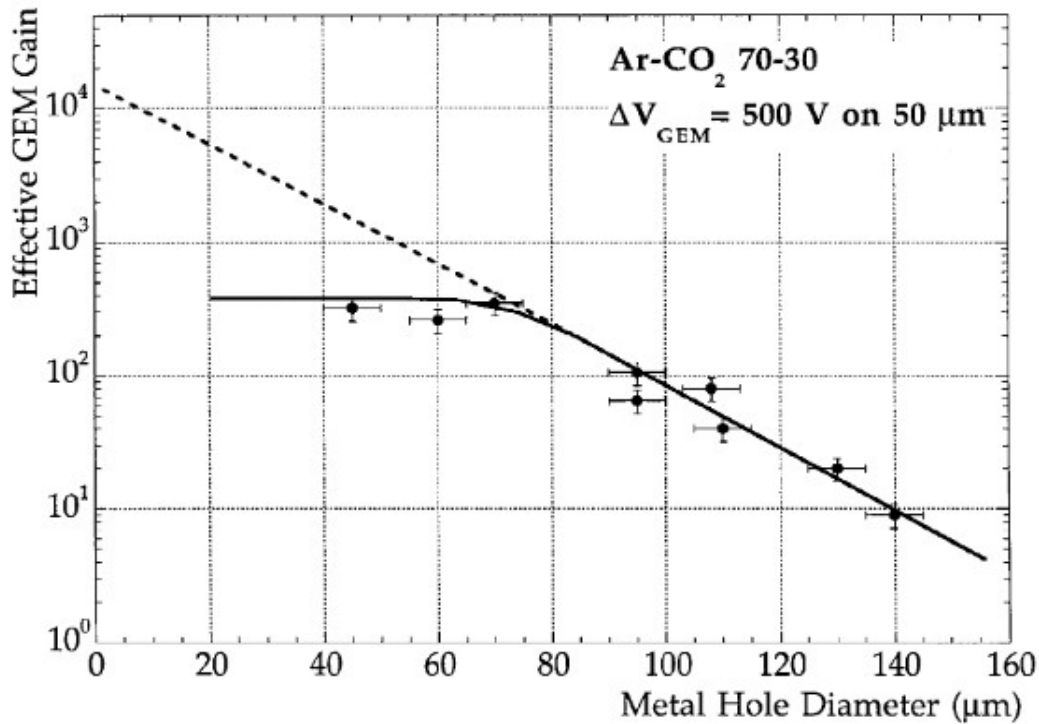
**Pic. 4.1.3:** *GEM effective gain in Ar/CO₂ for different metal hole diameter [72].*

The saturation effect, whilst limiting the possible gain enhancement, has the very positive effect of reducing substantially the dependence of gain from the precision of the GEM manufacturing process: the gain uniformity over the active area of the device is largely improved for hole diameters below the saturation value.

The pitch plays no role in the gain characteristics, but combined with the hole diameter affect the collection efficiency, or electrical transparency, for electrons released in the drift volume, as well as the distribution of ions produced in the avalanches. The optical transparency of the GEM mesh is ratio of open to total area. When the holes are disposed in a triangular matrix, it is given by the

expression $\quad \tau = \dfrac{\pi D^2}{2\sqrt{3}\,P^2}\quad$, assuming cylindrical holes of diameter D at distance P.

The geometry of the holes affects the charging-up, a short-term, rate-dependent instability of the electrode manifested usually as a small increase of gain due to the presence of insulating material close to the multiplication channels. Experimentally, it has been found [72] that the amount of increase depends on the geometry, reaching about 60% for the conical holes; lower than 20% for

the double conical ones and totally absent for a cylindrical geometry, as shown in pic. **4.1.4**.
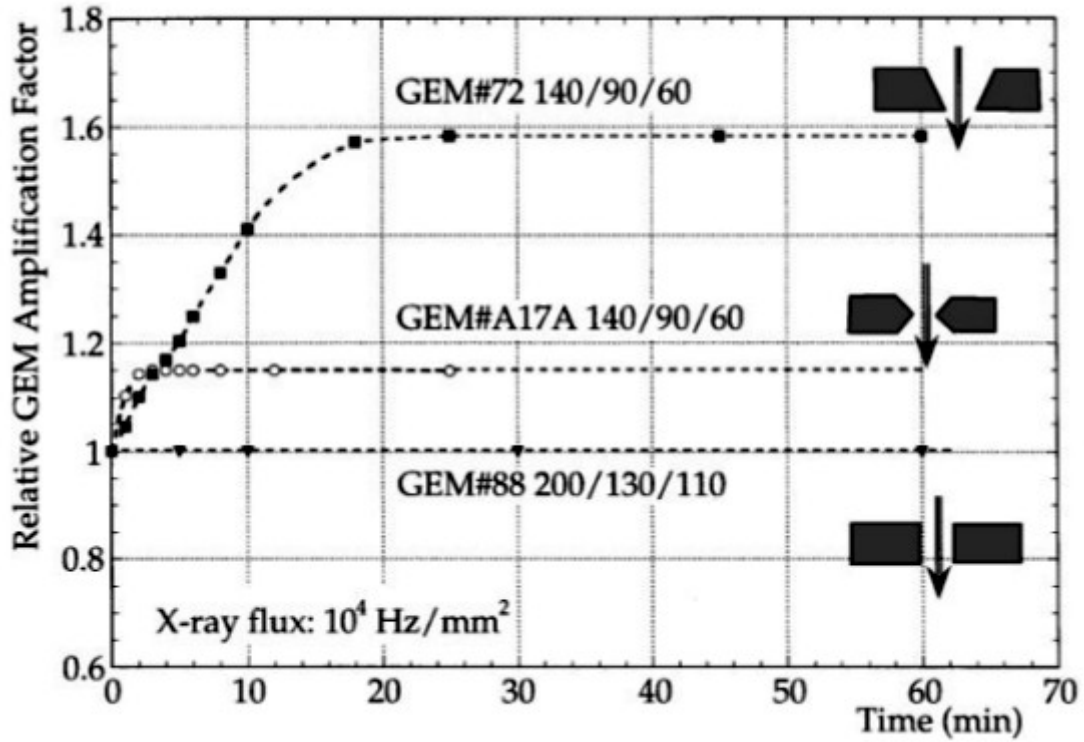
Pic. 4.1.4: *Time dependence of gain for several hole shapes under a particle rate of 104 Hz/mm² [72].*

4.2 Single GEM detector

Inserting a GEM between two plane and parallel electrodes, a single GEM detector is created. The upper electrode acts as cathode, while the lower one, consisting of a circuit (PCB) for the collection of the signal, acts as anode. In this way, two gap are defined, over and under the GEM (pic. **4.2.1**) named *drift gap* and *induction gap.* Placing a high voltage on the elements, typically

anode at ground, and negative potentials on the other electrodes, establish in these two regions uniform electric fields in the direction of the cathode, called consequently drift field, E_D, and induction field, E_I.

When an ionizing particle cross the drift region, electron-ion pairs are created. Following the force lines of the electric field, the ions migrate toward the cathode, while electrons are directed towards the holes in the GEM where, because of high field value, are multiplied in avalanches. The ions produced by the multiplication are partly collected on the top electrode of the GEM and in part will move towards the cathode, depending on the value of the drift field, and that inside the hole. By suitably adjusting the value of these fields, it is possible to liberate the area of multiplication in a very short time (of the order of 100 ns). Similarly, a fraction of the electrons produced in the hole are collected in bottom electrode of the GEM while most are transferred in the induction region contributing to the formation of the signal on the anode below.
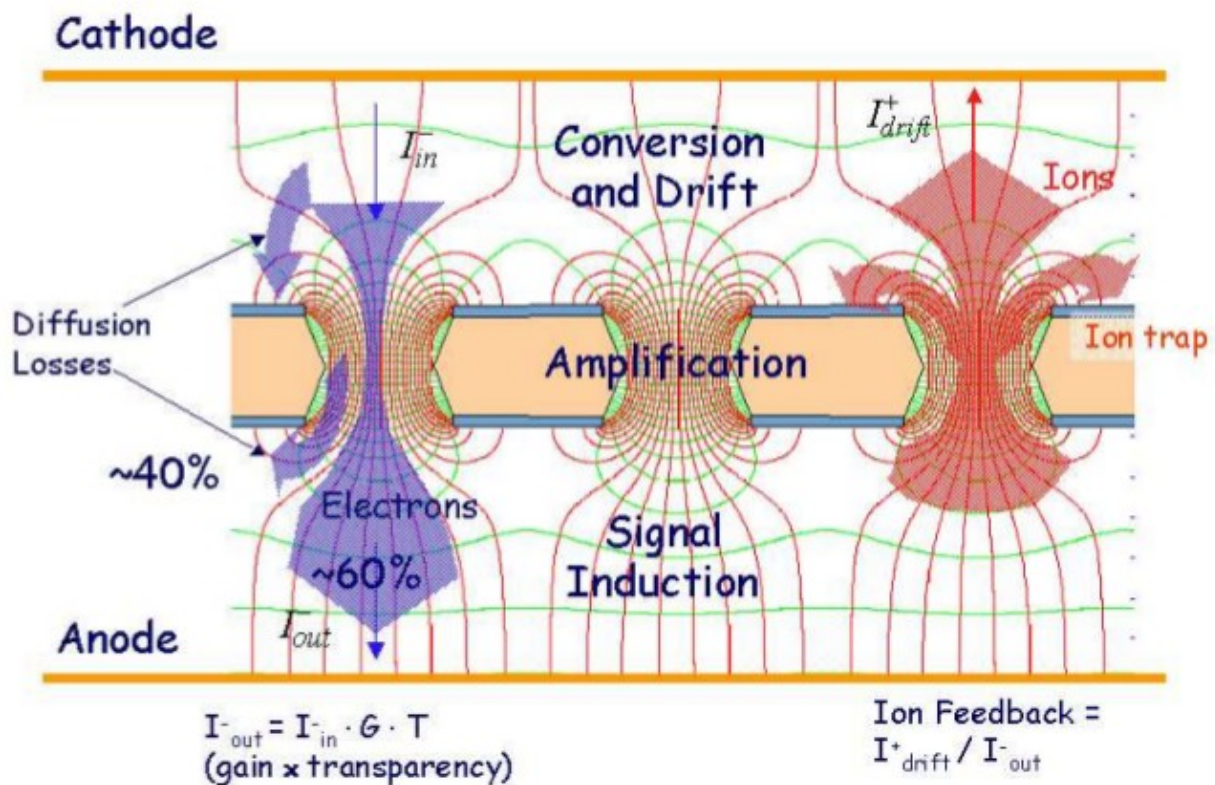
Pic. 4.2.1: Schematic of a single GEM detector and its fields [76].

One of the main differences with other gas detectors is that the signal induced on the PCB anode is purely electronic, i.e. it is due to the electrons motion in the induction region and therefore it is not

affected by the ballistic deficit typical of the detectors that collect also the ion signal.

Furthermore, thank to the GEM geometry, a single GEM detector has a unique advantage in that the multiplication region is separated from the readout electrodes, which are usually very vulnerable to damage from sparkling in the case of gas avalanches micro-pattern detectors.

Thanks to this geometry, the definition of the collecting volume can be made sectioning the anode in *strip* or *pad* (see par. **3.2** for examples) of the desired dimension and shape, without affecting the GEM multiplication [74].

Parameters that can be modified to adjust the detector operation, once the GEM foil geometry and the gas are chosen, are:

- electric drift-field and induction-field;

- potential difference between the GEM electrodes;

- drift- region and induction-region dimensions.

4.3 Signal formation in a GEM detector

The formation of the signal induced on the PCB of a GEM detector is due to the electrons motion in the induction region. If we consider that the signal starts to form as soon as the electrons leave the bottom GEM electrode, the induced current I_k on the pad k obtained using the Ramo theorem [80] is:

$$I_k = \frac{-q \cdot \vec{v}(x) \cdot \vec{E}_k(x)}{V}$$

where q is the charge, that is moving with a velocity v, and the $E_k(x)$ is the electric induction field due to the potential V_k placed in the k electrode (PCB anode).

We expect that every single electron coming out from the GEM hole, induce a current on the nearest pad, with a rectangular current pulse, and the width of the pulse depends on the time used by electrons to cross the induction-region:

$$I = \frac{-q}{t} = \frac{-q\, v_d}{x}$$

where x stands for the induction region dimension, and v_d is the drift velocity of the electron. Accordingly to this formula, to maximize the current we should use very little dimension for the induction-region, and high drift velocity.

4.4 Effect of the drift field

The drift-field has the function to transport electrons produced by the incident particle in the drift-region, to the GEM holes, where they multiply in avalanches. In pic. **4.4.1**, the signal induced in the PCB anode is shown as a function of the drift-field [74]. It shows a comparison of relative signal amplitudes for soft X-rays as a function of drift-field, deduced from a measurements of currents, and from pulse height with two shaping constants (100 ns and 1μs).

For values of drift field relatively low (<0.5kV/cm) there is a decrease in amplitude of the induced signal on the PCB: due to the low drift velocity, charges recombine before reaching the GEM. For field values intermediate (~0.5 ÷ 3kV/cm) the amplitude reaches a plateau and then decrease again for higher field values. The latter effect is due to the fact that a more consistent fraction of force lines of the drift field end on the upper electrode of the GEM rather than converge in the holes, i.e. the capacity of electrons threading into the holes of GEM is reduced (defocussing effect) [77].
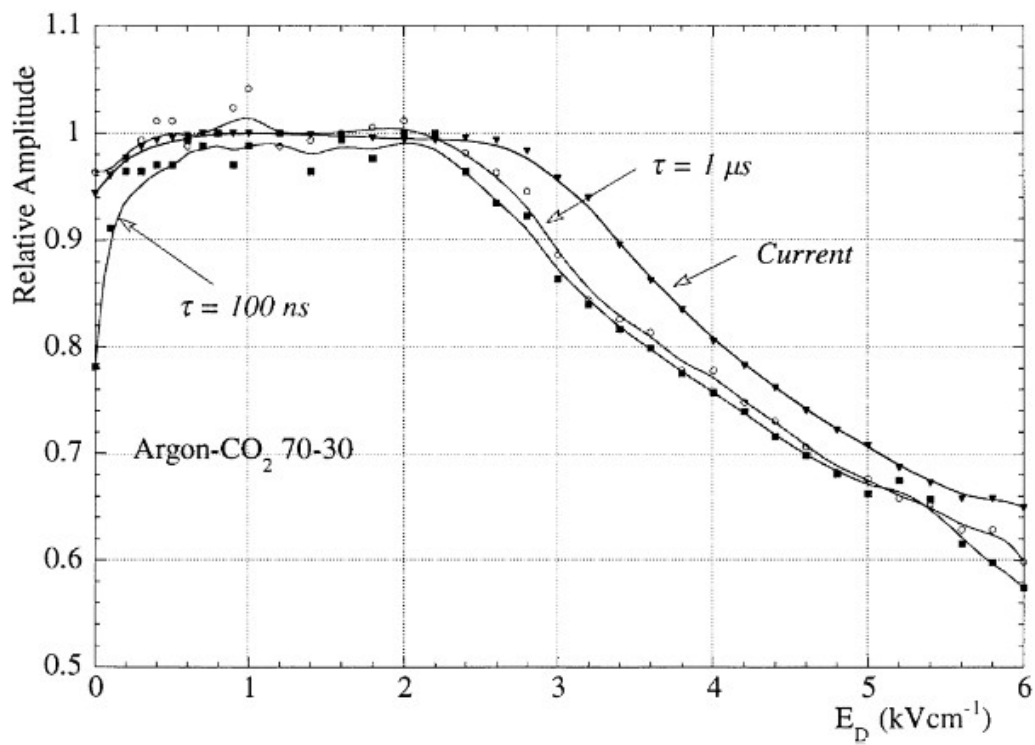
Pic. 4.4.1: *Collection efficiency as a function of drift-field [74].*
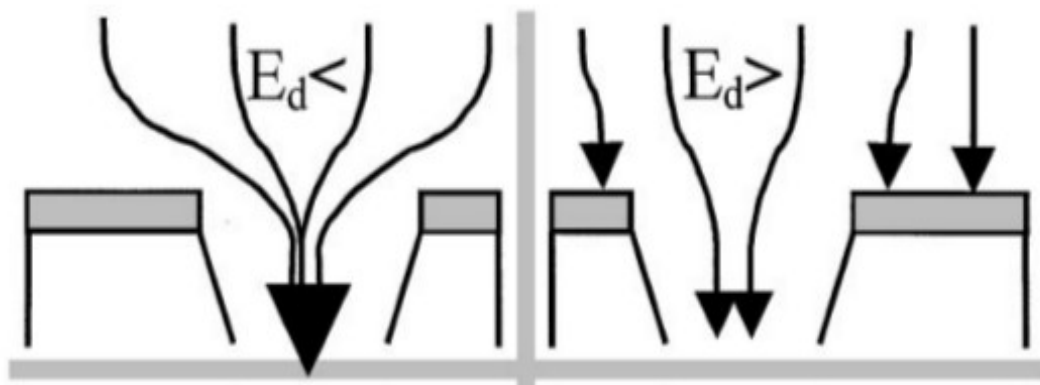
Pic. 4.4.2: *Schematic representation of the influence of drift field on electrical transparency. The arrows indicate electron cloud movement [75].*

4.5 Effect of the induction field

The induction field transport the multiplied electrons, from the GEM holes to the PCB anode. In pic. **4.5.1** the currents measured on the PCB (I_S), on the bottom (I_B) and top (I_T) electrode of the GEM, on the cathode (I_D), and the total (I_{TOT}) are shown as a function of the induction field [74].
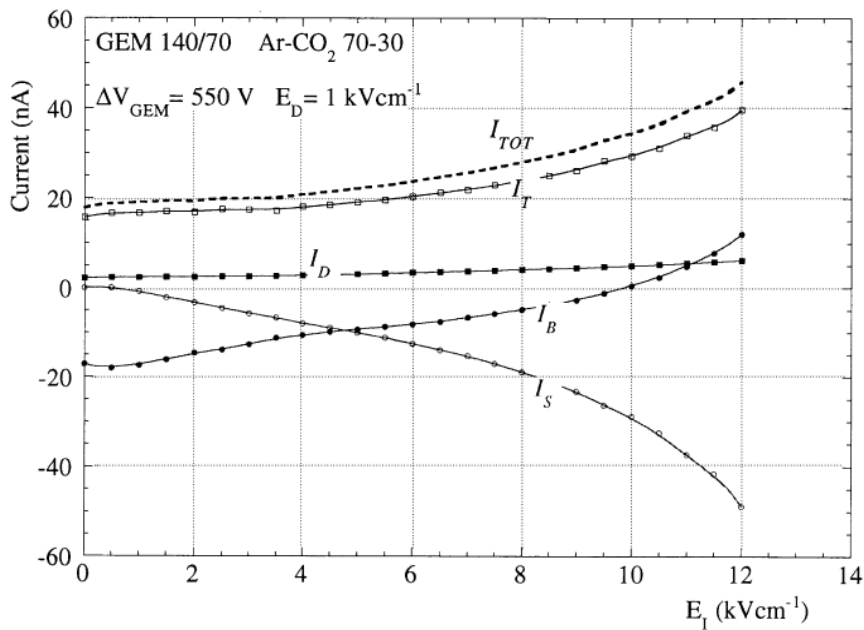
Pic. 4.5.1: *Current measured on the PCB (I_S), on the bottom (I_B) and top (I_T) electrode of the GEM, on the cathode (I_D) , and the total (I_{TOT}) as functions of the induction field E_i [72].*

An induction-field too low, do not allow the transfer of electrons to the PCB, in this case electrons are fully collected on the bottom electrode of the GEM (I_S =0 and I_B maximum). Increasing the induction-field, the current on the PCB increase, while decrease the current on the bottom electrode of the GEM. The limit for the induction field is due to the fact that fields too intense ($E_I \geq 8kV/cm$) may generate avalanches propagating in this region, with primers of unwanted discharges near the edges of the readout electrodes of the PCB, where the electric field is higher.

An intermediate value for the induction-field is about ~ 5 kV/cm, independently from the gas mixture used [73, 79].

4.6 Sizes of regions

The dimension of the drift-region is usually fixed about 2-4 mm, to obtain enough primary ionization and consequently an high intrinsic efficiency, with a negligible pile-up under high density particles flow [74]. The dimension for the induction-region is usually set around 1 mm, to contain electronic diffusion, and to keep the signal current as high as possible (see par. **4.3**). Accordingly to the formula in par. **4.3**, to maximize the current collected on the PCB we should use very little dimension for the induction-region, and high drift velocity.

Moreover, when a particle crosses the detector, it will ionize both inside the drift gap and induction gap. The signal created by the ionization electrons released in the induction gap has to be consider as a noise, since this signal it's not amplified by the GEM. Considering a ionization track with uniform density, if a charge Q is released inside the drift gap, a charge Q/n should be released inside the induction gap, where $n = x_D / x_I$ is the ratio between the dimension of the drift and induction regions.
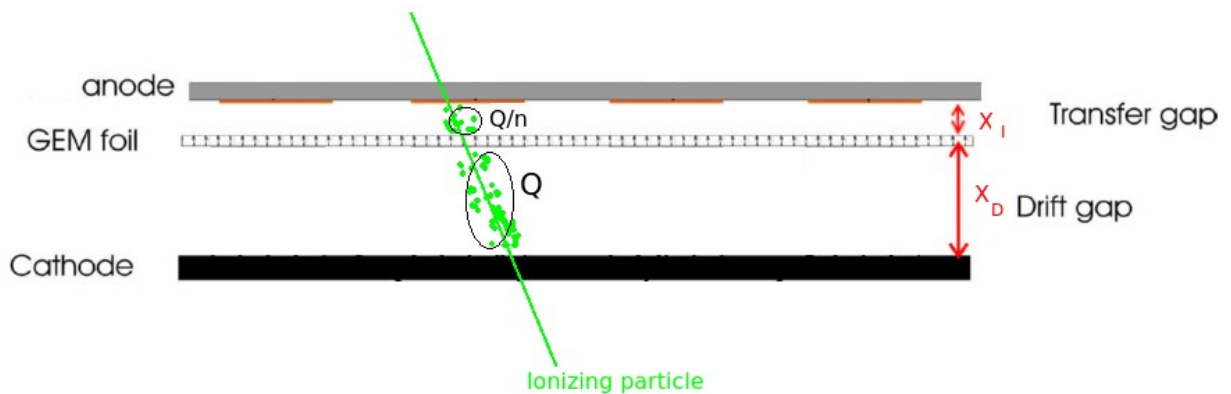
Pic. 4.6.1: *Ionisation induced on both drift and induction (transfer) regions by a ionizing particle crossing the detector.*

For these reasons the induction region should be keep as little as possible. On the other hand too small are not recommended as they would require high mechanical tolerances in order to avoid the occurrence of discharges on the PCB.

4.7 GEM polarization

The potential difference across the GEM has to be high enough to create an electric field capable of induce electrons multiplication in avalanches.

In literature has been reported that the GEM gain increases exponentially with the voltage applied between GEM electrodes (see pic. **4.7.1**).
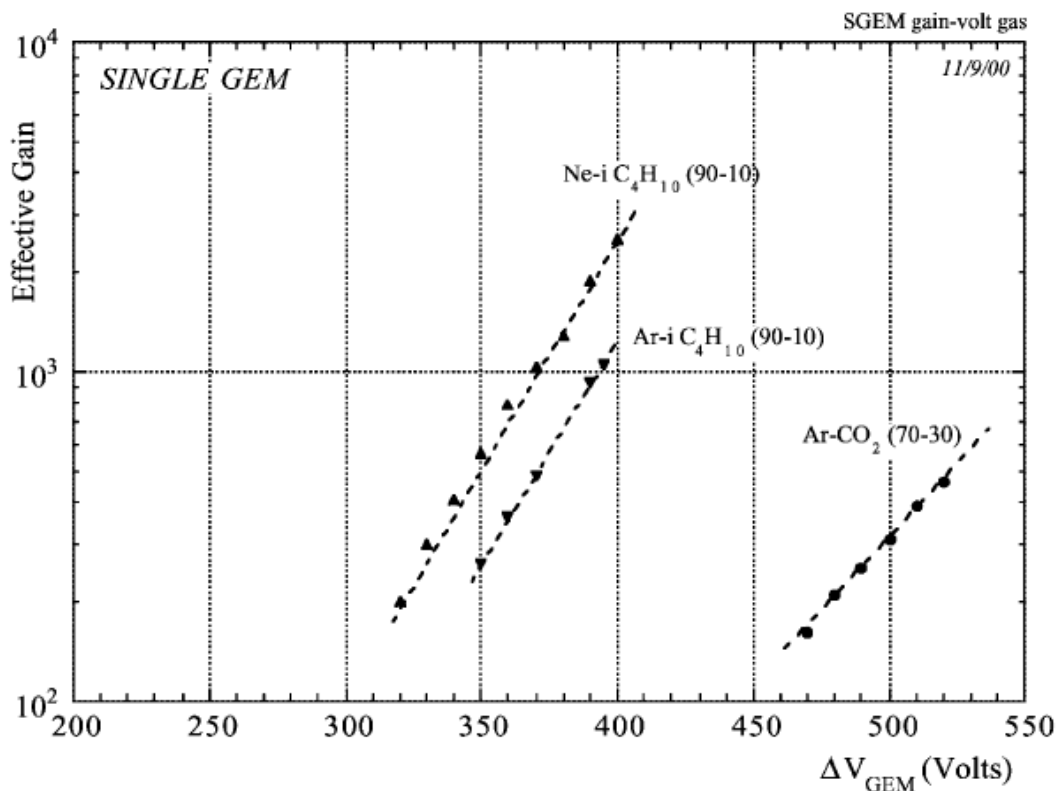
Pic. 4.7.1: *Effective gain of a single GEM detector in various gas mixtures* [73].

We can define two different type of GEM gain:

- The effective gain: the amount of electronic charge collected on the read-out electrode divided by the primary charge. Depending on operating conditions, the total amount of charge flowing through the detector can be larger than the fraction being collected by the electrode.

- The total gain: the absolute amount of electrons produced inside the GEM holes.

All measurements of gain in this paper refer to the effective gain.

The effective gas gain depends most of all from the voltage applied to the GEM, but different factors as electron collection efficiency and the charge sharing can affect it.

When leaving the GEM hole, not all electrons in the avalanche are collected on the anode; a field-dependent fraction of the electron cloud is trapped at the bottom GEM electrode due to dispersing effects or drift-field line-termination on the bottom GEM electrode, resulting in a loss of electrons. This is the effect which is referred to as charge-sharing.

5. TEPC-GEM based detector

In this chapter I will describe the motivations that have leaded to the design and construction of a new type of multi-TEPC based on a single GEM foil of the so called standard geometry that is characterized by biconical holes of 70 μm diameter and 140 μm pitch (140/70 GEM).

5.1 Choice of gas type, pressure and geometrical size

The counting gases commonly used in microdosimetry are methane-based or propane-based [22] tissue-equivalent (TE) gases at low pressure, to simulate a microscopic tissue site. The operation of GEM in these gas mixtures has been investigated by M. Farahmand [55].

M. Farahmand performed several measurements in both gas mixtures using two GEM types produced at the CERN printed circuit workshop: in one GEM the holes have an outer diameter at the surface of 80 μm, an inner diameter of 60 μm at the centre of the foil and a pitch distance of 140 μm (140/80 GEM), in the other GEM these values are respectively 60, 50 and 90 μm (90/60GEM). Both these GEM consist of a 50 μm thick kapton foil metallized with 5 μm copper on both sides, with an hexagonal matrix of biconical holes. Farahmand gas gain measurements are reproduced in pic. **5.1.1** and **5.1.2** respectively for methane-based or propane-based tissue-equivalent (TE) gases. It can be observed that the maximum safe gain is higher in C_3H_8-TE gas rather than in CH_4-TE gas and that this maximum occur for a gas pressure of 0.2-0.3 atm, depending on the GEM geometries.

Pure propane gas is also employed in microdosimetry, especially for space application [51, 81] and the equivalence of microdosimetric spectra measured in C_3H_8-TE and pure C_3H_8 has been proved [82].
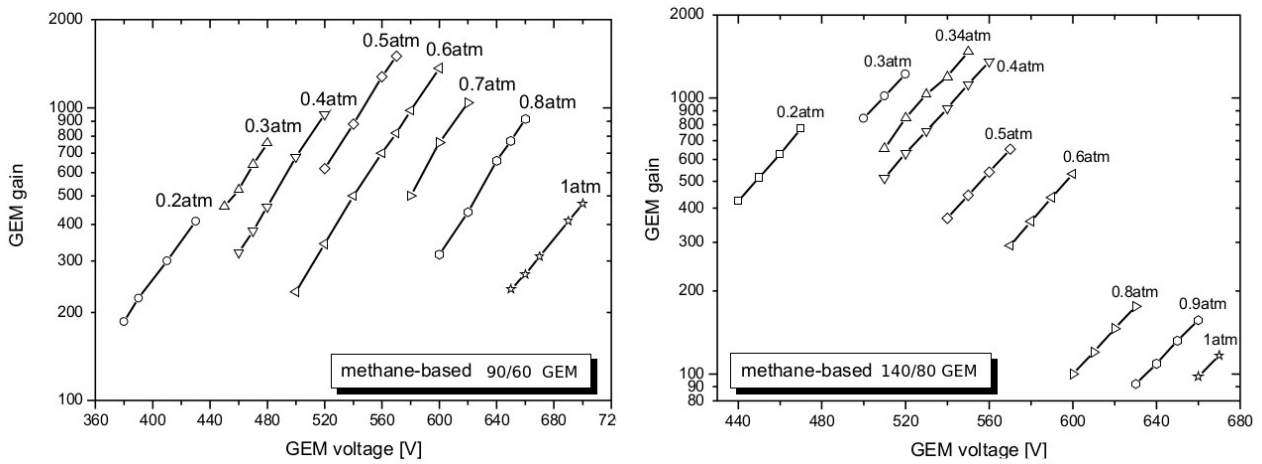
Pic. 5.1.1: *M. Faramhand measurements [55] of the GEM gain with two different GEM in methane-based TE gas.*
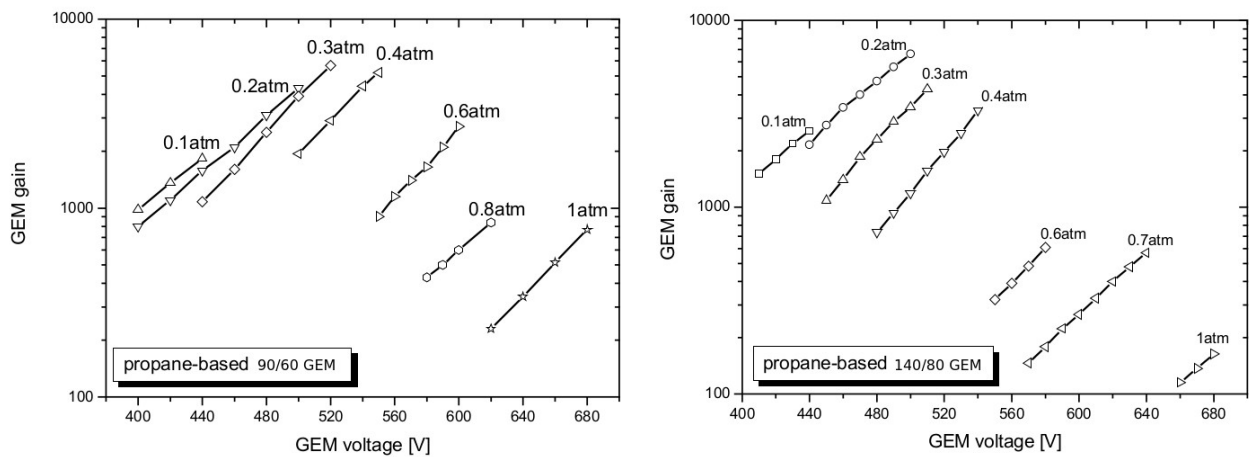
Pic. 5.1.2: *M. Faramhand measurements [55] of the GEM gain with two different GEM in propane-based TE gas.*

With respect to C_3H_8-TE, pure C_3H_8 has an higher gain [46, 82] and for this reason we have chosen to employ this gas in our counter. However, the properties of GEM in low pressure propane are currently undocumented. On the base of the results obtained by Farahmand we expect that even in C_3H_8 gas and with a 140/70 GEM foil the maximum safe gain will occur at a pressure between 0.2-0.3 atm. As our aim is that to simulate a sensitive volume of 1 μm equivalent size, we have fixed the dimension of the sensitive volume to 2 mm and the gas pressure to 280 mbar.

5.1.1 Walled vs wall-less

In order to simulate tissue cavities with size of 1 micron, the individual microdosimetric detectors will consist of straight cylinders 2 mm height and equal diameter, delimited on one side by a drift tissue equivalent (plastic A-150) electrode and on the other from the floor of the GEM. The events of ionization generated in each of the sensitive volumes, will be multiplied by the GEM to obtain measurable signals. The charge amplified, after having spread in a stage of "induction" will then be collected on the pads realized on a readout printed circuit board (PCB).

In order to decide advantages and disadvantages related to the realization of walled or partially wall-less detector, several aspects have been considered.

The construction of the detector is simpler for a wall-less detector and the deformation of the microdosimetric spectra due to "wall-effects" [83], especially relevant for charged particles of high energy [52], will be reduced. Nevertheless, to obtain a well defined sensitive volume for each microdosimeter with a wall-less detector is necessary that the electrons produced in the drift gap move toward the plane of the GEM undergoing a low transfer dispersion.
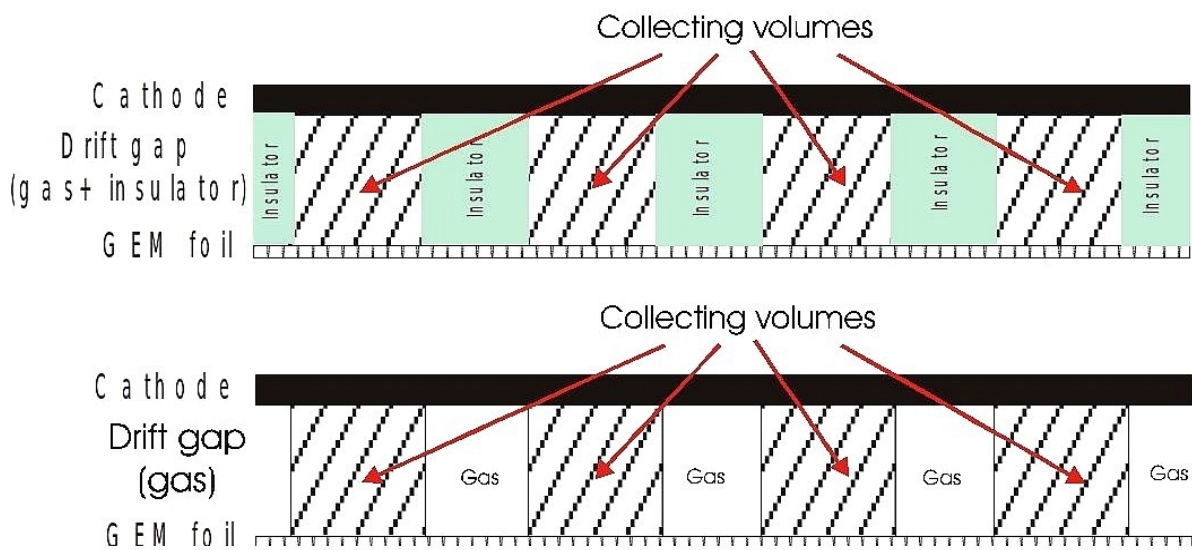
Pic. 5.1.3: *Wall vs wall-less schematic of the drift gap.*

In order to verify that these conditions are met, L. de Nardo made the calculations of the electrical potential in the detector (using a commercial program, FlexPD) and Monte Carlo simulations of electron transport in the gas. The model used in order to perform a 3D simulation of the detector, is outlined in pic. 5**.1.4**.
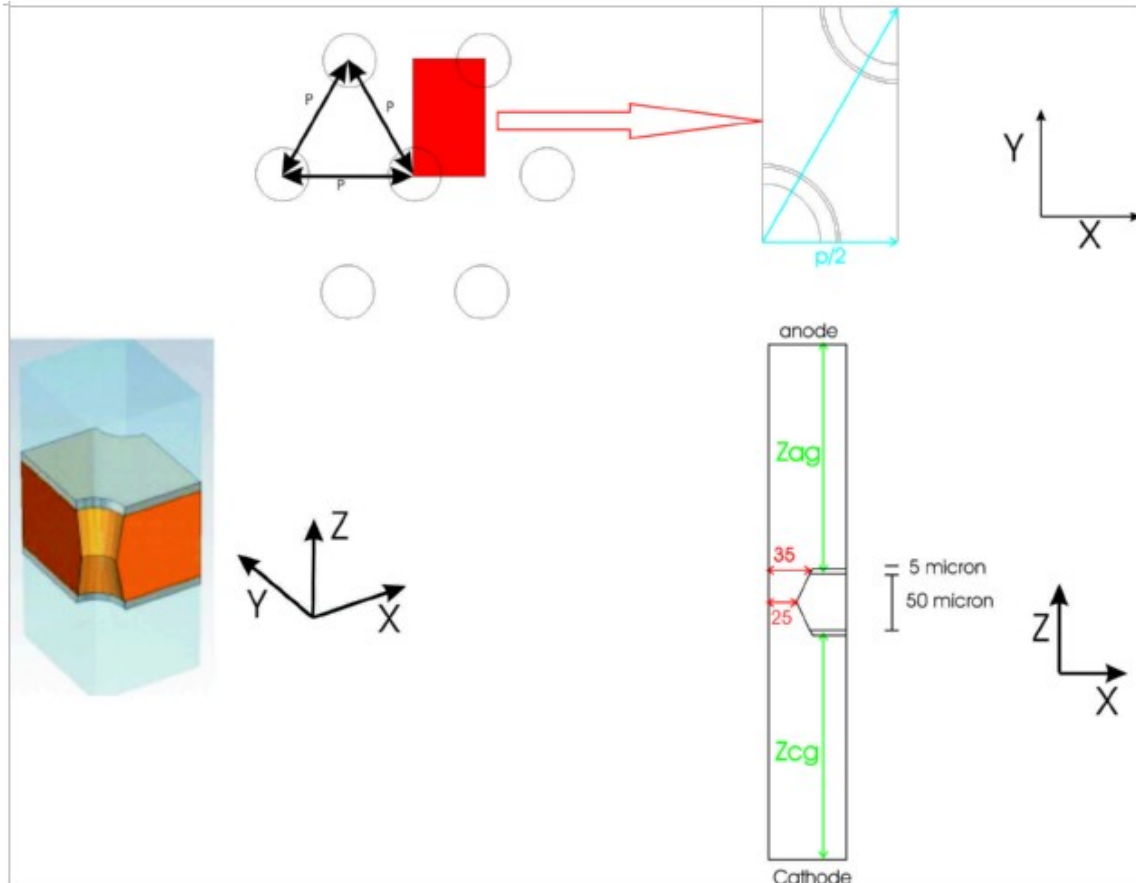
Pic. 5.1.4: *Model of GEM used to perform a 3D simulation of the detector.*

The area identified on the floor of the GEM and highlighted in red allows, for symmetry, the simulation of the triangular matrix of the holes of the GEM. The calculations made with field drift equal to $E_d = 60$ Vmm^{-1}, induction field $E_i = 400$ Vmm^{-1} and different values of ΔV_{GEM} show that, although at the centre of a single hole of the GEM, the electric field reaches very high values, the electric field in the drift region becomes practically uniform at a distance of 0.1 mm from the lower surface of the GEM (see pic. **5.1.5**).

This allows to perform Monte Carlo simulations of electron transport in the gas considering the electric field ad constant in the drift region.

Calculations performed with C_3H_8 gas at 280 mbar have shown that the collection efficiency of electrons created within the wall-less sensitive volume is in the order of 92±2%% and decreases rapidly to zero in the vicinity the edge of the sensitive volume. These results were found to be quite independent on the values of the drift field (in the range 50-1000 V/cm).

For comparison, the collection efficiency of electrons created within an equal volume, but bounded by walls, is of the order of 88%.
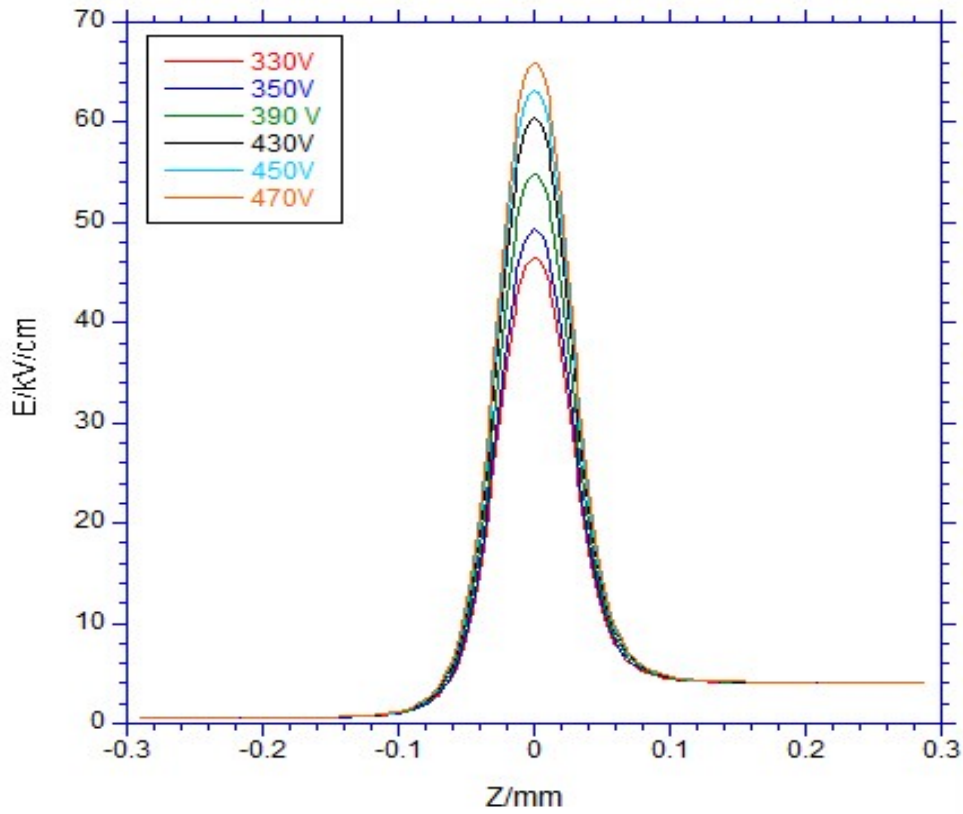
Pic. 5.1.5: Electric field along the axis of the GEM hole as a function of the distance from the centre of the GEM for different values of the voltage applied to the GEM.
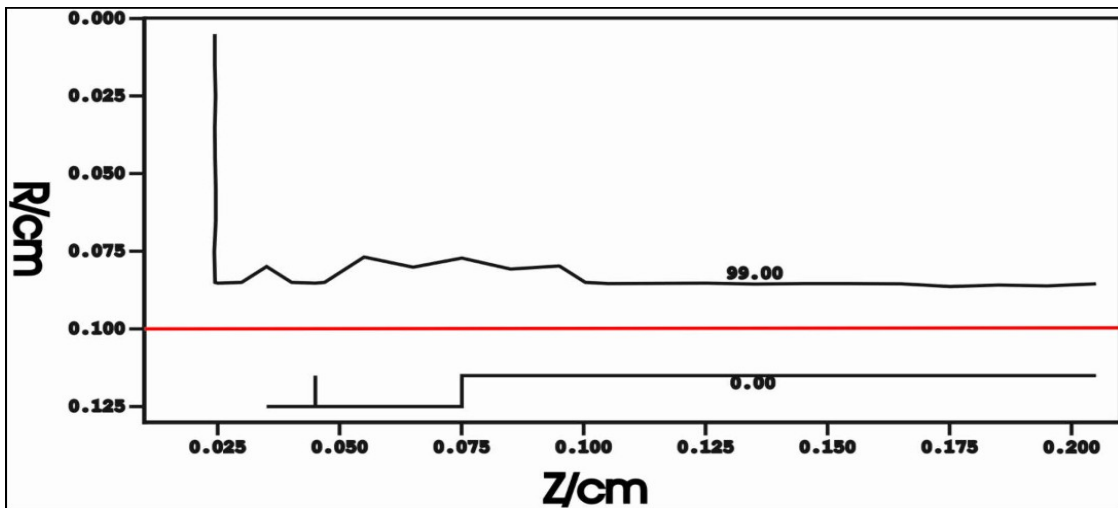
Pic. 5.1.6: Collection efficiency map, Z is the distance from the cathode, and R the distance from the central axis of the sensitive cylinder.
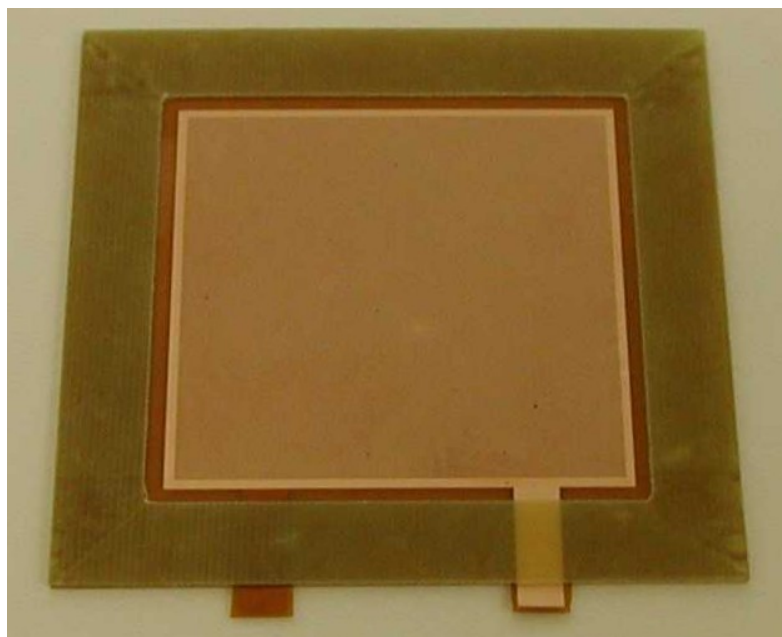
5.2 GEM-TEPC elements

The TEPC-GEM elements are a cathode, a GEM foil and a readout printed circuit board (PCB).
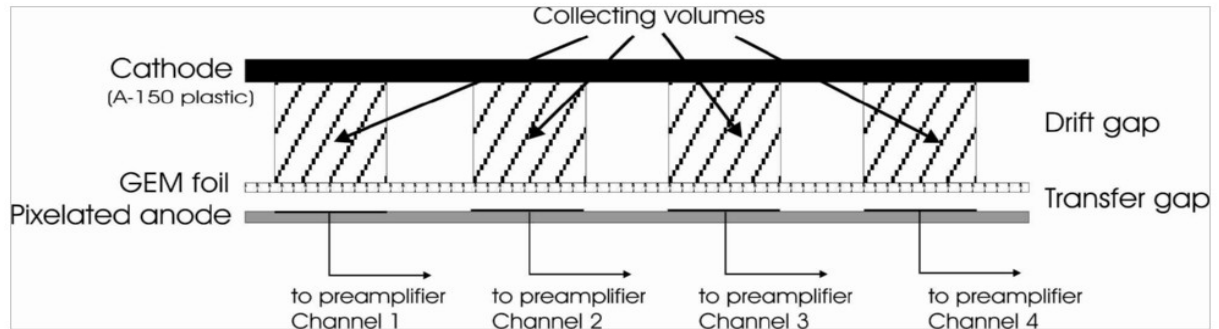
Pic. 5.2.1: Schematic of the detector.

5.2.1 GEM foil

We used a single GEM foil with an active area of 5x5 cm^2.

The GEM foil was assembled and developed at CERN. Compared to GEM foils produced by other manufacturers, with bi-conical holes with the same pitch but different inner and outer diameters, the CERN foils are reported to produce the lowest gain, but to exhibit the best gain stability over time [84]. The GEM structure used in this work is the so-called standard GEM, that is a kapton foil of 50 μm thickness, with a 5 μm thick copper coating on each side, perforated on a triangular pattern with a high density of holes with a double conical shape. The diameter in the copper surfaces is 70 μm, the diameter in the kapton is 50 μm. The holes have a distance between the centers of 140 μm. The GEM foil is glued between two fiberglass frames, each one of 0.5 mm thickness.

5.2.2 PCB

The signal created by the electron avalanche is collected on the anode.
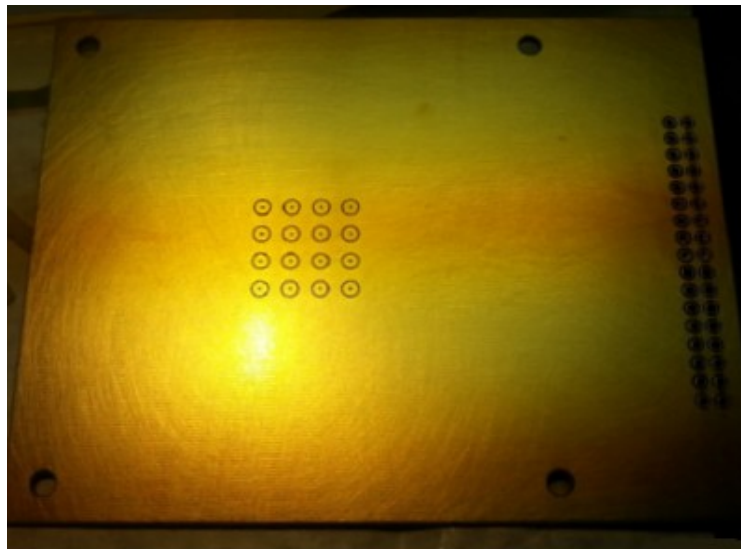
Pic. 5.2.2: picture of the PCB anode.

The anode is made in 4 layers PCB (Printed Circuit Board): the 1st for the pixelated anode, the 2nd for shielding, the 3rd for electrical connections ad the 4th layer for shielding again. In the first layer there are 16 pads, disposed in a 4 x 4 matrix. Each pad is 2 mm diameter circle with a pitch of 4

mm. Surrounding these pads (with an insulating thickness of 0.2 mm) there is a ground electrode.

The layout of the electrical connections of the 16 pads is drawn in pic. **5.2.3**. Between each couple of signal connection lines there is a ground connection to avoid cross talk effects. The PCB anode was printed at CERN.
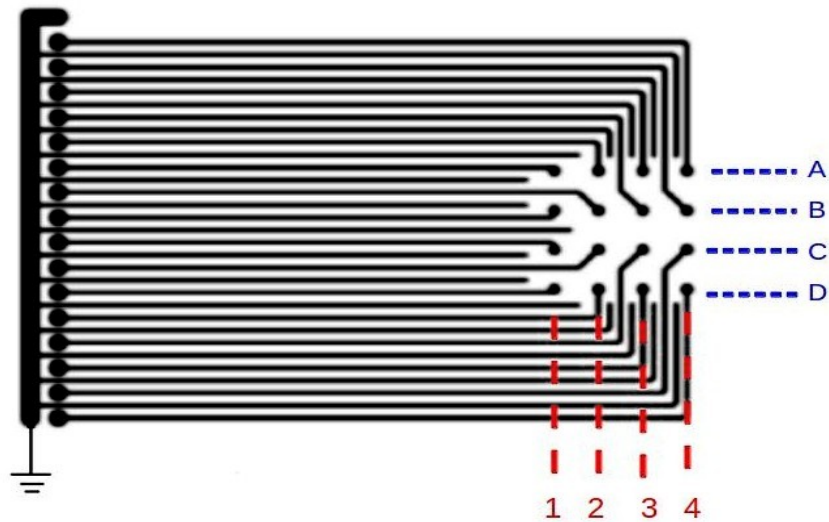

Pic. 5.2.3: *Electrical connections of the pixelated anode. Every collecting pad is defined trough a letter and a number.*

The pad where signal is collected define the collecting volumes: wall-less cylinders 2 mm high and with circular bases of 2 mm in diameter. If a ionising particle crosses this volume, producing some ionizations electrons, the signal created by the avalanche of electrons, produced in the region of amplification, is collected in the corresponding pad.

5.2.3 Cathode

The cathode is made in plastic A-150, a tissue-equivalent material that allows to simulate standard biological tissue (see paragraph **3.1**).

The cathode used for first experimental measurements has four holes to safely position the ^{244}Cm alpha source used for effective gain measurements (see paragraph **7.3**). Each one of them is aligned with 4 of the 16 pad of the anode. Under the source's place there is the collimation hole of 0,5 mm diameter.
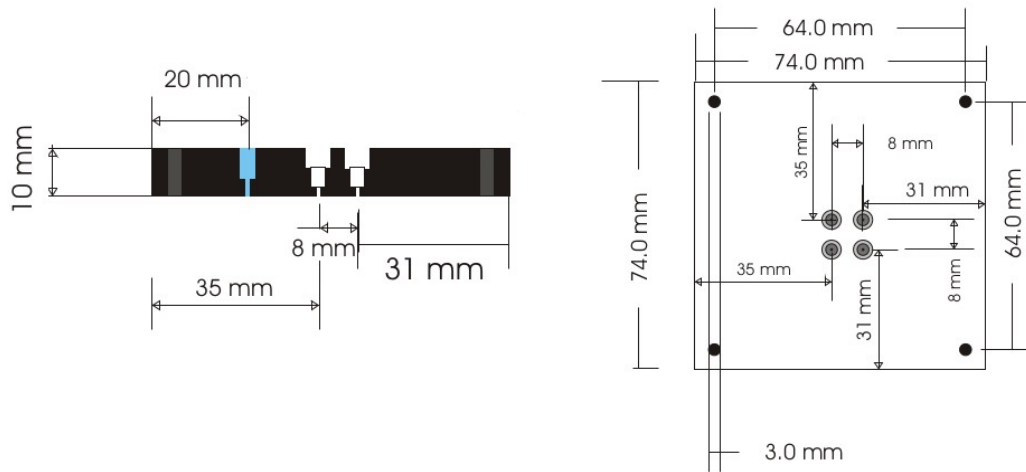
Pic. 5.2.4: Schematic view of the cathode, from the side (left)and from the top (right)
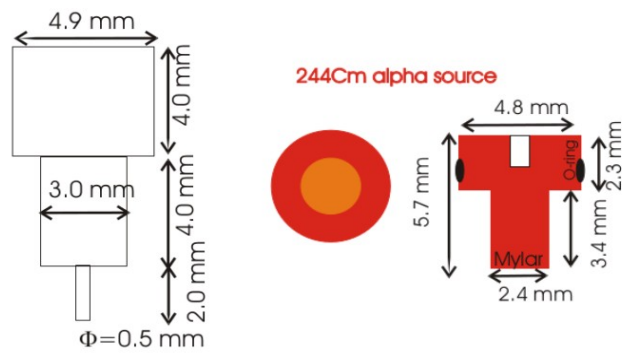
Pic. 5.2.5: Particular of one cathode hole, and comparison with alpha source used.

6. Experimental set-up

6.1 Measurement chamber

The detector is inserted in a vacuum tight chamber, holding the hermetic feedthroughs for the high voltages and the signal lines and for gas inlet and outlet.

The experimental chamber used has the vacuum system and the flow system presented in pic. **6.1.1**. The vacuum pumping is performed by two lines: using a rotary pump ALCATEL mod. 2012A up to a pressure of 10^{-1} mbar, and then through a pump PFEIFFER turbomolecular/BALZERS mod. PM P01, and a rotary pump PFEIFFER/BALZERS mod. DUO 016B, that allowed to reach 10^{-5} mbar. For the measurement of the pressure inside the chamber, we used two Pirani pressure gauges EDWARDS mod. PR 10 - K, 10 - S (P1 and P2 in the figure), sensitive to pressures down to 10^{-3} mbar, and a Penning gauge EDWARDS mod. CP - 25 S (P3 in the figure) for lower pressures. In carrying out the measurements the system is initially brought in vacuum to ensure a negligible presence of atmospheric gas in the chamber and then kept in a stream of propane C_3H_8 at a pressure of 280mBar. To achieve this condition, a Flowmeter (MKS 1259 HP) makes the propane gas flow inside the chamber. The gas is transported to the multiplication region through a small tube 3 mm diameter. At the same time, according to the pressure read by the gauge absolute MKS 627 A11MDC (P4 in the figure) with 0.1% of accuracy, the MKS Pressure Controller 600 series rules suitably the valve v2 allowing the gas flowing, and accordingly keeping constant the pressure inside the chamber.

The gas purity is an important factor that can strongly influence the stability of the gas gain and the reproduction of the measurements. Working with a continuous gas flow supply system ensure the gas purity.
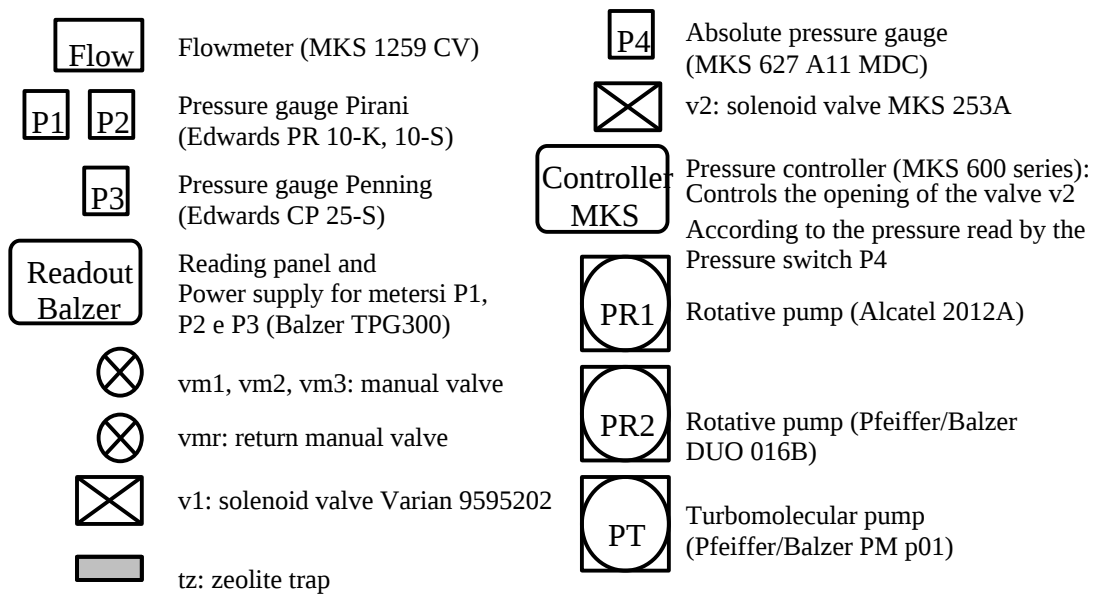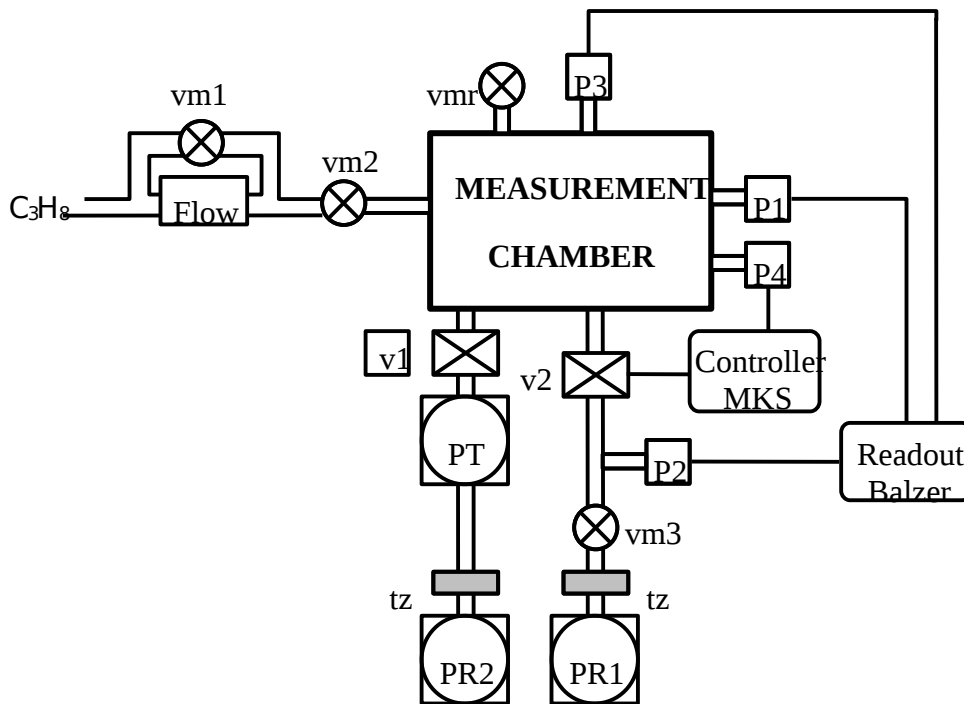
Pic. 6.1.1: *Schematic of the measurement chamber.*

6.2 Power supply of the GEM detector

The High Voltages are connected to both sides of the GEM foil (we are going to refer to the nearer to the anode as the Low Voltage Gem, and to the opposite as the High Voltage GEM) and to the cathode (Drift Voltage) with a filter to protect the detector from voltage surges.

The terms Low Voltage and High voltage are due to the fact that we measured keeping the anode at ground potential and applying negative HV to the GEM and the cathode.
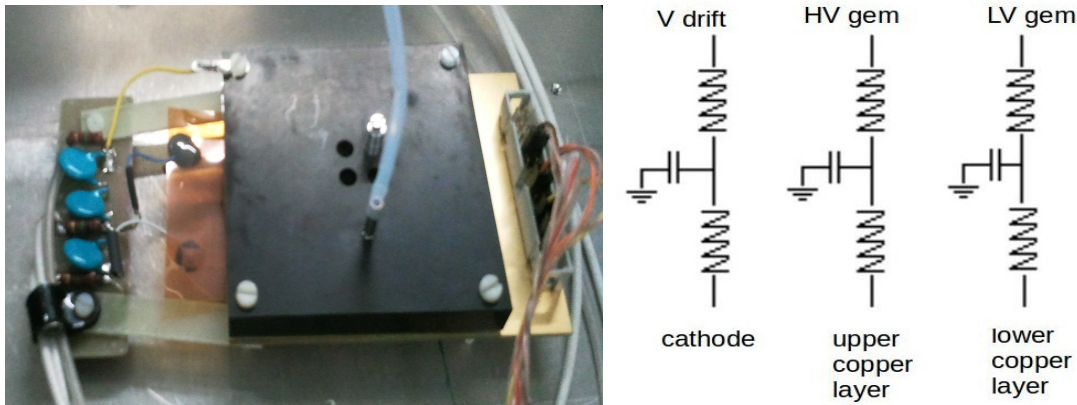
Pic. 6.2.1: *Picture of the detector and schematic of the protection filter. Resistance are 1MΩ .*

High voltage was supplied in first place using a ORTEC 710 module. This module contains four high-voltage power supplies that have independently selectable output voltages and polarities. Each supply can deliver an output voltage that is continuously adjustable over the range from 0 to ±100 V or from 0 to ±1 kV, with a maximum output current of 20 µA, the minimum current shown is of 10 nA.

After first measurements with the ORTEC module, we replaced it with a CAEN N1471H. This choice was motivated by the handling procedure of the GEM foil: it's recommended to never exceed few tens of nA of leakage current while powering the GEM.

The Mod. N1471H provides 4 independent High Voltage channels in a NIM module. Each channel can provide a 5.5kV/20 µA max output. It also includes safety features as:

• Over-voltage and Under-voltage warning when the output voltage differs from the programmed value by more than 2% of set value (minimum 10V).

• Programmable V_{MAX} protection limit .

• Over-current detection: if a channel tries to draw a current larger than its programmed limit, it is turned off.

• Channels can be enabled or disabled individually through the Interlock logic.

With the usage of this module we were able to collect measurements safely also with an high potential difference applied to the GEM foil (near 500V).

It should be emphasized that the probability of the transition from proportional multiplication to discharge at a given voltage depends on many internal and external factors, such as temperature, humidity and gas flow.

6.3 Electronic chain

The electronic chain used for the acquisition is schematically shown in pic. **6.2.1**. The signal collected in the PCB anode is sent to the pre-amplifier. The anode was hold at ground potential, while negative high voltage was applied to the GEM foil and the cathode (drift potential). This set-up has the advantage of eliminating high voltage on the anode feed-through which may cause noise. The pre-amplifier is kept outside the measurement chamber for convenience: in this first phase of the experiment we want to test several different pre-amplifiers, so we decided to connect the output signal from the detector to the pre-amplifier with cables, (keeping them as short as possible) instead of connecting it inside the vacuum chamber, even if it means an increase in noise [85].

The output signal from the pre-amplifier do not undergoes an analogical process of signal formation, i.e. by means of a shaping amplifier and peak detecting ADC, but it is directly connected to an Analog to Digital Converter CAEN DT5724, that converts the input signal into digital form before applying the energy filter. The signal processed by the CAEN module, is recorded in a computer.
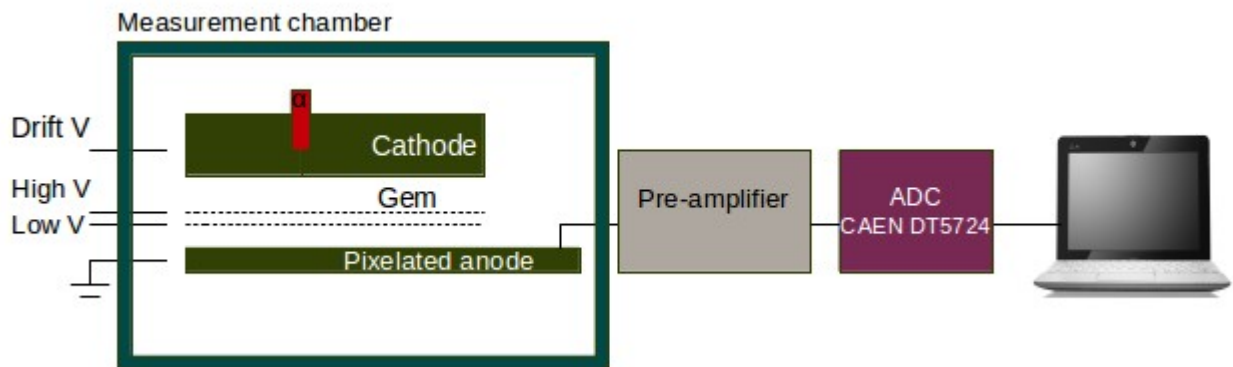
Pic. 6.3.1: *Schematic of the electronic chain.*

Every single element of the electronic chain is further explained in the following paragraphs.

6.4 Pre-amplifier

The signal collected at the anode is sent into the pre-amplifier. We tested three kind of pre-amplifiers: two commercial pre-amplifiers, Cremat CR110 and Cremat CR111, and one developed by the University of Padova.

The cabling between the detector and pre-amplifier was kept as short as possible, but accordingly to previous studies [22, 85], to obtain a significant reduction in noise pre-amplifiers should be built

into the detector housing. To can easily test different pre-amplifiers, we kept them outside the detector chamber, but final design will have them as close as possible to the detector.

We made some experimental measurements of the pre-amplifiers specification: noise level, gain factor, rise time and linearity. For the measurements we used the Pulser HP 8116A to generate input signal, and Tektronix TPS 2012B 2-channels oscilloscope.

To power the pre-amplifiers, two different power supplies were tested:

-Two Agilent E3612A DC power supply

-One AimTTi EL302RD dual power supply

In table **2** we report the noise level measured with both power supplies for different pre-amplifiers. The final choice was made for the last one, since it appreciably decreases the electrical noise.

Pre-amplifier	Noise in electrons RMS with 2 Agilent E3612A	Noise in electrons RMS with AimTTi EL302RD
CR110	1818	821
CR111	1702	938
preUNIPD	1203	410

*Table 2: Noise level for different pre-amplifiers with both power supplies.*

6.4.1 CR110 and CR111

These pre-amplifiers are mounted on a 8-channel acquisition board. Each channel includes a low noise charge pre-amplifier, connected as shown in the circuit picture (**6.4.1**).

For the first measurements only 4 channels have been used: 2 with pre-amplifiers CR110, and 2 with the pre-amplifiers CR111.
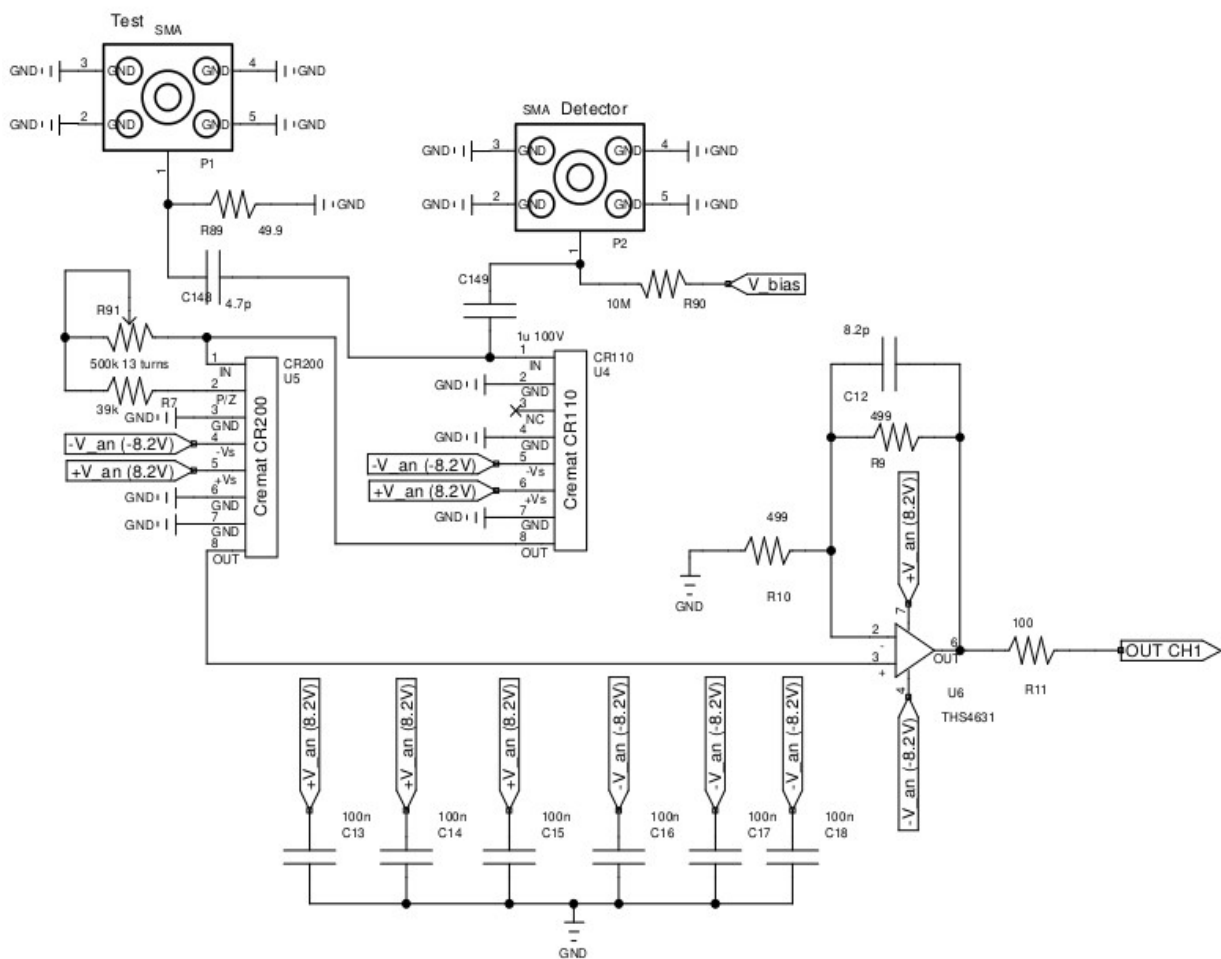
Pic. 6.4.1: *Assembly diagram of a preamplifier CREMAT. The original design included also the presence of an amplifier CR200 which was subsequently removed from the card and replaced with a bridge.*
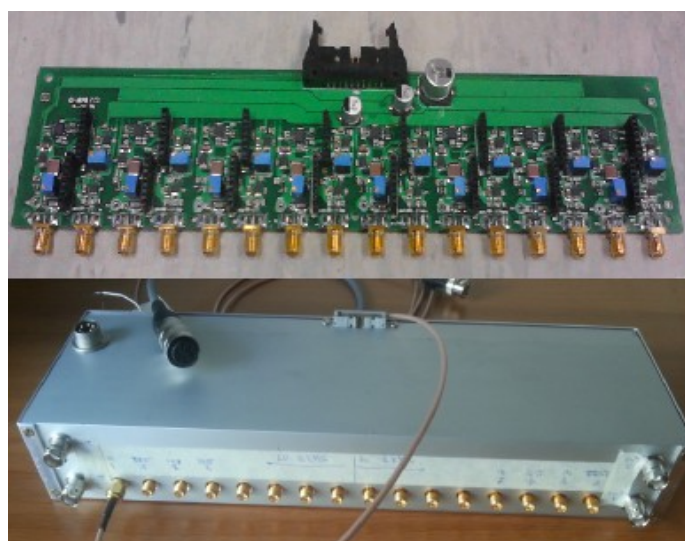
Pic. 6.4.2: *8-channel board.*

The nominal characteristic of the pre-amplifiers are reported in table **3**:

Pre-amplifier model	Gain [mV/pC]	Noise (ENC) in electrons RMS*	Rise time** [ns]	Unsaturated output [V]
CR110	1400	200	7	-3/+3
CR111	130	630	3	-3/+3

*Table 3: Nominal characteristic of Cremat pre-amplifiers.*

* 1µs of shaping time, input unconnected.

** Pulse rise time defined as the time to attain 90% of maximum value, with 0 added input capacitance. With non zero capacitance C_d: $t_r = 0.4C_d + 7$ ns for CR110 and $t_r = 0.11 C_d + 3$ ns for CR111.

The nominal unsaturated output is -3/+3V if detected with an high impedance instrument. The CAEN ADC we used has 50Ω of input impedance therefore linearity measurements have been performed using the oscilloscope with 50Ω input impedance, to recreate the same conditions of a spectrum acquisition. Rectangular pulses generated by the pulser were fed into the test input of the pre-amplifiers and output signal height were measured by means of the oscilloscope; by modifying the input pulse height, we checked the linearity of pre-amplifiers inside the unsaturated output range. In pic. **6.4.3** and **6.4.4** the results obtained for CR110 and CR111 are plotted.
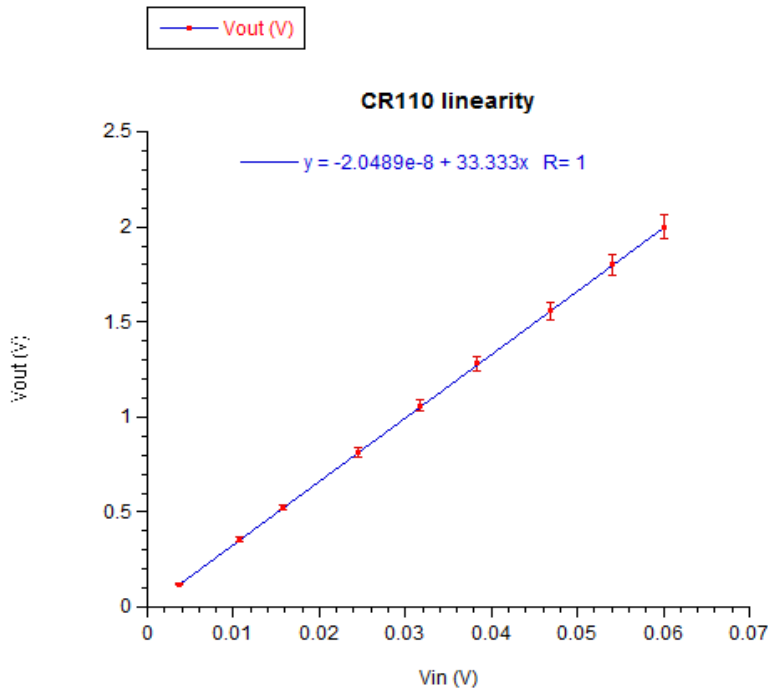
Pic. 6.4.3: Linearity for CR110 pre-amplifier.
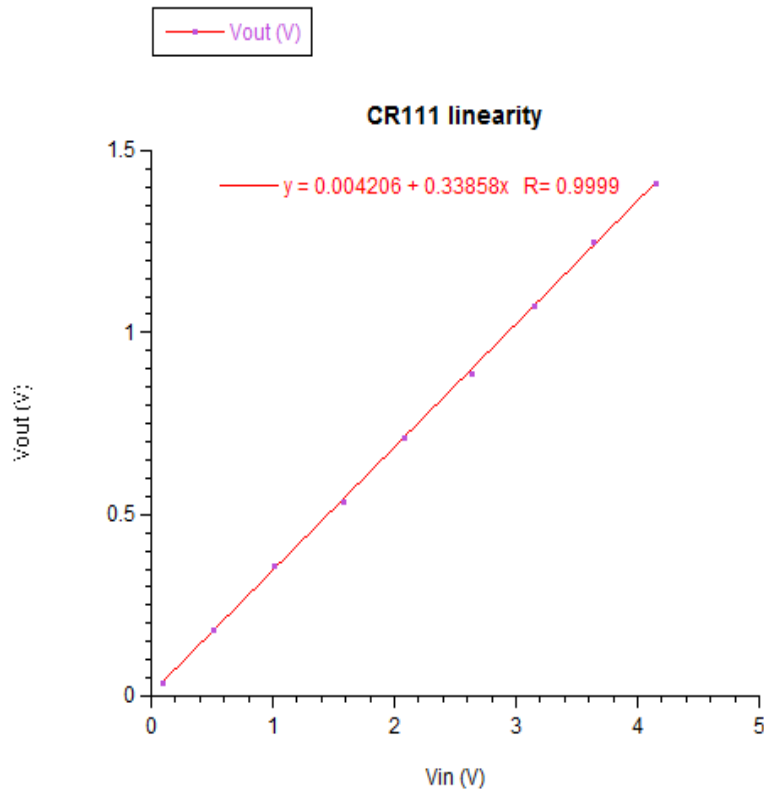
Pic. 6.4.4: *Linearity for CR111 pre-amplifier.*

The unsaturated positive output range for the Cremat pre-amplifiers, using a 50Ω of input impedance is:

CR110: 0/+1.8 V

CR111: 0/+1.56 V

The gain factor of the pre-amplifier is given by the following relationship: $G = \dfrac{V_{out}}{V_{in} \cdot C}$

where C is the feedback capacitor, and V_{in} and V_{out} the height of the input signals, respectively. By considering the nominal feedback capacity value of 4.7pF with uncertainty of 10%, and measuring the height of the signals with the oscilloscope, the following gain factors were obtained:

G=(1.27±0.07) V/pC for the CR110

G=(0.116±0.006) V/pC for the CR111.

83

The value obtained for the CR110 agrees, inside the error, with the nominal value of 1.24 V/pC, while the value obtained for the CR111 is slightly lower than the nominal one of 0.13 V/pC.

In pic. **6.4.5** are shown the rise time of two CREMAT pre-amplifiers unconnected, that have consistent value when compared with nominal value reported in table **3**: 6.7±0.2 ns and 3.2±0.1 ns for the CR110 and CR111 respectively.
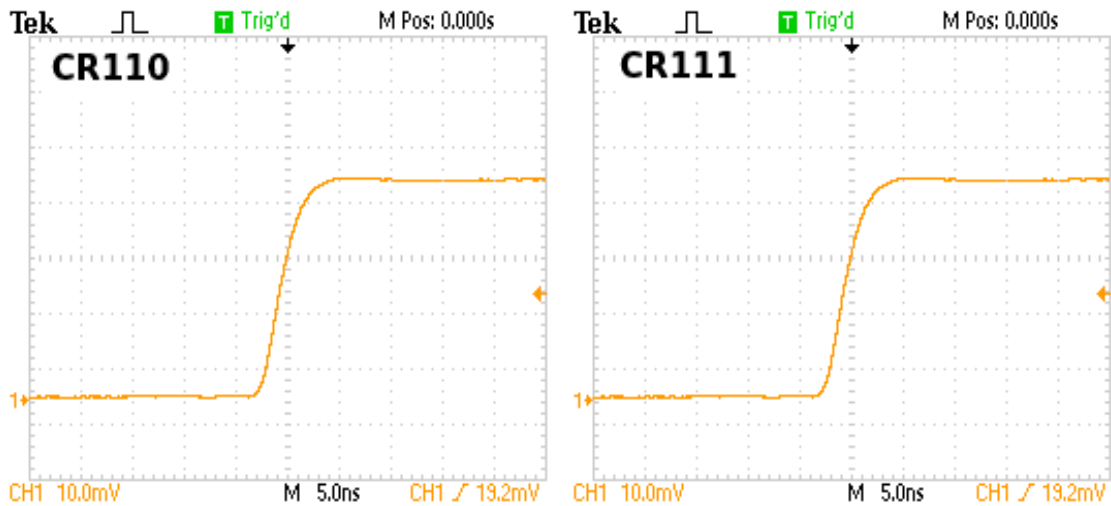

Pic. 6.4.5: *Rise time of CREMAT pre-amplifiers unconnected.*

In pic. **6.4.6** and **6.4.7** are shown the signal shape of the CR110 and CR111 pre-amplifiers output with the detector connected, using a pulser signal as input signal. By using the oscilloscope, we measured a rise time of 65.6±2.0 ns and 19.2±0.6 ns respectively for CR110 and CR111.

Referring to [89] for CR110 and [90] for CR111, from the signal rise time we can calculate the detector capacitance, using: $t_r = 0.4C_d + 7 = 65.6$ ns for CR110 and $t_r = 0.11 C_d + 3 = 19.2$ ns for CR111 we obtain the results shown in table **4**.

| Pre-amplifier model	Detector capacitance (pF)
CR110	146.5±4.8
CR111	147.3±5.5

Table 4: *Detector capacitance.*
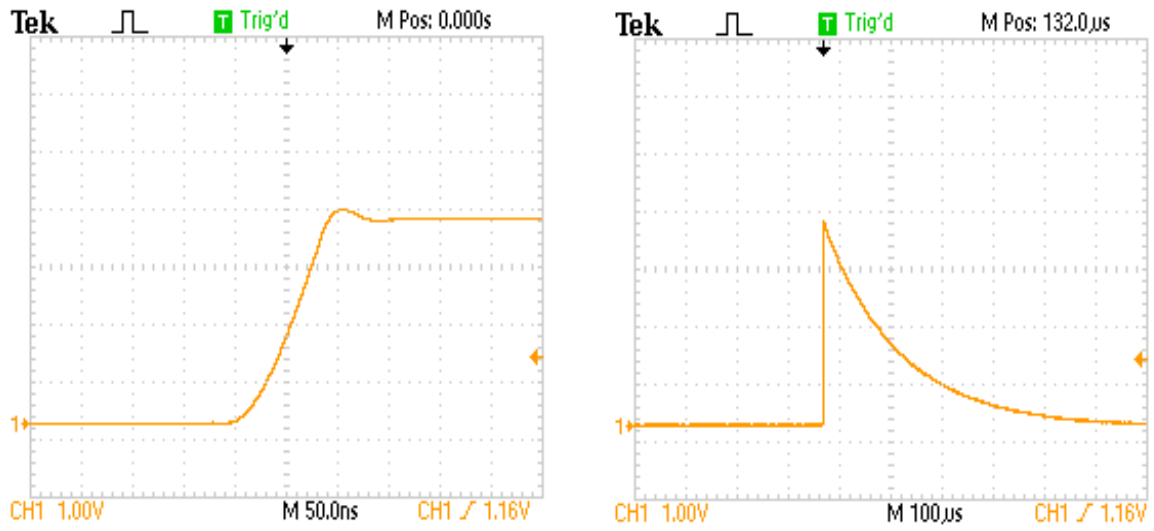
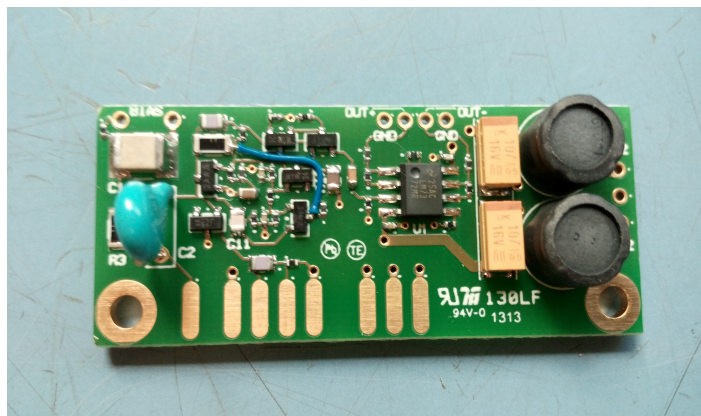*Pic. 6.4.6:* *Waveform of the output from the CR110 with the detector connected.*
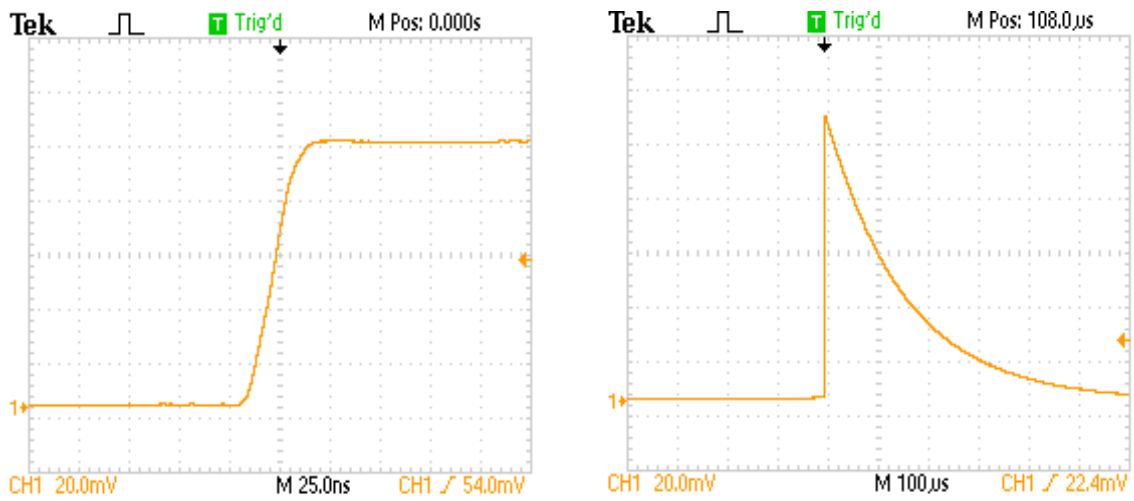
Pic. 6.4.7: *Waveform of the output from the CR111 with the detector connected.*

6.4.2 Pre-amplifier developed in Padova

This pre-amplifier developed at Padova University is composed as shown in pic. **6.4.8**
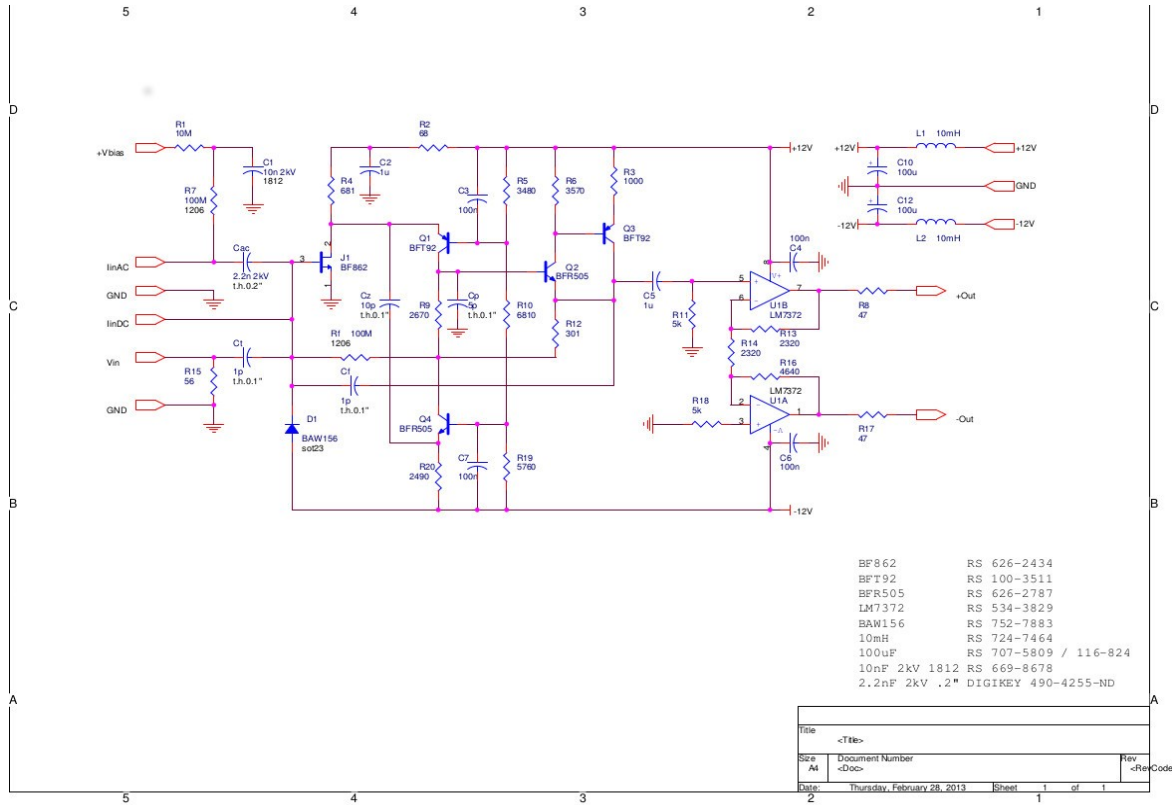
Pic. 6.4.8: *Schematic of the composition of the pre-amplifier.*

Pic. 6.4.9: *Picture of the pre-amplifier.*

The characteristic of this pre-amplifier were investigated by its designer, F. Dal Corso and his results are summarized in table **5**:

Pre-amplifier model	Gain [mV/pC]	Noise (ENC) in electrons RMS	Rise time* [ns]	Unsaturated output** [V]
preUNIPD	1.1	180	5	0/4.5

Table 5: *Characteristics of the pre-amplifier developed in Padova.*

* Detector unconnected, C_d=0 pF.

** Measured with an input impedance of 50Ω

Using the pulser output and the oscilloscope, we checked the linearity of the pre-amplifier inside the unsaturated output range. In pic. **6.4.10** it is shown the plot obtained, compared to the data taken by F. Dal Corso during his tests.
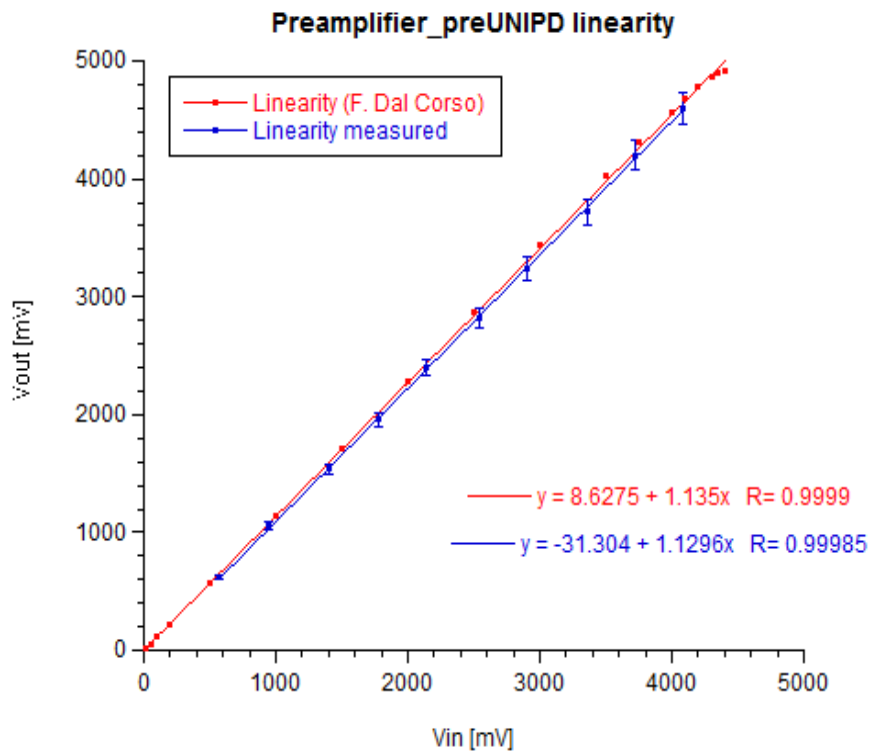
Pic.6.4.10: *Linearity for the pre-amplifier developed in Padova, measured by us in Legnaro, with the instruments nominated above, and linearity for the same amplifier measured by F. Dal Corso, his developer.*

The nominal unsaturated output range for this pre-amplifier is 0-4.5V with low input impedance (50Ω). We measured 0-4.6V with a 50Ω input impedance.

The gain factor has been calculated by using the formula:
$$G = \frac{V_{out}}{V_{in} \cdot C}$$

and taking into account the nominal feedback capacity value of 1pF with uncertainty of 10%. The gain factor obtained is: 1.066±0.003 V/pC.

In pic. **6.4.11** is shown the signal shape of the pre-amplifier output using a pulser signal as input signal, and detector unconnected. The rise time measured is about 6 ns, consistent with Dal Corso measurements.
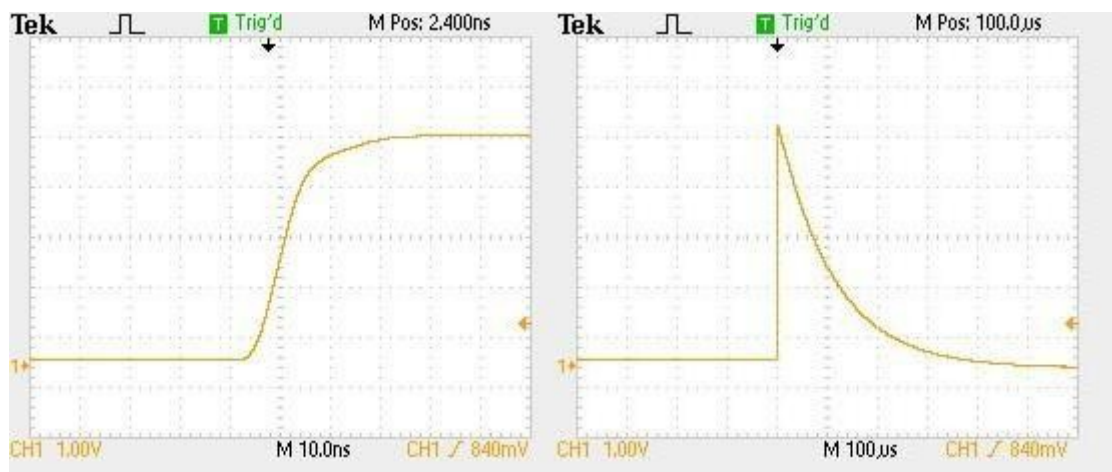
Pic. 6.4.11: Waveform of the output from the pre-amplifier developed in the University of Padova.

In pic. **6.4.12** can be seen how the rise time grows with the detector connected. The rise time become 72±2 ns. Using the detector capacitance found with CREMAT pre-amplifiers, we can calculate the scale factor of the rise time with the capacity: $t_r = \eta C_d - 5$ ns=72 ns, and $\eta = 0.5$ using $C_d \sim 145$ pF.
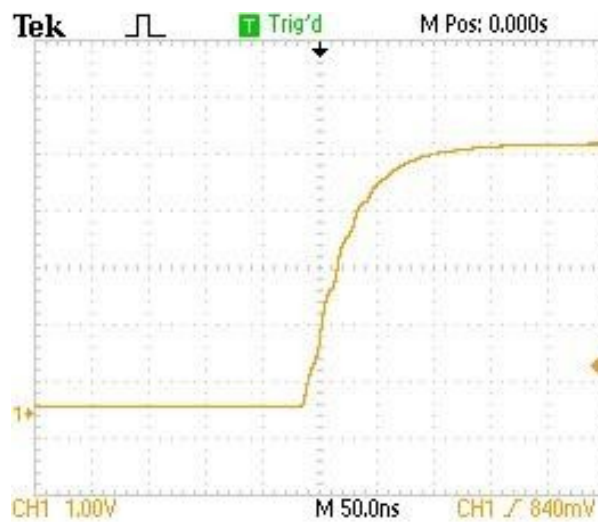
Pic. 6.4.12: *Rise time shape of the pre-amplifier developed in Padova with the detector connected.*

The signal from the pre-amplifier was sent into the Analog to Digital Converter CAEN DT5724.

6.5 ADC: characteristic and set-up

Data were acquired through the CAEN DT5724 digitizer equipped with a FPGA with DPP-PHA (Digital Pulse Processing for Pulse Height Analysis) firmware. In this configuration DT5724 provides a digital replacement of Shaping Amplifier and Peak Sensing ADC (Multy-Channel analyzer).

The Mod. DT5724 is a 4 Channel 14 bit 100 MS/s (million of samples per second) Desktop Waveform Digitizer with 2.25 Vpp dynamic range on single ended MCX coaxial input connectors. The DC offset is adjustable via a 16-bit DAC on each channel in the ±1.125 V range in order to preserve the full dynamic range also with unipolar positive or negative input signals.

The data stream is continuously written in a circular memory buffer. When triggered, the FPGA

writes further N samples for the post trigger and freezes the buffer that is read via USB. The acquisition can continue dead-timeless in a new buffer.

Each channel has a SRAM memory buffer divided in buffers of programmable size (1 - 1024). The readout of a frozen buffer is independent from the write operations in the active circular buffer (ADC data storage).

The trigger signal can be provided via the front panel input as well as via the software, but it can also be generated internally with threshold auto-trigger capability. DT5724 houses USB 2.0 and optical link interfaces. USB 2.0 allows data transfers up to 30 MB/s, and this type of connection was chosen for the experimental measurements.

Pic. 6.5.1: CAEN DT5724 Analog to Digital Converter.

Unlike the traditional acquisition chains for spectroscopy, in which the signal is treated by a certain number of analog blocks and then converted to digital at the end of the chain, in a digital MCA (Multi-Channel Analyser) this approach has been reversed: the A/D conversion is performed at the input of the module by a flash ADC whose output data (a continuous stream of digital samples) are managed by an FPGA that applies filters and algorithms for the extraction of the quantities of interest, such as the pulse height for the energy calculation, the baseline, the time stamp, etc..
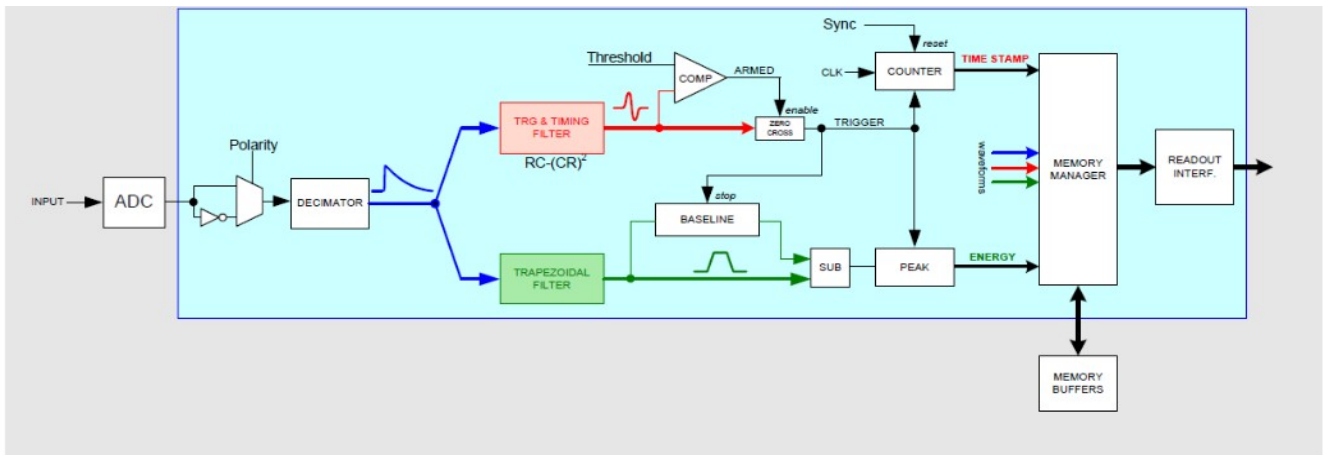
Pic. 6.5.2: Block Diagram of the processing chain programmed into the CAEN DT5724.

The block diagram is shown in pic. **6.5.2**, and the entire chain of components is described in the next subsections, and the chosen parameters for the acquisition are explained:

6.5.1 Decimator

The first block after the polarity selector is a decimator filter; this can be used in the case the signal is particularly slow, hence it is necessary to set values for the Digital Pulse Processing (DPP) time parameters that are not within the allowed range. The effect of the decimator is to scale down the sampling frequency of a factor 2, 4 or 8; it might have also benefits in terms of noise, since it averages a certain number of samples to make a new sample for the data stream.

We decided to keep the decimator at the standard value: 0.

6.5.2 Trigger and Timing Filter

After the decimator, there are two parallel branches: one for timing and triggering, the other one for the energy. The aim of the Trigger and Timing Filter (TTF) is to identify the input pulses,

generate a trigger on them and calculate the time stamp. Usually, the digitizers and the oscilloscopes feature a self-trigger based on a programmable voltage threshold: the trigger is generated as soon as the the input signal crosses the threshold. This technique may lead to missing pulses or to the detection of false triggers, because of baseline fluctuation, pulse pile-up, noise, etc. To reduce these effects, digital filters may be applied to reduce the noise, cancel the baseline and to perform shape and timing analysis. There are many types of timing and triggering filters: the one adopted by CAEN is like a RC-CR^2 filter: the integrative component is a smoothing filter based on a moving average filter that reduces the high frequency noise and prevent the trigger logic to generate false triggers on spikes or fast fluctuation of the signals.
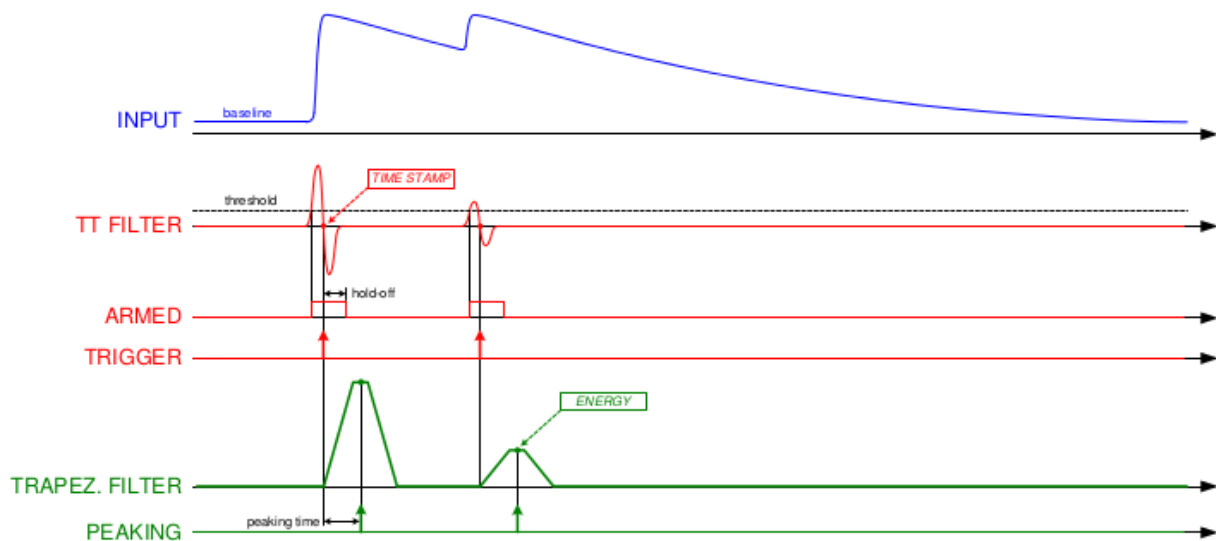
**Pic. 6.5.3:** *schematic representation of the signal processing.*

Instead, the purpose of the derivative component is to subtract the baseline, so that the trigger threshold is not affected by the low frequency fluctuation and, that is more important, by the pile up. As a result of the double derivation (CR^2), the output signal of the TTF is bipolar and the zero crossing is independent of the pulse amplitude. This is the same principle of the Constant Fraction Discriminator, although the algorithm is different. The trigger logic uses the threshold to get armed, then waits for the zero crossing to generate the trigger signal. The digital derivation is obtained by the difference between two samples separated by a programmable gap: Di = Si – Si-k, where *k* is the gap that can be programmed by means of the *Delay* parameter: usually, in order to

maximize the amplitude of the TTF output, *k* is set to a value between one and two times the rising edge of the input signal. We set the Delay parameter to 0.1μs.

### 6.5.3 Trapezoidal Filter (Energy Filter)

The trapezoidal filter (TF) for the energy calculation has the same purpose of the Shaping Amplifier in the analog MCA: it transforms the long exponential decay of the signal into a trapezoidal shaped signal whose amplitude is proportional to the input pulse height (energy). In order to reduce the pile-up, the duration of the trapezoid is usually much shorter than the input exponential pulse; the user can program the rise time of the trapezoid (that is always equal to the fall time) as well as the width of the flat top. In analogy with the shaping time of the analog systems, choosing the rise time of the trapezoid is a compromise between resolution and pile-up rejection (dead time): a long shaping time gives a better resolution but has higher probability of pile-up. It is also possible to program the position on the flat top where the peak is calculated; this setting is particularly important for large volume detectors in which the ballistic deficit causes a significant error in the energy calculation; this error can be corrected by delaying the time at which the trapezoid peak is sampled, thus waiting for the full charge collection. The trapezoid, like the Gaussian pulse of the shaping amplifier, requires an accurate pole-zero cancellation in order to guarantee the correct return to the baseline at the end of the falling edge; in theory, when the pole-zero compensation is perfect, after a finite and deterministic time equal to 2TR + TF (where TR is the rise/fall time and TF is the flat top) the output of the trapezoidal filter goes back to the baseline. This is a great advantage of the digital filter compared to the analog shaping amplifier in which the tail of the pulse is unlimited, at least from the mathematical point of view.

To evaluate the best parameters for our application, we proceed simulating with the pulser HP 8116A the shape of the signal coming out from the detector, and used that signal to optimize the ADC parameters that affects the trapezoidal shape, as the decay time (see pic. **6.5.5**). To evaluate the decay time, we checked the correct return of the trapezoid to the baseline at the end of the energy filter. This parameter is similar to pole zero correction for a Gaussian shaping amplifier. Effects of the bad choice of the decay time can be seen in pic. **6.5.5**. The final choice for this parameter is 130μs with all pre-amplifiers used.
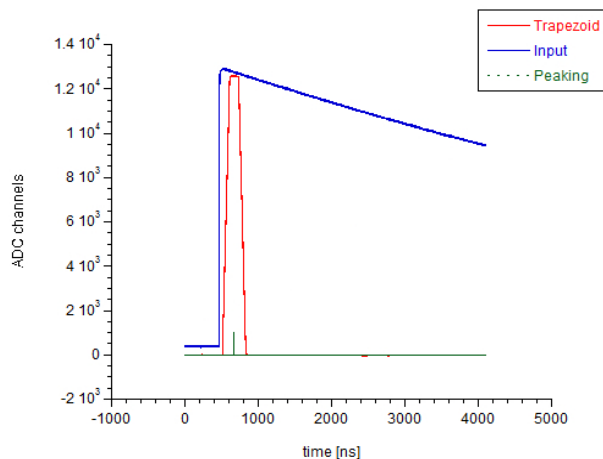
Pic. 6.5.4: Trapezoidal waveform, input signal and peaking as they are created by the CAEN ADC.

Once we obtained a satisfactory trapezoidal shape, we proceeded acquiring different spectra with the alpha source, optimizing the ADC parameters to obtain a correct peaking measurement (see pic. **6.5.6**). In pic. **6.5.6** the light blue alpha peak is shifted by 3% because of the wrong peaking value: with a flat top of 5 μs, taking the peak after 0.67 μs correspond to a systematic underestimation of the peak height. The red, green and blue signals instead, are comparable with each other. We chose a rise time of 1μs, that's a good compromise between 7μs (more stable flat top, but can be a problem with faster source) and smaller ones, that are good to avoid pile-up, but create a very unstable flat top, observed with the signal shape function of the ADC. For the flat top length, the final choice was to keep it at 1.2μs, and the peaking occurs after 0.7μs. This set-up was chosen because of the good performance, despite the short time duration of the trapezoidal signal.
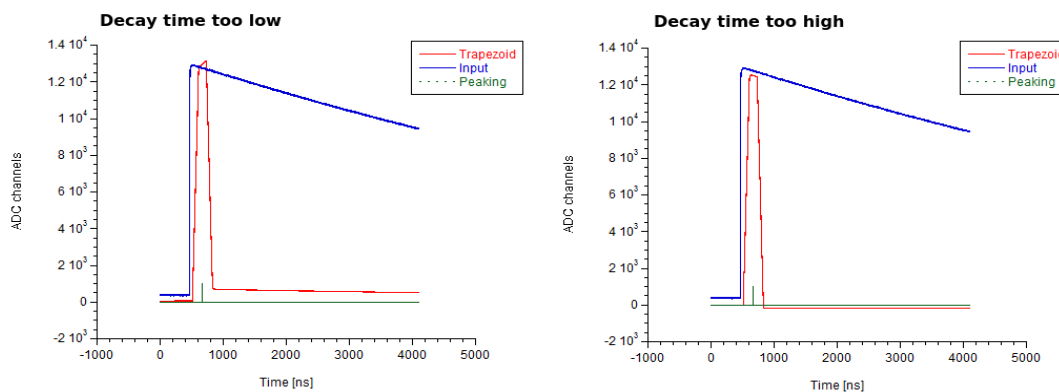
Pic. 6.5.5: Bad decay time setting effects on trapezoid signal.

94
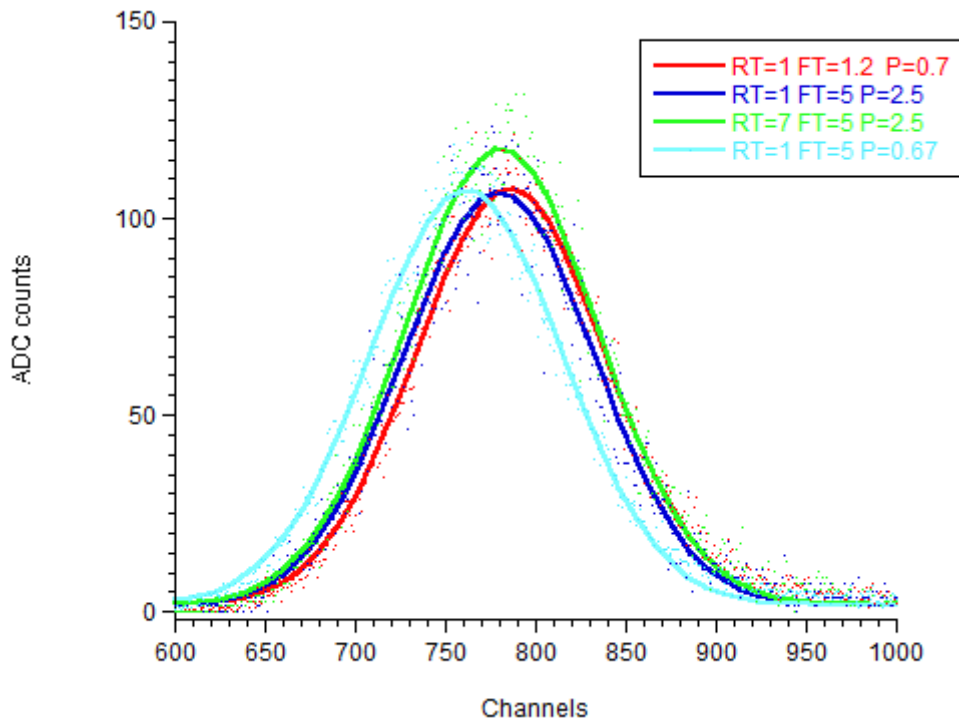
Pic. 6.5.6: *Comparison between different set up of the ADC with the signal of the alpha source [244]Cm: RT means Rise Time, FT Flat Top and P for Peaking. All values are expressed in µs. Shifting of the light blue peak is due to a wrong peaking choice, that underestimate the energy of the trapezoid. All spectra are acquired at 330V across the GEM.*

6.5.4 Baseline Restorer

The energy filter includes also a baseline restorer; this operates on the trapezoidal filter output and calculates the baseline by averaging a programmable number of points before the start of the trapezoid. The baseline is then frozen during the ramp up and used in the height calculation. Once the trapezoid is returned to the baseline (ramp down), the averaging restarts to run. The pulse height (i.e. the trapezoid amplitude) is given by the distance between the flat top and the baseline taken in the programmed position; in order to further reduce the fluctuation of this distance due to the noise, it is possible to average a certain number of points in the flat top before subtracting the baseline.

The Baseline Mean parameter was chosen to be 16384 , the maximum possible of points to be

mediated for the baseline calculation, to have a Baseline calculation as correct as possible, and avoid incorrect estimates of the energy filter.

Baseline holdoff was set to 1μs. The baseline calculation is inhibited from the start to the end of the trapezoid, plus 1μs. This value was chosen to be absolutely certain of the end of the trapezoid filter before starting calculate the baseline.

6.5.5 Dead time

In case of signal saturation (**Pic. 6.5.7**), if the input signal is over-range (exceeds the input dynamic range of 16k ADC channels) the acquisition is inhibited. As soon as the input signal is out of saturation a fake event is saved. This fake will have the energy value set to FFFF (the maximum possible value of a 4-bit signal in hexadecimal base). The dead time is equal to the time difference between the last trigger occurred and the fake-event trigger after the saturation.
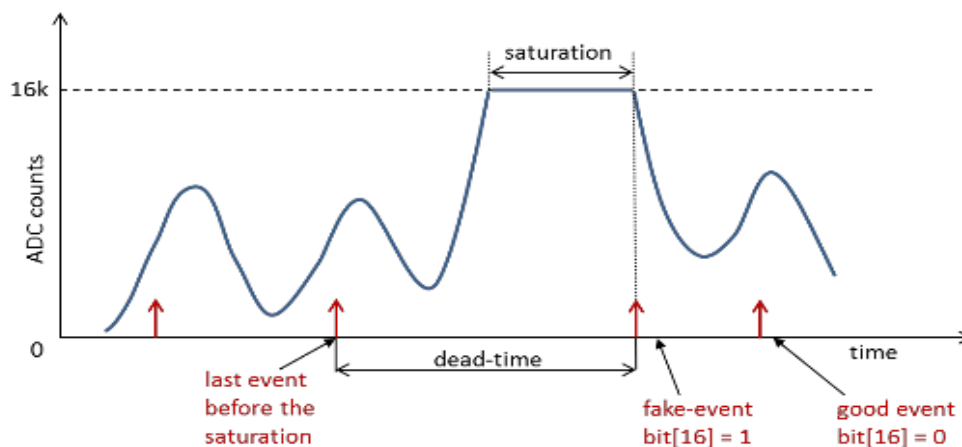
Pic.6.5.7: *Dead time in case of signal saturation*

To powering the ADC we consider an AimTTi EX354RD dual power supply and the external AC/DC stabilized power supply provided with the digitizer, and included in the delivery kit.

As can be seen in pic. 6.5.8, better performances in term of noise are found using the AC/DC stabilized power supply (referred as AC in the graph) although more signal are collected, they have minor height. For our purpose this is preferable, but it can be a limit in high rate acquisition

96

performances.
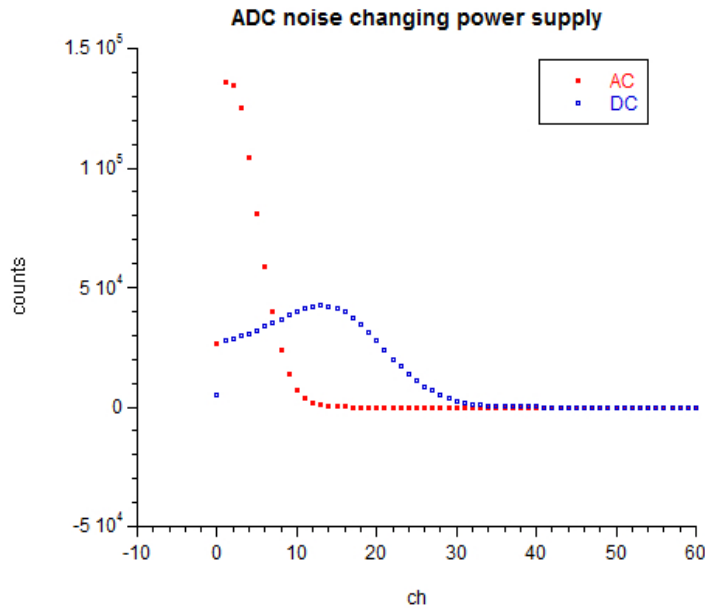
Pic. 6.5.8: *Comparison on the ADC noise using different powering supply. Acquisition is taken with a threshold of 10 channels.*

It's worthy to specify that the trigger logic uses the threshold to get armed, then waits for the zero crossing to generate the trigger signal. This means that the threshold doesn't work as in the analog systems, cutting the first part of the spectrum, but instead, if a noisy signal arms the trigger, the conversion of the signal into a trapezoidal shape begins, and if there is no effective signal after the rise time of the trapezoid, the ADC register a signal of amplitude between 0 and the threshold anyway. Increasing the threshold, the probability of arming the trigger on noise instead of on a signal diminish, but there is no guarantee to cut the spectrum below a certain value.

We checked the linearity of the channels of the CAEN ADC using a ramp generator BNC LG-1. We find out that at high frequency (over few hundreds Hz) CAEN acquiring system overestimates counts between channels 0 and 2500. It is a problem that could be linked to decay time of the output signal from the pre-amplifier, it is probably related to an error in the digitizing the input signal. This problem doesn't affect the measurements of effective gain presented in next chapter, because the centroid of the alpha peak is always located beyond channel 2500.
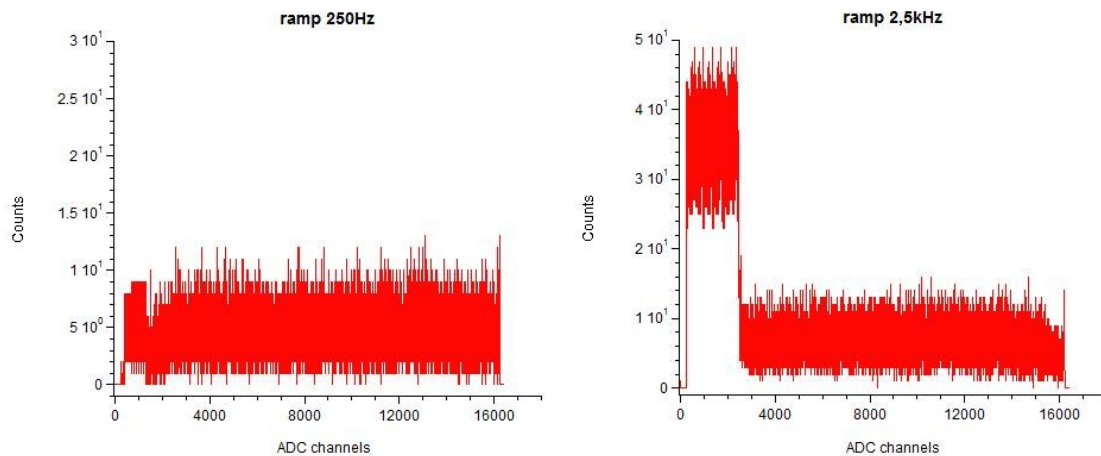
Pic. 6.5.9: Ramp generated histogram collected with the ADC CAEN at difference frequencies.

The alpha spectrum obtained with the ADC CAEN shows a strange peak in lower channels, as can be seen in pic. **6.5.10**. It can be related to the threshold system of the CAEN ADC: after the digitalization of the signal, trigger starts when input value become greater than the selected value. If trigger starts on a noise fluctuation, when the energy filter calculates the height of the signal, the trapezoid can be 0-threshold value height. In this way, even though with a selected threshold, some counts are collected under it.
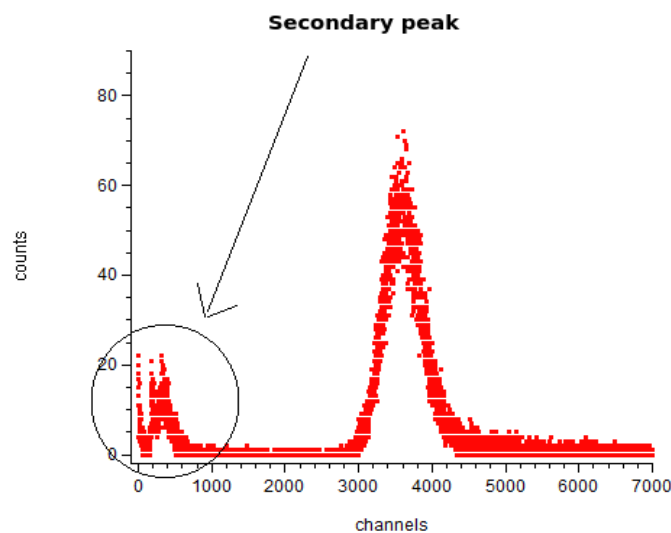
Pic. 6.5.10: Alpha spectrum with a potential difference across the GEM of 390 V.

In pic. **6.5.11**, it is shown how the peak evolves increasing the potential difference between GEM electrodes. The inferior limit seems to stay around the same channel, while the right part move forward to high energy. This behaviour open the possibility to consider it a real event, since it is well-formed by the pre-amplifier. It could be linked to some events due to the GEM configuration, such as electrons emission from the kapton foil, or to a secondary event related with electrons avalanches. The analogical CAMAC based acquiring system do not shows this peak (see pic. **6.5.13**), because this signal is comparable with the noise level.
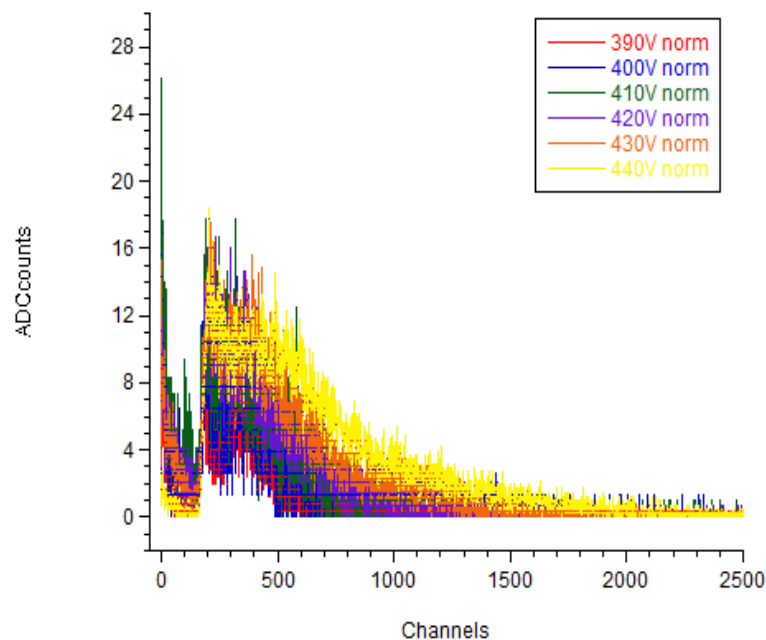
Pic. 6.5.11: Evolution of the secondary peak with the potential applied to the GEM electrodes.

To investigate this phenomenon, we take some measurements with an inverted drift field, i.e. applying on the cathode a potential such as the electrons drift to the cathode instead to the GEM foil. The resulting spectrum is shown in pic. **6.5.12**, and the little peak is still visible, therefore the peak is not due to an energy deposition event inside the sensitive volume of the counter.

Other investigations are needed to fully understand the origin of this peak (at least if it is a physical event or it is linked to the digital acquisition system).
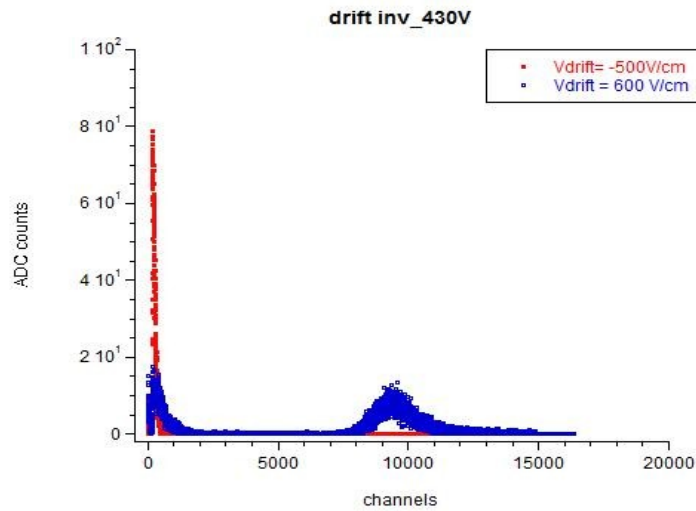
Pic. 6.5.12: *Comparison between alpha spectra acquired with a voltage across the GEM of 430V, and V_{drift} direct and inverted.*

To compare the performances of the CAEN ADC with those of an analogical system, some measurements have been performed with a CAMAC based system. In the CAMAC acquiring system, the output signal from the pre-amplifier is sent into a Shaping Amplifier Silena 7612/L, with a shaping time of 25ns, then into the CAMAC ADC AD413A QUAD 8K ORTEC where it is digitized and registered on the computer. To choose the parameters for the acquisition we proceed as for the CAEN module, creating a signal form the pulser with same characteristic as the signal coming out from the pre-amplifier, and then optimizing the parameters and the pole zero compensation.

We tested both ADC with a contemporary acquisition of alpha source (^{244}Cm). The position and the FWHM of the peaks are the same with both acquisition systems, the counting statistics is also the same. The difference in shape of spectra plotted in pic. **6.5.13** are due to the different resolution of the two system due to the different numbers of channels: 16 384 for CAEN acquiring system, and 8192 for the CAMAC one.

CAMAC system shows an higher noise detection, that can be related to the connection cables used.
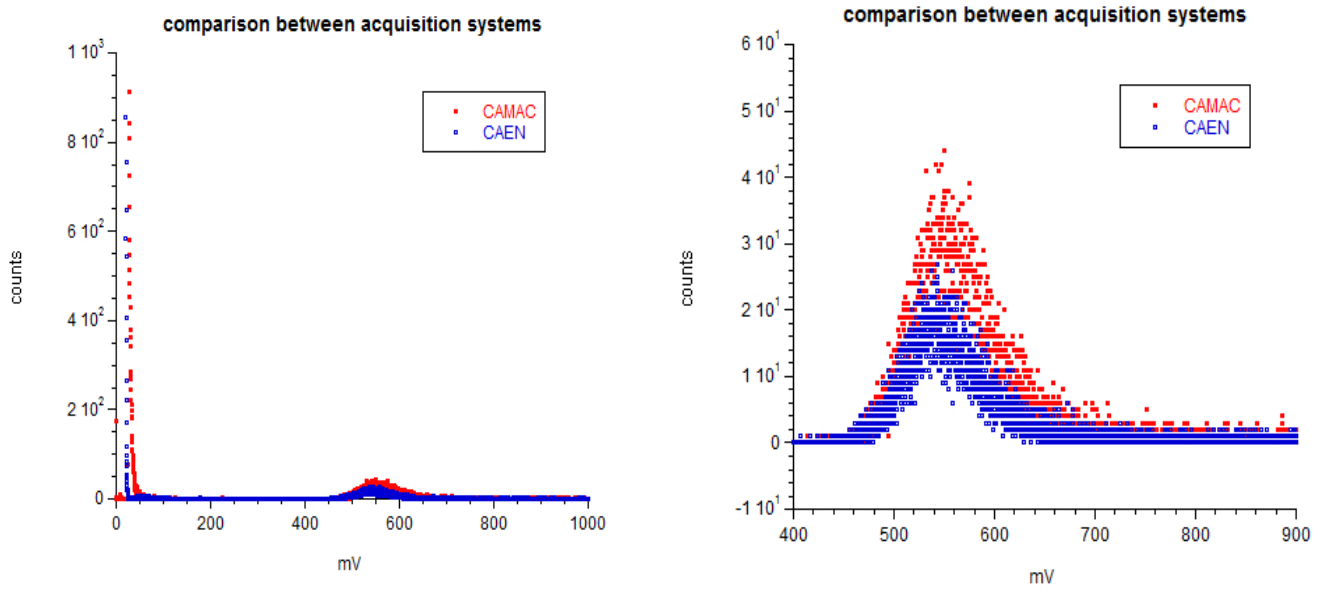
Pic. 6.5.13: *Contemporary acquisition of the alpha particle with two different acquisition systems.*

7. Effective gas gain measurements

7.1 Time stability measurements

We performed several measurements with a ^{244}Cm alpha source positioned inside the cathode (see par. **5.2**). The collimating hole, although necessary to perform measurements with good accuracy, shields a great part of the alpha particles emitted from the source. The counting rate is about 10 particles per minute, that requires at least several hours to obtain a spectrum with good statistics.

In picture **7.1.1** a photo of the detector can be seen: the plastic A-150 cathode (black square), with the ^{244}Cm source inserted, (it is located below the screw whose head is visible at the centre of cathode), and the tube for the gas flow. Under the cathode, the kapton foil of the GEM with the copper contacts connected to the power supply filters, and, on the opposite side, the PCB anode, with the connections for the collection of the signal from one pad only (single microdosimeter).
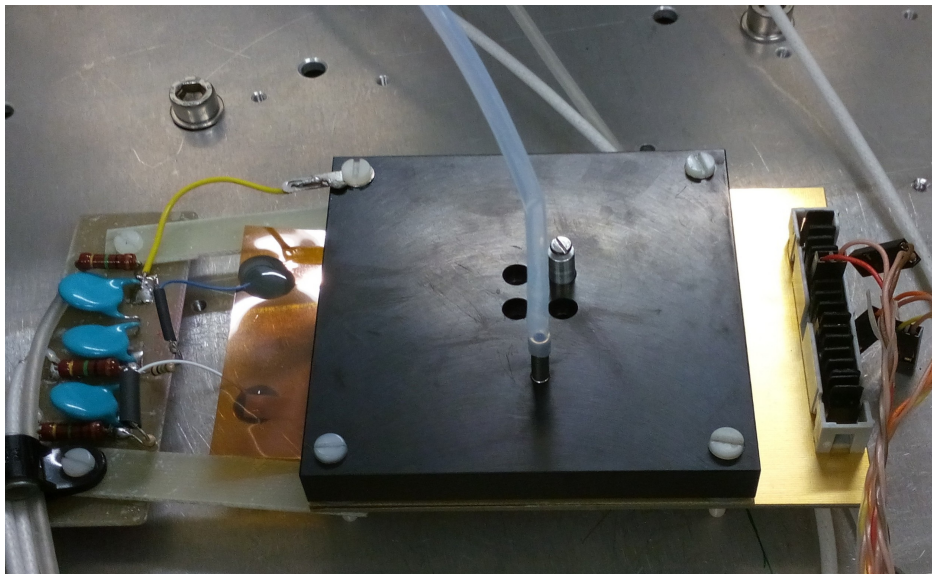
Pic. 7.1.1: *Photo of the detector.*

The independence of pads has been verified using the oscilloscope Tektronix: we connected up to four pad with different pre-amplifiers, and checked them in the 2 channels oscilloscope, using one signal as trigger of the other. We did not detect any signal in coincidence.

A typical pulse height spectrum collected with a voltage difference between the two sides of the GEM of 370 V is plotted in pic.**7.1.2**. Drift and induction fields were 600 V/cm and 4kV/cm, respectively. The peak in the pulse height spectrum was fitted by a Gaussian distribution to obtain the mean value and the FWHM of the peak. Despite the good value of the correlation coefficient of the fit, the peak show an evident tail at high energy values. To verify if this tail is due to a shift in the GEM gain, repeated measurements have been performed.
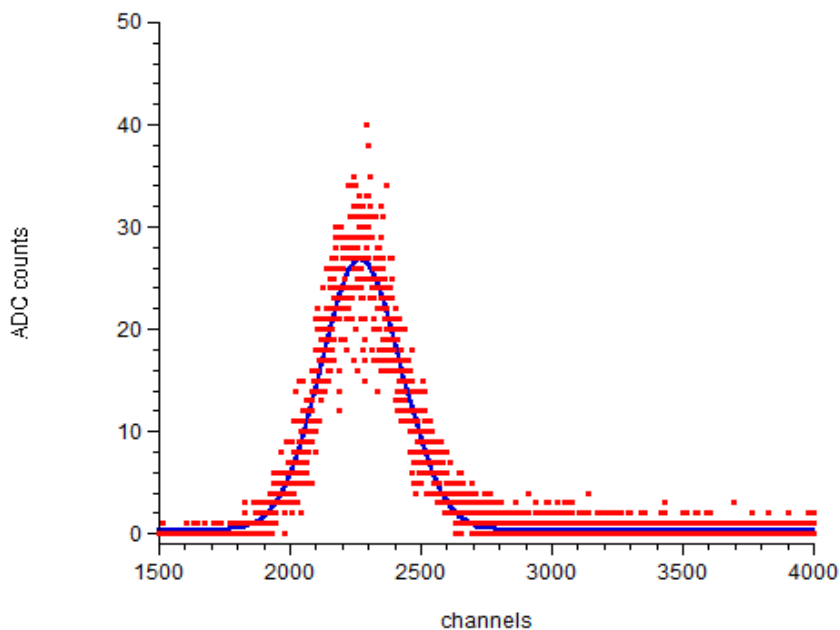
Pic. 7.1.2: *A typical spectrum obtained with the alpha source.*

In graph **7.1.3** two spectra are superimposed, taken with identical measurements conditions (600 V/cm as drift field, 4 kV/cm as induction field, and 400 V between the GEM electrodes) but at different times: the red one was acquired for t_1=381931,4 s and afterwards the blue one was acquired for t_2=223336,5 s and then normalized respect to time. The shape of the two spectra is identical, proving the signal stability over time.
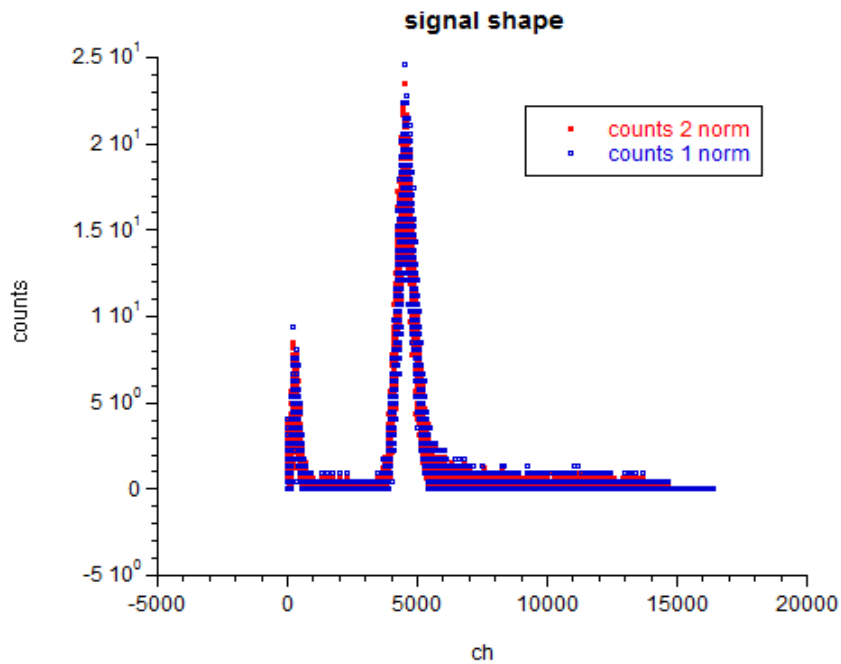
Pic. 7.1.3: *Shape of the spectrum obtained with the alpha particle, for two different acquisition time, normalized to 100000 s.*

The gain stability of the GEM is also reported in the literature [72, 77], even if it has also been reported that the GEM gain can shift as a function of illuminating time, due to the charging-up of the Kapton insulator surface inside the GEM holes [78]. The effect of gain shifting, however, is dependent from hours of functioning. Due to the low counting rate of our set-up, we performed acquisition holding the GEM in voltage for several days. The gain stability has been verified even after days, bringing the detector in the initial conditions after other measurements or even after opening the vacuum chamber.

The stability of the GEM gain is fundamental, since for our measurements long times are needed to achieve a good counting statistics.

The high energy tail visible in pic. **7.1.3** is therefore not due to a shift of the gain but it is correlated to the energy spectrum of the [244]Cm source. This spectrum, plotted in pic. **7.1.4**, has been measured in vacuum with a solid state detector and calibrated by using a 3 peak alpha source. The peak of the spectrum occur at energy 5.5 MeV. The tail at lower energy may cause the tail at high energy in the energy deposition spectrum measured with the GEM-TEPC and plotted in pic. **7.1.2**.

105
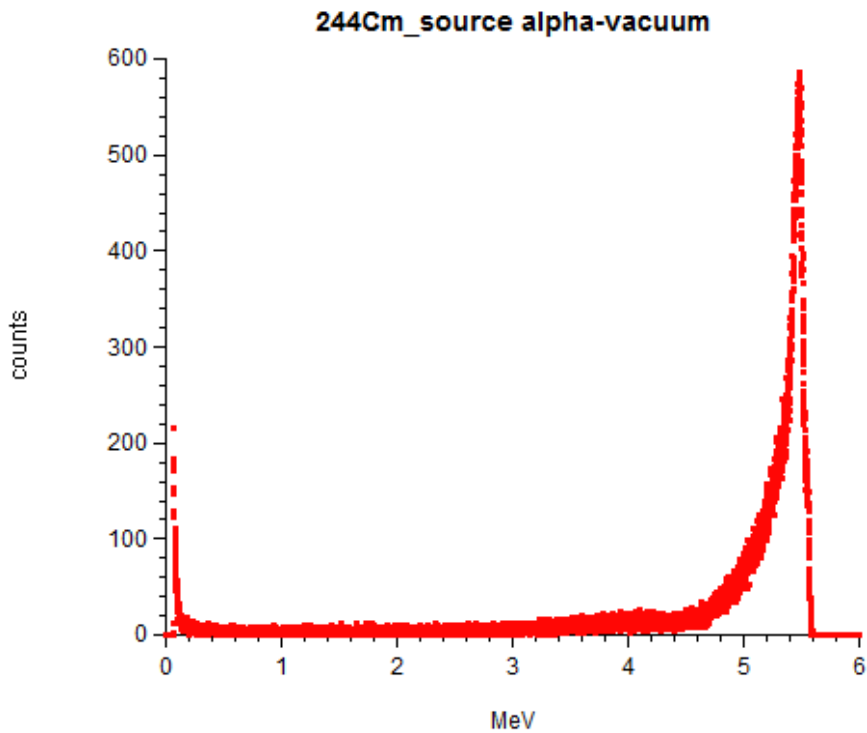
Pic. 7.1.4: Solid state spectrum of the ^{244}Cm alpha source.

7.2 Effective gas gain measurements

In order to evaluate the performance of GEM with propane gas, the effective gas gain, G_{eff}, was derived. The effective gas gain is defined by the following relation, which is the amount of charge collected on the readout pad divided by the primary charge: $G = \dfrac{N_f \cdot e}{N_i \cdot e} = \dfrac{Q_f}{Q_i}$

where N_f and N_i are numbers of electrons collected in the anode and released by the alpha particle

inside the collecting volume respectively, e is the electron charge and Q_f and Q_i are the charge collected at the anode and released in the collecting volume respectively.

G_{eff} was measured as a function of ΔV_{GEM}, E_D and E_i, where ΔV_{GEM} is the voltage difference across GEM and E_D and E_i are the drift and transfer field, respectively.

To find Q_f, we evaluate the position of the peak of the alpha particle spectrum V_{peak}, in mV and divide it for the gain factor of the pre-amplifiers (expressed in V/pC). Calculation of the pre-amplifier gain factor is presented in par. **6.4**.

To find Q_i we need to evaluate the energy released inside the sensitive volume. The alpha particle spectrum produced by the ^{244}Cm alpha source has been measured with a solid state spectrometer (see pic. **7.1.4**). The most probable alpha energy is 5.4MeV, whose range in pure propane gas is 0.0035 g/cm^3, which corresponds to a range of 35μm when scaled to a density of 1 g/cm^3. The most probable alpha energy deposited in the counter active volume has been calculated, disregarding the possibility of delta ray escape from the detector active volume (the maximum energy of delta rays is 2.7keV, whose range in C_3H_8 is about 20 μm/cm^2, which corresponds to a range of 200 nm when scaled to a density of 1 g/cm^3), by using the ICRU 49 data tables [92] to be (107 ± 4) keV.

By dividing the mean alpha energy released in the counter by the W-value of 28±0.5 eV [93] we have estimated the number of ionizations produced by alpha particle in the detector active volume. We found that one alpha particle inside our sensitive volume creates 3821 ± 221 ionisations, that correspond to $Q_i = (3821 \pm 221)e = (-6.1 \pm 0.3)\ 10^{-4}$ pC.

7.2.1 Drift field influence

The dependence of the effective gain on the drift field strength, E_D, has been measured. It is known that the electric field in the drift region should be strong enough to limit recombination between ions and electrons. On the other side, the drift field should not be too strong because this causes some field lines to terminate on the upper electrode of the GEM, reducing the fraction of the drifting electrons collected in the holes (electric transparency) [74, 75]. it has been reported that in many cases the two effects, recombination and transparency, causes an optimum gain to be attain between two values of E_D, a plateau. The dependence of G_{eff} on the drift field strength, E_D, was measured for fixed value of ΔV_{GEM} and E_i. Pic. **7.2.1** shows the results obtained with $\Delta V_{GEM}=430V$

and E_i=4 kV/cm, normalized to the effective gain measured with E_D=600 V/cm, where G_{eff}~3000. The relative effective gain increases with E_D until about 600 V/cm, then reach a plateau up to 800 V/cm and then start to increase again.
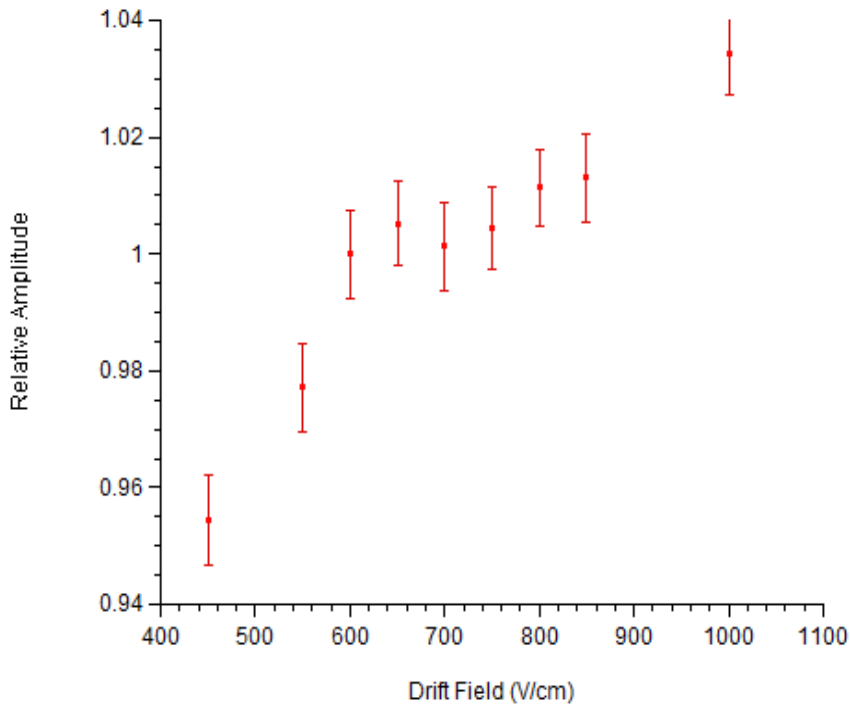
Pic. 7.2.1: Relative amplitude as a function of the drift field. Plateau is recognizable between E_D values of 600-800 V/cm.

The discordance of our measurements with the trend expected in literature (see sec. **4.4**) can be related to the difference in measurements conditions: data collected in literature are taken with 1 atm of pressure, while we work at 280 mbar. Probably in our conditions, different physical phenomena happens that causes an increased signal at high drift field. We made a simulation with the FlexPDE software of what happen to the electric field of the detector when the drift field increases. The trend is shown in pic. **7.2.2**, it can be seen that the multiplication region slightly enlarge, and this effect could be the cause for the signal increased amplitude after the plateau.
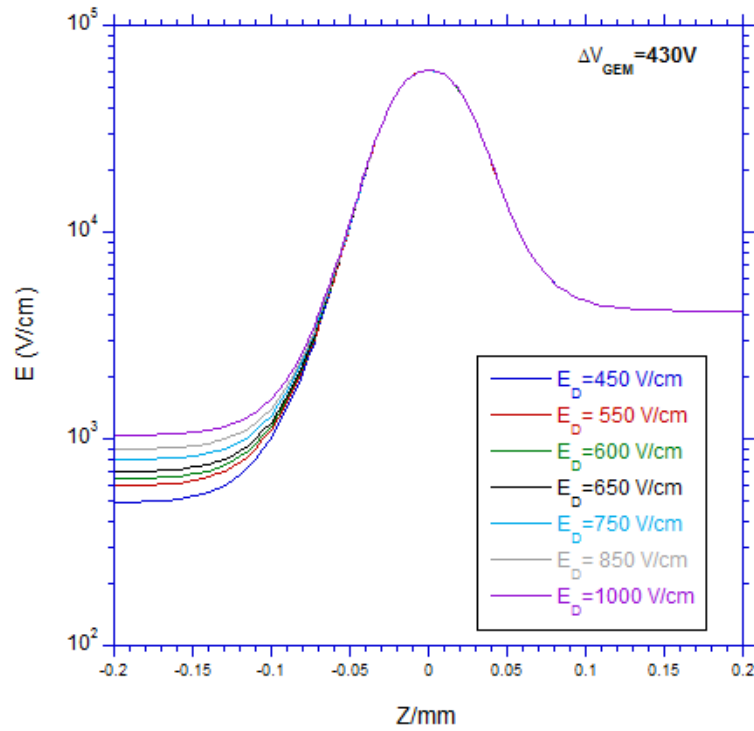
Pic. 7.2.2: Simulation of the electric field along the GEM hole channel as a function of the distance from the center of the GEM, for different values of drift field.

7.2.2 Induction field influence

The dependence on the effective gain on the induction field strength, E_i, has been measured. It is known that the electron collection efficiency increases in a nearly linear fashion with the induction field. The induction field, however, cannot be too high, because the full discharge propagation has a non-zero probability at high values of induction field [79].

The effect of the induction field E_i on G_{eff} was measured for fixed value of ΔV_{GEM} and E_D. Pic. **7.2.3** shows the results obtained with ΔV_{GEM}=430V and E_D=600V/cm, normalized to the effective gain measured with E_I= 4 kV/cm, where G_{eff}~3000.

The relative effective gain increases with E_i in a almost linear way. This results do not surprise, since we know from literature (see par. **4.5**) that the charge collected on the anode increase with the induction field.
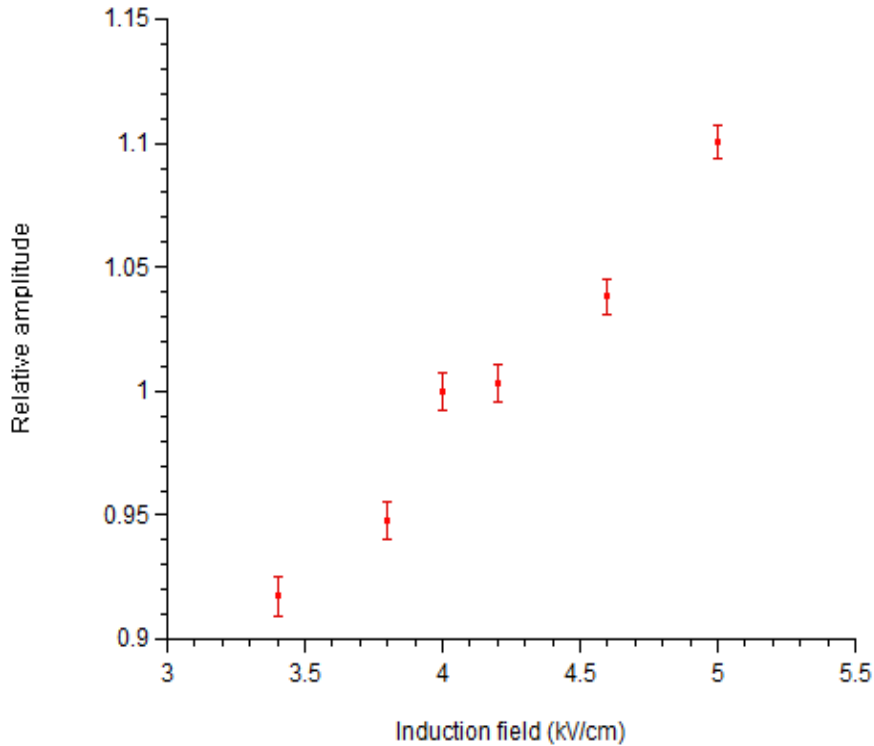
Pic. 7.2.3: *Relative amplitude as a function of the induction field. Plateau is recognizable between E_i values of 4-4.5 kV/cm.*

7.2.3 Multiplying field influence

We performed several acquisitions using the ^{244}Cm alpha source investigating the increment of the signal height with the potential difference applied to the GEM foil.

As the potential difference applied to the GEM foil increases, the electric field inside GEM's holes become greater, and so does the electron avalanche and the charge collected in the pad.

Effective gas gain measurements have been performed as a function of voltage difference across the GEM, ΔV_{GEM}, for fixed value of the drift and induction field, at 600 V/cm and 4 kV/cm respectively. To obtain the chosen fields, V_{drift} was kept at 120V higher of the voltage applied on the top of the GEM, and the voltage applied to the bottom of the GEM was kept at 200 V for all the

measurements. Results are plotted in pic. **7.2.4**. The maximum value of $G_{eff} \sim 6500$ does not correspond to the maximum safe gain because measurements were stopped before observing any discharge, to prevent damage to the GEM. In these conditions, we could reach even higher gain.

The fitting lines point out the exponential rise of the gain with increasing voltage.
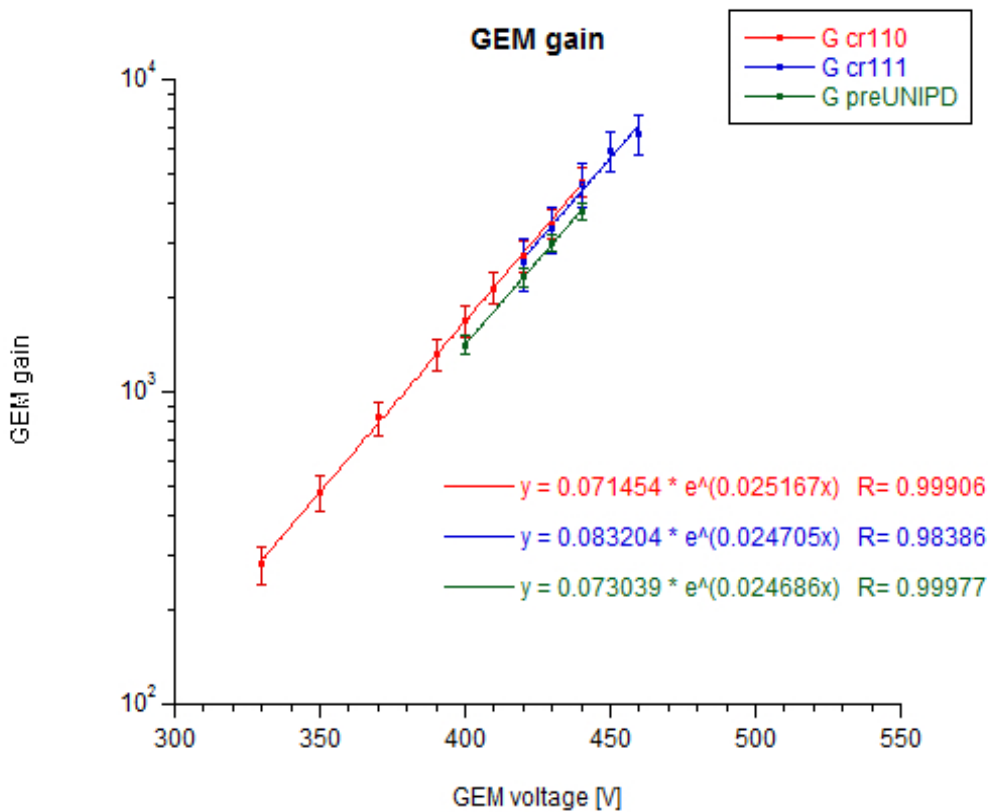
Pic. 7.2.4: GEM Gain changing the potential difference across the GEM. All measurements are collected with a pressure of 280 mbar, to simulate 1µm site.

Measurements has been taken with the three different pre-amplifiers described in par. **6.4**, obtaining comparable results: small differences are probably due to the fact that calculation of the gain factor is made with the nominal feedback capacity, and differences can be referred to the parasitic capacitance.

In pic. **7.2.5**, the trend of the Full Width Half Maximum (FWHM) of the alpha peaks is shown as a function of the voltage applied on GEM electrodes. It shows a exponential dependence with the applied voltage. In the same graph is represented also the resolution of the alpha peaks, that shows

a constant value around 20% for CR110 and preUNIPD. For CR111 the resolution is also around 20% until ΔV_{GEM}=440 V that correspond to a GEM gain of ~5000, then increases. Further studies are required to explain the behaviour of the CR111 pre-amplifier, since other pre-amplifiers do not show the resolution increment.
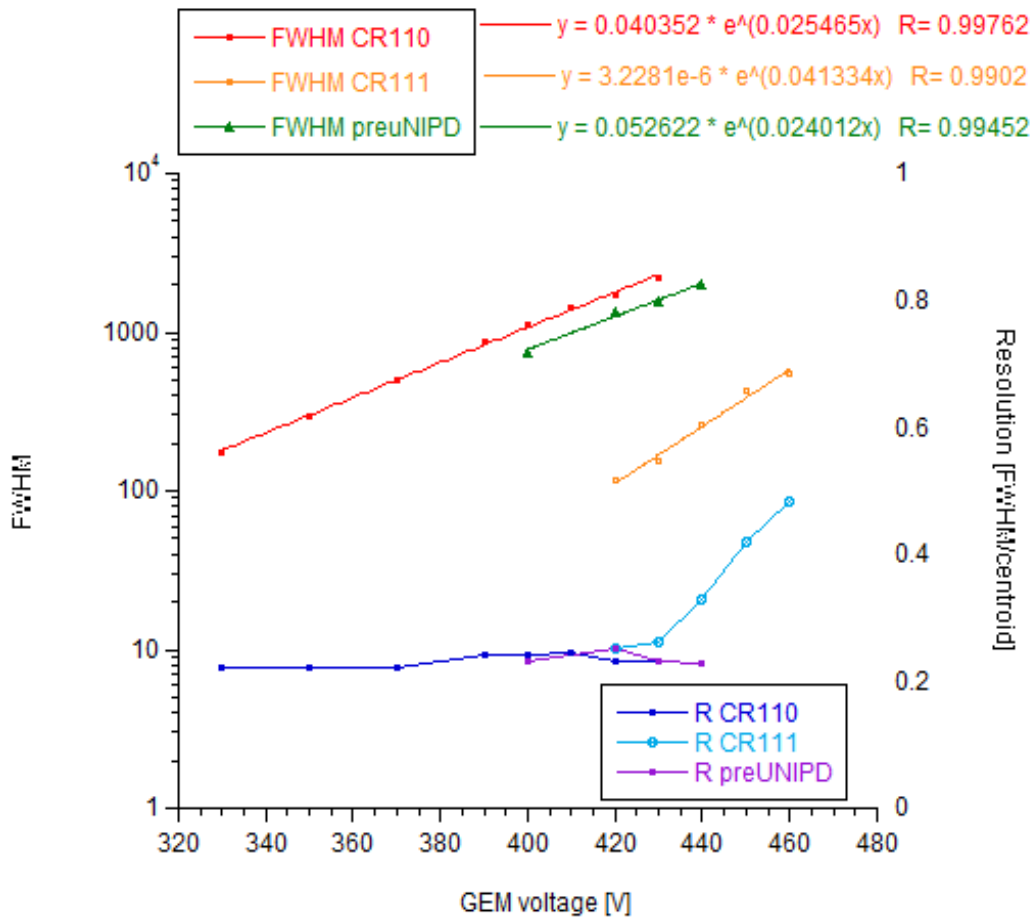
Pic. 7.2.5: Full Width Half Maximum and resolution as a function of GEM voltage, for the pre-amplifiers used.

As the properties of GEM gain in low pressure propane are, at our knowledge, currently undocumented, we don't have literature results to compare with. It is expected that the gas gain in pure propane should not be very different than that in propane-TE [46, 82]. A comparison can therefore be made with data collected by M. Farahmand (pic. **7.2.6**), with slight different GEMs (he made measurements with GEM which holes are 80μm or 60μm large, while in the GEM we used, they are 70μm large), but with propane-based TE gas instead of pure propane at a pressure of 300

mbar.

The increase of the gain with V_{GEM} show a similar dependence but for the same V_{GEM} gain are higher in pure propane than in TE propane-based gas. This can be related to the different gain characteristics of the two gases. Besides for the same applied voltage, and equal gas, the electric field along the hole channel is stronger with decreasing hole diameter.
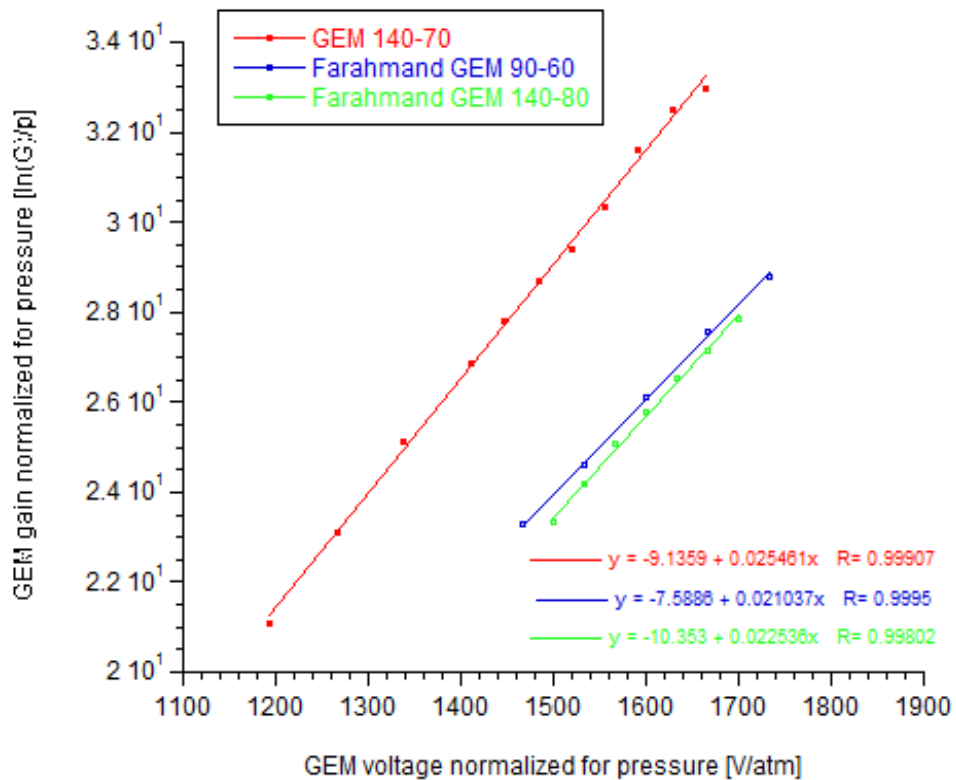
Pic. 7.2.6: *Comparison with values of gain obtained by M. Farahmand [55].*

In pic..**7.2.7** we represented the maximum value of the electric field along the hole channel calculated with the software FlexPDE for three different geometries of the GEM.
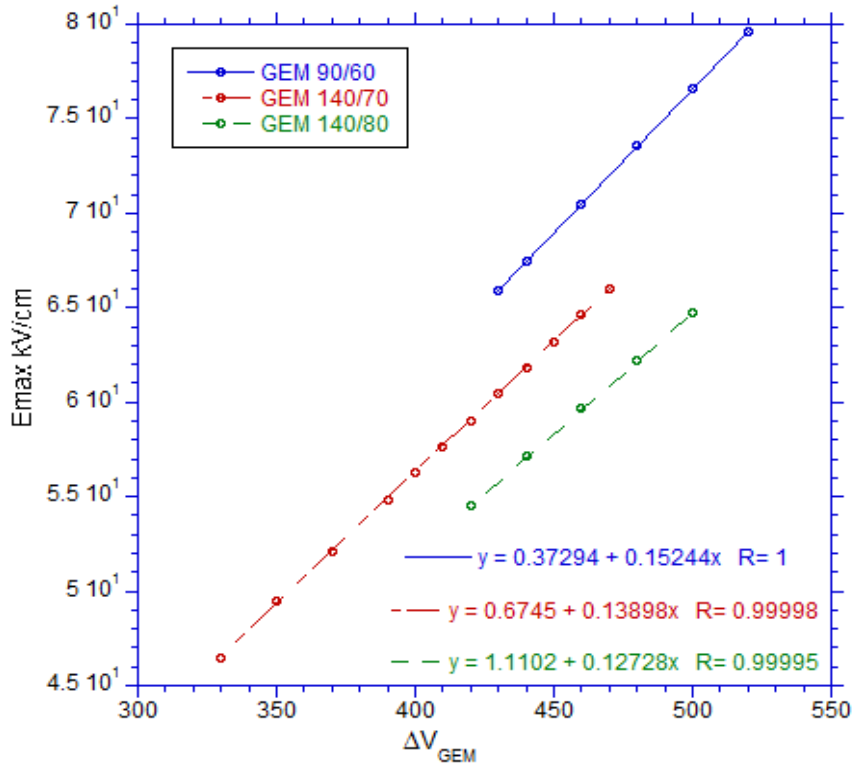
Pic. 7.2.7:*Maximum value of the electric field along the hole channel for different GEM geometries.*

7.3 Microdosimetric measurements with gamma source

We take a gamma spectrum with a ^{137}Cs with (411±12) kBq source resting on the cathode-TE surface, as shown in pic. **7.3.1**, using the CAMAC acquiring system.

We preferred to use an analogical acquiring system to avoid the non-linear channels zone of the CAEN ADC, that can affect the gamma measurements since the energy-deposition is lower than

for alpha particles. Measurements have been performed at 1 μm simulated site size (with ΔV_{GEM}=430V, E_D=600 V/cm and E_I=4 kV/cm).
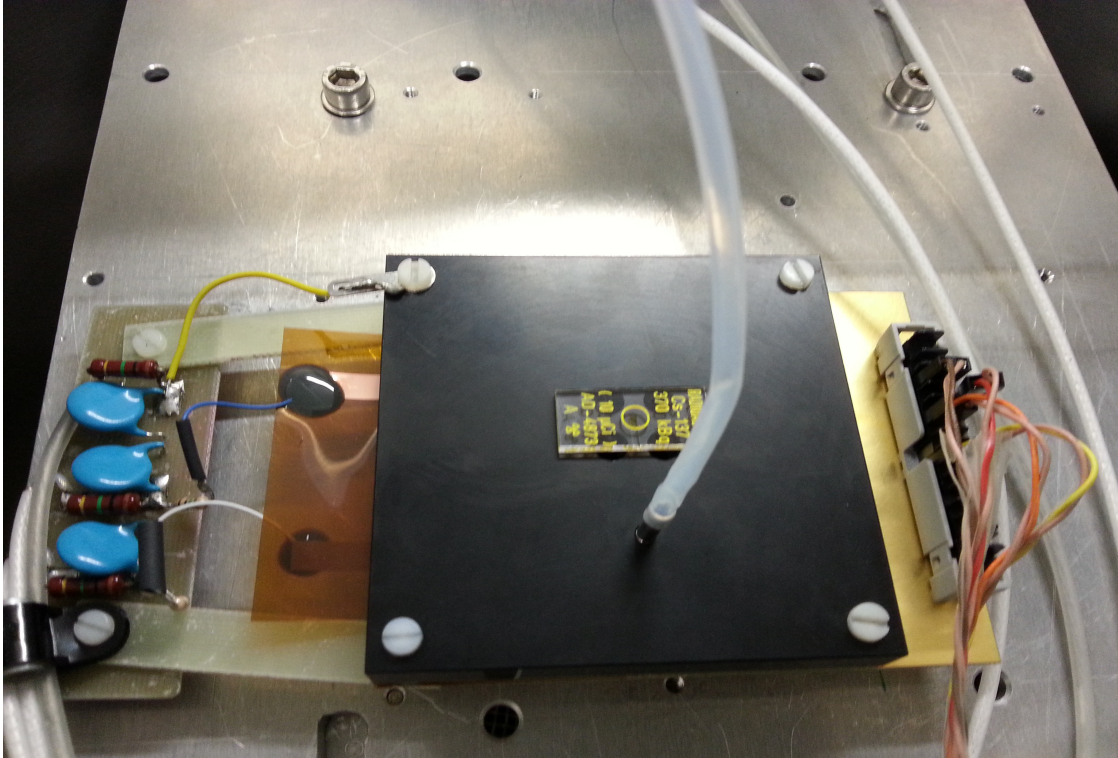
Pic. 7.3.1: *Set up for the acquisition of the gamma spectrum.*

In pic. **7.3.2** the spectrum measured with the GEM-TEPC is compared with a spectrum measured with a spherical TEPC, truncating the spectra at the same lower threshold of 0.18 keV/μm. The uphill and the downhill portion of the two spectra are super-imposable, while the central part is different between the two. These differences may be attributable to the different conditions of irradiation and the different distribution of mean chord length of the two detectors. Mean chord length in influenced by the radiator position: while in usual TEPC with central anode wire, the radiator is all around the sensitive volume, providing an isotropic radiation field, in the prototype developed, the radiator is the cathode in TE plastic, that is only in the upper layer of the sensitive volumes, so the radiation field won't be isotropic. Despite these differences, the agreement between the two spectra is quite satisfactory, as is proved by a comparison between the frequency mean lineal energy y_F, and the dose mean lineal energy y_D of the two spectra, considering a lower threshold of 0.18 keV/μm:

	EuTEPC	GEM-TEPC
y_D	2.69±0.13 keV/μm	2.92±0.15 keV/μm
y_F	0.80±0.08 keV/μm	0.85±0.09 keV/μm

Table 6: *Comparison of frequency mean lineal energy and dose mean lineal eneergy.*

The lower threshold might be diminished using an higher GEM gain, and optimizing the cables connections between detector and acquisition system.
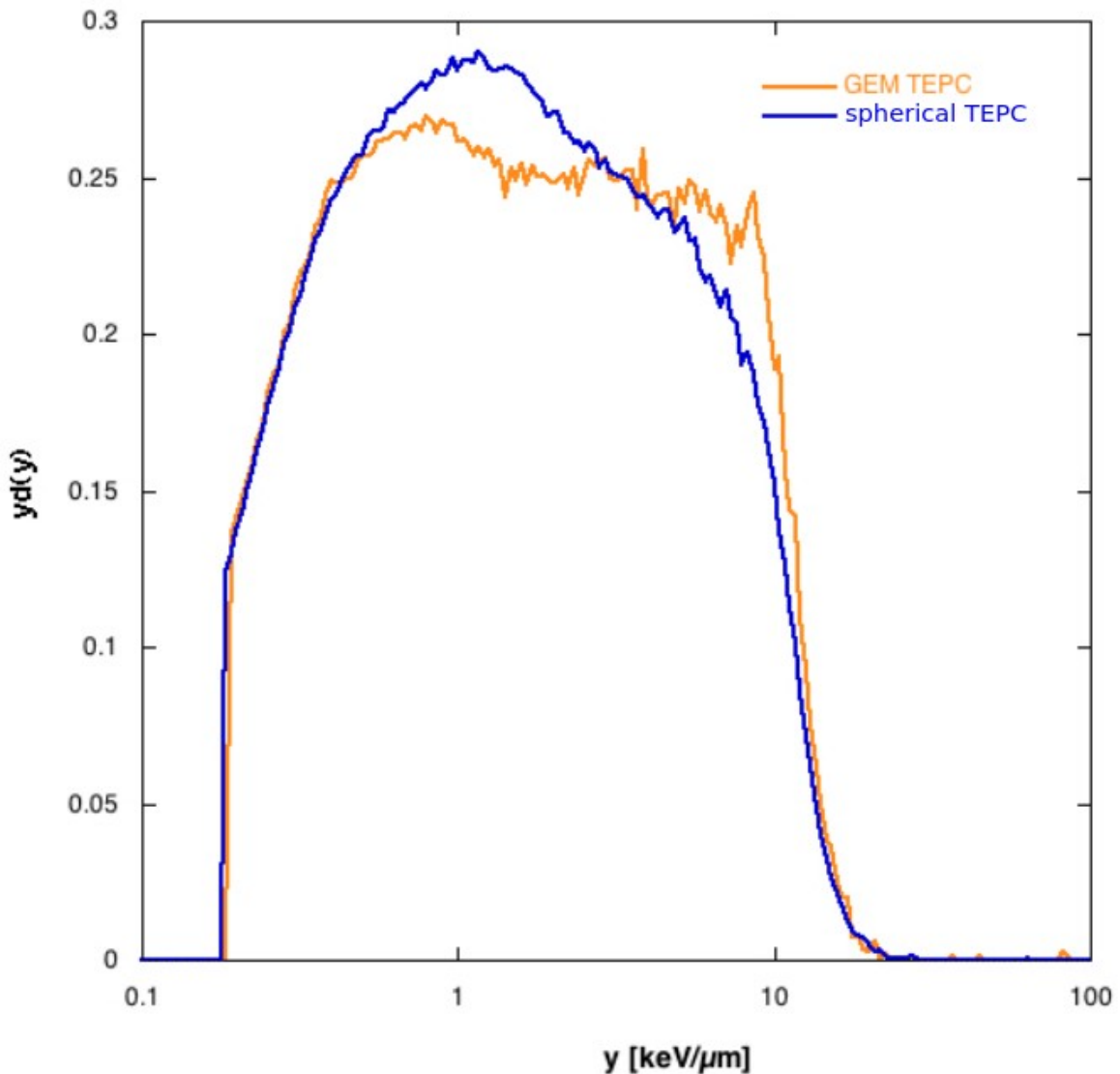
Pic. 7.3.2: *Comparison between microdosimetric spectra of gamma radiation taken with our GEM-based detector and a traditional spherical TEPC.*

8. Conclusion and further development

In this work we evaluated the performances of a multiple-TEPC detector based on a GEM. We studied the GEM gain for different potentials applied to the GEM electrodes, without reaching the discharge. This mean that the maximum GEM gain we obtained (~6500 with 460V between the GEM) is not the maximum safe gain. Further studies will be done to investigate the maximum safe gain of a GEM based TEPC in pure propane.

We tested the detector as a single miniTEPC, with a gamma source placed on the cathode-TE, and compared it with a spectrum obtained with a spherical TEPC with the same gamma source. The agreement between the two spectra was quite satisfactory, despite differences in the shape of the spectra that can be linked to the differences in the chord length distribution (spherical vs cylindrical geometry, see par. **2.2**). Further measurements will be performed with different radiation beams to fully understand the impact of our geometry on the microdosimetric spectra. Furthermore, we test the detector as a single miniTEPC, and verified that every pad does not communicate with the nearer, other studies will be made about its behaviour as a multiple-TEPC detector.

The energy range required for a microdosimetric spectrum is large (see par. **2.3**), from 0.1 to 1500 keV/μm. Usually microdosimetric measurements are performed with three different amplifier, with different amplification factor and three different ADC, to cover it. To have a compact and portable acquisition system, we propose to use only the desktop module ADC CAEN DT5724, with a range from 0 to 2.25 V and apply a different voltage between GEM electrodes and different pre-amplifiers to set a microdosimetric range appropriate for the measurements. Referring to the alpha peak position, we can relate ΔV_{GEM} with the microdosimetric range visible. For example, using the pre-amplifier developed by the university of Padova, considering the lowest detected signal around 5 mV, and with a ΔV_{GEM}=460V, the microdosimetric range visible is from 0.2 to 115 keV/μm, suitable for measurements with gamma rays (a range smaller is reachable optimizing the noise, for example diminishing the length of the cables that connect the detector to the pre-amplifier, and increasing the GEM gain till the maximum safe gain in pure propane). If, on the

other side, we need to measure in a heavy ions beam, we could use the CR111 pre-amplifier, considering the lowest detected signal around 10 mV, and with a ΔV_{GEM}=440V, the microdosimetric range visible is from 4 to 1956 keV/µm.

A particle crossing the detector will ionize both inside the Drift gap and induction gap. The thickness of the drift region is 2mm, the one of the induction region is 0.5 mm. Let us take into consideration the maximum ionizing particle to be detected. Supposing the same ionization linear density in the two region, a charge Q_{drift}=Q will be produced in the drift region, a charge Q_{ind}=Q/4 will be produced in the induction region. The charge Q_{drift} will be multiplied by the effective gain factor of the GEM, G_{GEM}, giving rise to the total collected charge $G_{GEM} \cdot Q_{drift}$, while the charge Q_{ind} will not be amplified. In order that Q_{ind} will not produce a detectable signal, $Q_{ind} \leq Q_{threshold}$. Therefore the dynamic range of the measurable signal will be at maximum (when $Q_{ind}=Q_{threshold}$) equal to $4G_{GEM}$.

To increase the dynamic range it should be necessary to increase the ratio Q_{drift}/Q_{ind} by increasing the drift region thickness compared to the induction thickness.
To induction gap cannot be reduced, since 0.5mm is the size of the insulating frame of the GEM foil. It is possible instead to increase the drift gap, but in order to simulate always a micrometer it will be necessary to decrease the pressure.
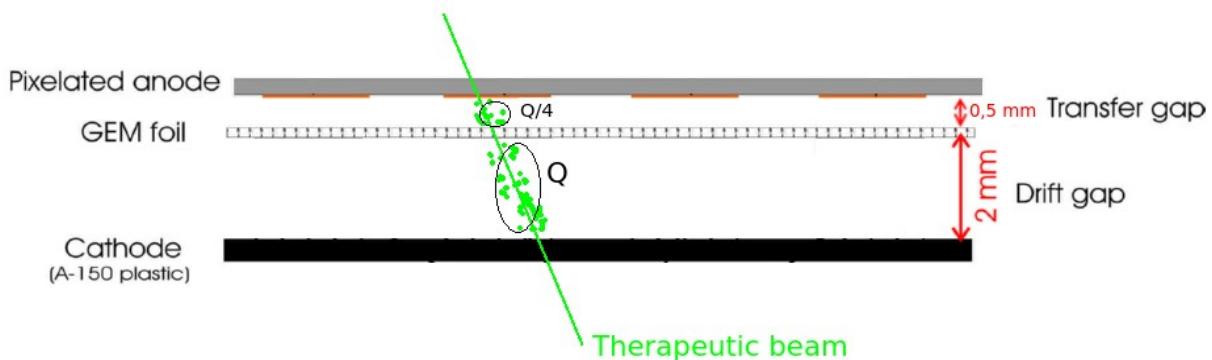

Pic. 8.1: *Effects of a charged particle crossing the detector.*

In case of energetic ion beams, as for a therapeutic carbon beam, the charge released in the induction region can be higher than the threshold used. To keep the dynamic range as large as possible, it will be necessary to take spectra both with drift field inverted and direct in order to

remove the signal released in the induction gap.

In our measurements conditions (lower threshold of 0.18 keV/μm) the minimum charge detected is of about ~6 electrons, and can be improved with shorter cables connections between the detector and pre-amplifiers, or increasing the GEM gain to detect even smaller signals.

A containment chamber for the detector has been designed and is being implemented in order to be able to measure at beams of LNS and CNAO. In pic. **8.3** is visible an overall view of the project of the chamber and the technical drawing. On left side wall of the parallelepiped container are connectors for SHV power supply of the GEM and the cathode, on the opposite side feedthroughs for signal connections from the pads, and on the front side fittings for pumping and gas flushing and the absolute pressure meter. On the lid of the container is visible a flange CF with central hole, closed by a sheet of Mylar, which will form the input channel of the accelerated beam, in correspondence of the sensitive volume of the detector.
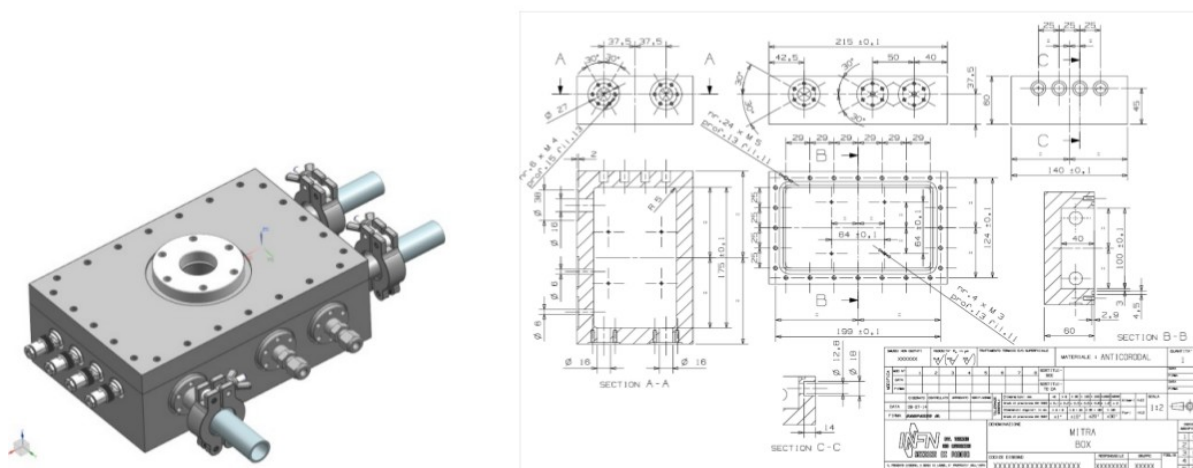
Pic. 8.3: Containment chamber of the detector for measurements on accelerated therapeutic beams.

The TEPC-GEM has potentially many advantages compared to the usual TEPCs such as, cheapness, simplicity in construction, robustness and stability in operation. Moreover, the components (sensitive volumes, GEM and wall material) are easy to modify. The TEPC-GEM we developed offers the possibility of a 2D scan of the therapeutic beam in a 4x4 matrix of sensitive volumes, each one acting like a single TEPC.

The advantages for a clinical usage are many: such as, easily to re-product in case of break-out,

easily changing acquiring condition, acting on the GEM gain; furthermore, changing the sensitive volume, and/or the gas type and pressure, it is possible to simulate sites with different size and compositions. It can be easily modified and optimized accordingly to the type of informations needed and to the radioactive beam used.

References

- [1] http://www.ptcog.ch PTCOG: Particle Therapy Co-Operative Group

- [2] Paganetti et al. *Relative biological effectiveness (RBE) values for proton beam therapy*, Int. J. Radiat. Oncol. Biol. Phys. 2002; 53, 407

- [3] P.Kliauga *Measurement of a single event energy deposition spectra at 5nm to 250nm simulated site size* Rad. Prot. Dos. Vol. 31 N° 1/4 pp. 119-123 (1990)

- [4] Wilson RR, *Radiological Use of Fast Protons* Radiology 47: 487-491, (1946).

- [5] O. Jäkel, *Radiotherapy With Protons And Ion Beams* International Scientific Meeting on Nuclear Physics, (2009).

- [6] ICRU report 16 (1970)

- [7] D. Schardt and T. Elsässer D. Schulz-Ertner, *Heavy-ion tumor therapy: Physical and radiobiological benefits* Rev. Of Mod. Phys, vol. 82, (2010).

- [8] Haettner E, Iwase H, Schardt D: *Experimental fragmentation studies with 12C therapy beams*, Radiat Prot Dosimetry. 122 (2006) 485-7.

- [9] K. Gunzert-Marx, H. Iwase, D. Schardt and R. S. Simon *Secondary beam fragments produced by 200MeV/u ^{12}C ions in water and their dose contributions in carbon ion radiotherapy*, New J. Phys. 10 **(**2008)

- [10] Serber *Nuclear reactions at high energies* Phys. Rev.**72**1114–5 (1947)

- [11] J. M. Brown, *Tumor hypoxia in cancer therapy*, Methods Enzymol.; 435:297-321, (2007).

- [12] Furusawa Y, Fukutsu K, Aoki M et al: *Inactivation of aerobic and hypoxic cells from three different cell lines by accelerated ^{3}He, ^{12}C and ^{20}Ne ion beams*. Radiat Res 154 (2000) 485–96.

- [13] J. D. Chapman et al. *Radiobiological characterization of the inactivating events produced in mammalian cells by helium and heavy ions,* Int. J. Radiat. Oncol. Biol. Phys. 3 (1977) 97

- [14] J. D. Chapman et al. *Radiation biophysical studies with mammalian cells and a modulated carbon ion beam* Radiat. Res. 74 (1978) 101

- [15] E. Blakely et al. *Physucal and cellular radiobiological properties of heavy ions in relation to cancer therapy applications,* report (1980)

- [16] J. T. Lyman et al. *Radiological physics of heavy charged-particle beams used for therapy,* report (1980)

- [17] T. Kanai et al. *Irradiation of mixed beam and design of spread-out Bragg peak for heavy ion radiotherapy,* Radiat. Res. 147 (1997); 78

- [18] K. Kagawa et al. *Preclinical biological assessment of proton and carbon ion beams at Hyogo Ion Beam Medical Center,* Int. J. Radiat. Oncol. Biol. Phys. 54 (2002) 928

- [19] M. Scholz, G. Kraft, *Calculation of heavy ion inactivation probability based on track structure, x-ray sensitivity and target size,* Radiat. Prot. Dosim. 52 (1994) 29

- [20] M. Scholz et al. *Computation of cell survival in heavy ion beams for therapy. The model and its approximation.* Radiat. Environ. Biophys. 36 (1997) 59

- [21] Scholz M. *Dose Response of Biological Systems to Low- and High-LET Radiation*. Amsterdam: Elsevier; 2006.

- [22] ICRU report 36, (1983)

- [23] H. H. Rossi, M. Zaider, *Microdosimetry and its applications,* (1996).

- [24] A. M. Kellerer *Considerations on the random traversal of convex bodies and solutions for general cylinders,* Radiat. Res. 47 (1971) 359

- [25] ICRU report 60 (1991)

- [26] T. Doke et al. *Comparison of LET distributions measured in low-earth orbit sting tissue-equivalent*

proportional counters and the position sensitive silicon-detector telescope (RRMD-III), Radiat. Res. 156 (2001) 310

- [27] J. Taddei et al. *The response of a spherical tissue-equivalent proportional counter to different heavy ions having similar velocities* Radiation Measurements 41 (2006) 1227 – 1234

- [28] Borak et al. *Comparisons of LET distributions for protons with energies between 50 and 200 MeV using a spherical tissue equivalent proportional counter (TEPC) and a position sensitive Si-spectrometer (RRMD-III).* Radiat. Res. 162, 687–692. 2004

- [29] ICRU report 40 (1986)

- [30] A. M. Kellerer *Revision of the quality factor,* Radiat. Res. 114 (1988) 480.

- [31] Tilikidis A. et al. *An estimation of relative biological effectiveness of 50 MV bremsstrahlung beams by microdosimetric techniques.* Phys. Med Biol 41, 55-69, (1996).

- [32] Loncol, T., Cosgrove, V., et al., *Radiobiological effectiveness of radiation beams with broad spectra: microdosimetric analysis using biological weighting functions.* Radiat. Prot. Dosim. 52, 347–352, (1994).

- [33] Pihet, P., Menzel, H.G., et al., *Biological weighting function for RBE specification of neutron therapy beams.* Radiat. Prot. Dosim. 31, 431–442, (1990).

- [34] L. de Nardo et al. *Microdosimetric assessment of Nice therapeutic proton beam biological quality* Phys. Medica XX (2004)

- [35] G. Coutrakon, *Microdosimetry spectra of the Loma Linda proton beam and relative biological effectiveness comparisons,* Med. Phys. 24 (9), September 1997

- [36] Gerlach, Roost, Kellerer, *Heavy ion RBE and microdosimetric spectra*, Radiat. Prot. Dosim. Vol. 99, 413-418 (2002)

- [37] R. B. Hawkins, *A Statistical Theory of Cell Killing by Radiation of Varying Linear Energy Transfer*; Radiat. Res. 1994; 140, 366-374.

- [38] A. M. Kellerer and H. H. Rossi, *The theory of dual radiation action,* Radiat. Res. 8 (1972) 85.

- [39] T. Sato et al. *Biological dose estimation for charged-particle therapy unsing an improved PHITS code*

coupled with microdosimetric kinetic model, Radiat. Res. 171 (2009) 107.

- [42] T. Inaniwa et al. *Treatment planning for a scanned carbon beam with a modified microdosimetric kinetic model,* Phys. Med. Biol. 55 (2010)

- [41] Y. Kase et al. *Microdosimetric measurements and estimation of human cell survival for heavy-ion beams.* Radiat. Res. 166, 629– 638 (2006).

- [42] Y. Kase et al. *Biophysical calculation of cell survival probabilities using amorphous track structure models for heavy-ion irradiation.* Phys. Med. Biol. 53, 37–59 (2008).

- [43] Albrecht M. Kellerer, *Fundamentals of Microdosimetry* (1985)

- [44] J. S. Lilley, *Nuclear Physics: principles and applications* (2001)

- [45] A. J. Waker, *Principles of experimental microdosimetry,* Rad. Prot. Dos. Vol. 61, 297-308 (1995)

- [46] I. K. Bronic and B. Grosswendt, *Ionization coefficient in propane, propane-based tissue equivalent and dimethyl-ether in strong non-uniform electric fields,* J. Phys D, Appl. Phys 32 (1999) 3179

- [47] P. Segur et al. *Numerical modelling of tissue-equivalent proportional counters,*Radiat. Prot. Dosim. 61 (1995) 323.

- [48] T. E. Burlin, *A general theory of cavity ionisation,* Brit. J. Radiol. 39, 727. (1966).

- [49] *Relative Biological Effectiveness in Ion Beam Therapy ,* IAEA Technical Reports Series No. 461 (2008)

- [50] Health, SI broader scope and new tecgnologies, *biologically weighted quantities in radiotherapy.* EMRP Call (2011)

- [51] D. Moro, L. De Nardo, P. Colautti, V. Conte, T. Berger, K. Marsalek, P. Beck, S. Rollet, M. Latocha, et al. *EuTEPC - (European Tissue Equivalent Proportional Counter): a Microdosimeter for the Assessment of the Radiation Quality at the International Space Station* 2011, LNL-INFN Report

- [52] S. Tsuda at al., *Measurement of microdosimetric spectra with a wall-less tissue-equivalent proportional counter for a 290 MeV/u ^{12}C beam* Phys. Med. Biol. 55 5089, (2010)

- [53] S.E. Rademacher et al. *Wall effects observed in tissue-equivalent proportional counters from 1.05*

GeV/nucleon iron-56 particles. Radiat. Res. 1998; 149(4): 387-95.

- [54] D. Moro, *Determinazione del fattore di qualità mediante TEPC miniaturizzati nella radioterapia adronica,* Thesis (2005)

- [55] M. Farahmand, *A novel Tissue-Equivalent Proportional Counter Based on a Gas Electron Multiplier.* PHD thesis (2004)

- [56] G. M. Orchard et al. *Development of a thick gas electron multiplier for microdosimetry* Nuclear Instr and Meth in Phys Res A 638 (2011) 122–126

- [57] L. Periale, et al. *Detection of the primary scintillation light from dense Ar, Kr and Xe with novel photosensitive gaseous detectors,* Nucl. Instr. and Meth. A 478 (2002) 377.

- [58] J. Dubeau, A. J. Waker *Neutron microdosimetric response of a Gas Electron Multiplier,* Radiat. Prot. Dosim. , Vol. 128, 413–420 (2008)

- [59] A. Fazzi, S. Agosteo et al. *Test of the ΔE/E Silicon Microdosimeter at the CATANA Facility* 2009 IEEE Nuclear Science Symposium Conference Record

- [60] S. Agosteo et al. *Feasibility study of radiation quality assessment with a monolithic silicon telescope: Irradiations with 62 MeV carbon ions at LNS-INFN* Radiation Measurements 46 (2011) 1534-1538

- [61] S. Agosteo et al. *Study of a silicon telescope for solid state microdosimetry: Preliminary measurements at the therapeutic proton beam line of CATANA Radiation Measurements,* 45 (2010) 1284-1289

- [62] N. Tartone, M. Angeloni et al. *X-Ray Detection by Using CVD Single Crystal Diamond Detector* IEEE Transaction on Nuclear Science, vol. 56, No. 3, (2009)

- [63] M. Angelone et al. *Simulation and Test of a New Microdosimeter Based upon Single Crystal Diamond* (2011)

- [64] D. Moro *Development of tissue-equivalent proportional counter for BNCT microdosimetry*, PHD thesis (2006)

- [65] P. Pihet *Etude microdosimetrique de faisceaux de neutronsde haute energie. Apllication dosimetrique et radiobiologiques*, Thesis (1989)

- [66] A. J. Waker et al. *Experimental uncertainties in microdosimetric measurements*, Nucl. Instr. And Meth. A234 (1985) 354.

- [67] V. Conte et al. *Lineal energy calibration of mini tissue-equivalent gas-proportional counters (TEPC)*, Ion Beam (2012)

- [68] F. Sauli, *GEM: A new concept for electron amplification in gas detectors*, Nucl.Instr. and Meth. in Phys. Res. A 386 (1997) 53 l-534

- [69] T. Geralis *The continuing rise of micropattern detectors*, CERN courier (2009).

- [70] M. Wakabayashi et al. *Development of a Diehard GEM using PTFE insulator substrate* JINST (2014)

- [71] H.S. Cho et al. *GEM: Performance and aging tests.* IEEE Trans. Nucl. Science 46 (1999) 306

- [72] J. Benlloch et al. *Further developments and beam tests of the gas electron multiplier (GEM)* Nuclear Instruments and Methods in Physics Research A 419 (1998) 410-417

- [73] S. Bachmann et al. *Discharge studies and prevention in the gas electron multiplier*, Nuclear Instruments and Methods in Physics Research A 479 (2002) 294–308

- [74] S. Bachmann et al., *Charge amplification and transfer processes in the gas electron multiplier* Nucl. Instr. and Meth. A 438 (1999) 376

- [75] T. L. Van Vuure et al. *Properties of the GEM, double GEM and GEM + MGC combination.* Nucl. Instr. And Meth. A443 (2000) 375

- [76] M. Alfonsi *Studio e sviluppo di un rivelatore a GEM per la zona centrale delle camere per muoni di LHCb*, (2003)

- [77] C. Richter et al. *Absolute electron transfer efficiency of GEM*,Nucl. Instr. and Meth. A 461 (2001) 38–41

126

- [78] C. S. Lee et al. *Properties of thick GEM in low-pressure deuterium,* 3rd interational conference od micro-pattern gaseous detectors (2013)

- [79] S. Han, H. Kang, *Charge-Sharing and Electron-Transfer Characteristics of a Gas Electron Multiplier (GEM),* Journal of the Korean Physical Society, 2002, pp. 820∼825

- [80] S. Ramo, *Currents Induced by Electron Motion,* Proc. IRE 27, 584 (1939)

- [81] A. Mitaroff et al. *The CERN-EU High-energy Reference Field (CERF) Facility for Dosimetry at Commercial Flight Altitudes and in Space,* Radiat. Protect. Dosim. 102 (2002) 7-22.

- [82] S. Chiriotti, D. Moro, V. Conte, P. Colautti, B. Grosswendt, *Equivalence of Pure Propane and Propane-TE Gases for Microdosimetric Measurements,* MICROS 2013, (2013)

- [83] A. M. Kellerer, *An Assessment of Wall Effects in Microdosimetric Measurements* Radiat. Res 47, (1971)

- [84] B. Azmoun, G. Karagiorgi, C. Woody, *A Comparative Study of GEM Foils from Different Manufacturers* (2004)

- [85] V. Radeka, *Optimum Signal Processing for Pulse Amplitude Spectrometry in the Presence of High-Rate Effects and Noise* IEEE Trans. Nucl. Sci. NS-15 (1968) 455

- [86] Kellerer, A.M. *Criteria for the equivalence of spherical and cylindrical proportional counters in microdosimetry.* Radiat. Res. 86 (1981) 277.

- [87] Kliauga, P., Waker, A. J. and Barthe, J. *Design of Tissue-Equivalent Proportional Counters.* Radiat. Prot. Dosim. 6 (1995) 309.

- [88] V. Aulchenko, A. Bondar, A. Buzulutskov, L. Shekhtman, R. Snopkov, Yu. Tikhonov, *Further studies of GEM performance in dense noble gases,* To be published in Nucl. Instr. and Meth. A

- [89] Cremat *CR-110 charge sensitive preamplifier: application guide* Rev. 2 (May. 2014)

- [90] Cremat *CR-111 charge sensitive preamplifier: application guide* Rev. 2 (May. 2014)

- [91] ORTEC *A study of the decay scheme of ^{244}Cm by an alpha x-ray coincidence experiment experiment 20*

- [92] ICRU Report 49, *Stopping power and ranges for protons and alpha particles* (1993)

- [93] Bronic I.K., *W Values in Propane-Based Tissue-Equivalent Gas* Radiat. Prot. Dosim. 70 (1997) 33

Acknowledgements

Voglio prima di tutti ringraziare la mia relatrice, Laura de Nardo, per i preziosi consigli e per la pazienza che ha avuto, e insieme a lei, tutti quelli del laboratorio a Legnaro, sempre disponibili e pronti ad aiutare, Davide, Sabina, Paolo e Valeria.

Credo poi di dover spiegare la mia dedica, *"alla mia bicicletta rosa"* ovvero all'evento che mi ha portato a fare fisica (se non capite il riferimento, dovete guardare la serie tv *Stacked*).

La *bicicletta rosa* è quell'evento che mi ha segnata, e portata a fare fisica, per dimostrare a tutti che si può fare, che io lo posso fare. Se non avessi perso l'occasione di giocare con i delfini a Gardaland quand'ero piccola, magari avrei scelto un'università diversa, non mi sarei appassionata al capire come funziona il mondo, non avrei giocato in laboratorio, ma soprattutto non avrei conosciuto Mauro.

Non c'è modo di ringraziare in una frase colui che è stato la mia forza nei momenti di sconforto, la mia lucidità nei momenti di panico, la mia serenità quotidiana, avrò tutta la vita per farlo.

Un ringraziamento va a tutta la mia famiglia: alla mamma e al papà, sempre al mio fianco, anche quando voglio fare tutto da me, alla mia sorellona (che è sempre più ina) che nonostante il tanto, troppo lavoro, mi è sempre stata vicina, alle zie, cosa dire delle mie zie? Siete meravigliose!!, alla mia cuginetta (sempre più etta) che è anche la mia allieva preferita, alle mie super nonne, e a tutti quanti!

Avete reso tutto questo possibile, aiutandomi quando ne avevo bisogno, costringendomi a prendermi delle pause anche se non volevo. So che spesso sono scontrosa (per usare un eufemismo), ma non dubitate mai di quanto vi ami.

A special thank to Ember, that was so kind to read my loooong thesis, from Canada, giving me good advices. My home will be always open for you.

Un ringraziamento va a tutti i compagni e gli amici di questi anni, compagni di una grande avventura a cui chiedere aiuto e da aiutare.

In bocca al lupo a tutti.